2010

LOCALIZED MECHANICAL DEFORMATION AND DISSOLUTION OF 45S5 BIOGLASS

Ding Li
University of Kentucky, liding@engr.uky.edu

ABSTRACT OF DISSERTATION

Ding Li

The Graduate School
University of Kentucky
2010

LOCALIZED MECHANICAL DEFORMATION AND DISSOLUTION OF 45S5 BIOGLASS

ABSTRACT OF DISSERTATION

A dissertation submitted in partial fulfillment of the
requirements for the degree of Doctor of Philosophy in the
College of Engineering
at the University of Kentucky

By

Ding Li

Lexington, Kentucky

Director: Dr. Fuqian Yang, Professor of Materials Engineering

Lexington, Kentucky

2010

ABSTRACT OF DISSERTATION

LOCALIZED MECHANICAL DEFORMATION AND DISSOLUTION OF 45S5 BIOGLASS

Bioactive glasses react with the human physiological solution in control of their biofunctionality. The stress state in bioactive glasses determines the chemomechanical reaction and their biofunctionality. Using the microindentation technique, the effect of the indentation deformation on the surface damage and material dissolution of 45S5 bioglass was investigated.

The indentation-induced residual stresses were calculated. Complete anelastic recoveries of the indentation depths and the impression marks were observed for the first time, which was likely driven by the stored strain energy over the anelastic deformation zone. The indentation-induced local surface damages were revealed before and after the immersion tests in phosphate buffer solution (PBS). The growth of the cracks in the PBS solution displayed the stress-corrosion behavior with the crack-growth speed being a linear function of the indentation load.

45S5-bioglass was crystallized at temperature of 650 ºC. Microindentation technique also was used to study the localized mechanical behavior of the crystallized 45S5-bioglass. The crystallization had little effect on the indentation hardness, and the indentation hardness of the crystallized 45S5-bioglass is the same as that of the corresponding material in vitreous state. The fracture toughness is about 3 times less than that of annealed 45S5-bioglass in vitreous state, suggesting the preference of using bioactive glasses of vitreous state in the implant applications. Also, the effect of crystallization on the material dissolution was examined in phosphate buffer solution.

We also studied the growth and mechanical behaviors of the Ca-P precipitate layers formed on 45S5 bioglass in simulated body fluid. The thickness of the Ca-P precipitate layers was proportional to the square root of the immersion time, and the ratio of Ca/P in the Ca-P precipitate layers increased with the immersion time and approached 1.67, corresponding to the stoichiometric hydroxyapaptite (HA).Using the indentation technique, the indentation behavior of the Ca-P precipitate layers was

investigated. The indentation hardness of the HA layers formed in SBF was found to be 0.40 GPa, and the contact modulus was 12.0 GPa. The contact modulus of 12.0 GPa is close to that of cortical bone. In this thesis, the primary mechanical properties of the non-crystalline and crystalline bioglass 45S5 were revealed. The relationship between the dissolution rate and localized residual stresses are discussed. With such knowledge, the evaluation of implants with respect to manufacturing processes, control, and service conditions now has another variable to consider and evaluate against performance.

KEYWORDS: Bioglass, Residual stress, Crystallinity, Indentation, Bioactivity

Ding Li

04/01/2010

LOCALIZED MECHANICAL DEFORMATION AND DISSOLUTION OF 45S5 BIOGLASS

By

Ding Li

Fuqian Yang
Director of Dissertation

Stephen Rankin
Director of Graduate Studies

04/01/2010
Date

RULES FOR THE USE OF DISSERTATIONS

Unpublished dissertations submitted for the Doctor's degree and deposited in the University of Kentucky Library are as a rule open for inspection, but are to be used only with due regard to the rights of the authors. Bibliographical references may be noted, but quotations or summaries of parts may be published only with the permission of the author, and with the usual scholarly acknowledgements.

Extensive copying or publication of the dissertation in whole or in part also requires the consent of the Dean of the Graduate School of the University of Kentucky.

A library that borrows this dissertation for use by its patrons is expected to secure the signature of each user.

Name	Date

DISSERTATION

Ding Li

The Graduate School

University of Kentucky

2010

LOCALIZED MECHANICAL DEFORMATION AND DISSOLUTION OF 45S5 BIOGLASS

DISSERTATION

A dissertation submitted in partial fulfillment of the
requirements for the degree of Doctor of Philosophy in the
College of Engineering
at the University of Kentucky

By
Ding Li

Lexington, Kentucky

Director: Dr. Fuqian Yang, Professor of Materials Engineering

Lexington, Kentucky

2010

DEDICATED TO MY FAMILY

ACKNOWLEDGEMENT

Firstly I would like to sincerely thank my advisor Dr. Fuqian Yang for his invaluable guidance, continuous encouragement and constructive instructions. I am grateful to Dr. John Nychka, Dr. Y. T. Cheng, Dr. Stephen Rankin, Dr. David Puleo and Dr. Richard Eitel for their helpful insight and supervision. I also appreciate the support from Dr. Yuming Zhang. In addition I want to thank all of my colleagues in the Lab: Rong Chen, Juchuan Li, Hongmei Dang, Yan Li, Ning Zhang, and Ming Liu for their helpful suggestions for my work.

In addition, I want to give my thanks to my parents for their endless love and support throughout all my life. Lastly I'd like to express my great appreciation to my Husband, Kun Qian, for bringing me and sharing with me so many wonderful moments in my life.

TABLE OF CONTENTS

LIST OF TABLES

LIST OF FIGURES

Chapter 1 Introduction and Overview

1.1 Fundamental of Bioglass

1.1.1 Concept, classification, and applications of bioglass

Bioceramics are ceramics used for the repair and reconstruction of diseased or damaged parts of the musculo-skeletal system [1], in which bioglass is a type of glass having the potential to be used as a medical implant material. Bioglass is bioactive, designed to be resorbable and slowly replaced by bone in a biological environment. In general, bioceramics can be classified by bioactivity and chemical composition. Designations include bioinert, resorble, and bioactive. Most types of bioceramics can be designed to be porous for tissue ingrowth. Examples are given in Table 1.1.

Bioglass has a range of compositions. The compositions of three common bioglasses are given in Table 1.2. [2] Nowadays, with the advancement in new processing techniques, especially sol-gel processing methods, some bioglasses can have as much as 90 wt% SiO_2 [1]. Although it is often a component in bioglass, P_2O_5 is not necessary for bioglass to exhibit the required properties [1]. If glasses have too much P_2O_5 (>6 wt%), they will probably not bond to bone [1] and also P_2O_5-free Na_2O-SiO_2 glasses have been observed by Ogino *et. al.* to form an apatite layer on their surfaces when exposed to calcium-phosphate solutions [3]. Bioglasses can be classified by chemical compositions which include SiO_2, CaO and P_2O_5, Na_2O, K_2O, MgO, Al_2O_3, CaF_2, B_2O_3 and other compositions as optional. The mechanical properties and bioactivity of bioglass are sensitive to their composition. Use as implants for repair of biological tissues, usually the hard tissues of the musculo-skeletal system, such as bones, joints, or teeth, is one of the most prevalent clinical applications of bioglass. Currently, the greatest difficultly encountered with xenotransplants (transplants between species) of bone is immune rejection by the body[4]. In past years, researchers and scholars [5], [6], [7] have attempted to overcome

the immune rejection of bone by using various techniques such as freezing, boiling, and immersion in chemicals. Another challenge for the implant materials is to replace old, deteriorating bone with a material that can function through the entire patient's life, which is to say the biomaterial needs to last for 20+ years [1]. In addition, the biological environment for implanting ceramic materials is especially harsh because of the corrosive condition of saline solutions at 37˚C and the ceramic implants must maintain stable chemomechanical properties under variable, multiaxial, and cyclical mechanical loading. Thus it is essential to identify the dissolution/corrosion behaviors of bioglass in simulated body solutions and also the related biological responses. There are several characteristics such as the composition, processing technique, porosity, surface roughness, residual stress and crystallinity which may affect the dissolution/corrosion behaviors and the biological response of bioglass in a biological environment. Some of these characteristics have been proven to favor the surface reaction and bioactivity of bioglass, while others have not been studied enough to reach a widely-accepted conclusion on the effects. In the Chapter 1, the composition, processing techniques, porous characteristics, surface roughness, residual stress, and crystallinity effects on bioactivity of bioglass will be introduced. The major goal and research emphasis will be summarized as well.

1.1.2 Bioglass reaction and definition of bioactivity

Bioglass reaction with the biological environment involves two major stages. One is the formation of a Hydroxycarbonate Apatite (HCA) layer, which is rapid and sensitive to the composition of materials. [1] The second involves the ingrowth of bone cells. For bioglasses implanted into a biological body, the reactions are sensitive to the microstructure of the implant since there are several steps related to biological actions of bones. The surface reaction steps are summarized in Figure 1.1.

Generally, when the bioactive glass is tested *in vitro*, the first stage of the surface reaction is used an indicator to characterize the *in vitro* bioactivity. The first stage

(the first five steps in Figure 1.1) occurs very rapidly on the surface of most bioglasses because of fast ion exchange of alkali ions with hydrogen ions in body fluids. [1] Although the first stage occurs rapidly, it is essential because it leads to biochemical adsorption of growth factors and a synchronized sequence of cellular events (the second stage) including action of macrophages, attachment of stem cells, differentiation of stem cells, generation of a matrix and proliferation and growth of bone, which may take a few weeks or more. [1] Cerruti's group studied the early stage ionic exchange and claimed that the cation leaching, silica network formation and phosphate reprecipitation are not sequential steps of reaction but occur at the same time. [8] In our study, we are focusing on the first stage of the surface reactions. The dissolution of the surface and the formation of the hydroxyapatite layers are used as two major indicator of the bioactivity of the bioactive glass.

Bioactivity is defined and characterized by different behaviors of biomaterials when under different environments. In the research on bioglass, the dissolution of the materials and the formation of HA layers is usually used as the indicator of bioactivity of bioglass in the *in vitro* tests. The response of an organism, especially the cell proliferation and ingrowth is usually used as the indicator of bioactivity of bioglass in the *in vivo* tests.

There are several variables that could affect the bioactivity of bioglass in different stages and ways. These variables can be classified into two types, one set of factors that favor of the formation of HCA, and the other that facilitate ingrowth of bone cells. These variables are shown in Table 1.3.

Depending on the reactions between the implanted materials and bio-tissues, the composition, porosity and pore morphology, surface roughness and morphology, residual roughness and crystallinity of bioglass can be important variables for controlling the bioactivity of bioglass. As for the composition and porosity effects, there have been conclusions of the factors that give better bioactivity. For example, higher SiO_2 content has been proved to favor surface reaction because of the high concentration of nucleating sites it generates in gel glasses [9]. High porosity and interconnected pores larger than 100 microns have been proved to be able to

facilitate ingrowth of bone cells [9], [10], [11], [12].

1.1.3 Processing techniques

To meet the requirements for various applications, more and more processing techniques have been developed since the first sinter-derived bioglass. For tissue engineering applications, a scaffold made with bioglass is required that can act as a template and guide for osseointegration including cell proliferation, cell differentiation and tissue growth, thus bioglass is usually expected to be porous and mechanically strong.

There are four different processing techniques which are mostly used in the production of bioglass materials: sintering [13], [14], tape casting and sintering (TCS) [11],[15],[16], sol-gel foaming (S-G (F)) [17] , and sol-gel processing using pore former (S-G (PF)) [12],[10], [18]. The sol-gel processing for making bioglasses is relatively newer compared to the sintering-based techniques. However, it is difficult to tell which one is better than the others because many factors can be used to evaluate the biological performance of bioglasses generated with different processing methods. For example, bioactivity, as indicated by the ability of bone cells to proliferate and grow into the implant *in vitro* and *in vivo*, is essential to determining whether a bioglass can be used as an implant to induce osseointegration. Thus, the pore size, distribution, and pore volume all contribute to the control of bioactivity. As an implant material, a bioglass should be pure, clean, and biodegradable. Ideally, the mechanical properties must match that of the bone. Sol-gel derived bioglass is generally found to have higher porosity and better mechanical properties than bioglass produced from sintering [19] . For economical reasons, the cost and productive cycle time should also be considered to ensure that the bioglass implant can be easily manufactured. The sol-gel processing techniques are usually more expensive than sintering techniques because of relatively longer production cycle.

Melt-derived bioglass including tape casting derived bioglass can match the

mechanical properties of natural bone and have a function gradient structure mimicking the structure of natural bone. Generally the melt-derived bioglass will have more advantages structurally and economically until the sol-gel processing becomes more mature.

1.2 Factors affecting the Bioactivity of Bioglass

1.2.1 Porous characteristics

1.2.1.1 Effects of porosity on mechanical properties and bioactivity

The IUPAC classification of pores according to their size is given in Table 1.4. The current understanding of bioglasses has been mainly developed based on the relative ease of formation of the HCA layers on the bioglasses surface while testing *in vitro*. Since the current direction of biomaterials research towards assisting or enhancing the body's own reparative ability[20], porosity (including the average interconnected macropore size and surface roughness) is an important parameter to understand in biomaterials because of its potential effect on the proliferation and ingrowth of bone cells.

1.2.1.2 Characterization of porous materials

Since porosity and pore size are important parameters of bioglass, precise characterization of porous characteristics is necessary. An appropriate characterization of porous materials should include an analysis of the pore size distribution, pore morphology, total porosity, thickness of different layers or porous clusters [21]. For bioglass, the interconnectivity of macropores is another important factor determining bioactivity of the material. The selection of different measurement methods must be based on the pore sizes of materials, which are listed in Table 1.5.

Mercury-intrusion porosimetry (MIP) is the standard method of measuring pore size distribution of macropores[10]. Mercury is a non-wetting liquid for almost all

substances, and consequently, it has to be forced into the pores of these materials. Pore size and volume quantification can be accomplished by submerging the sample under a confined quantity of mercury and then increasing the pressure of the mercury hydraulically. [22] As applied pressure is increased more mercury penetrates into the sample. The data obtained give the distribution of pore volume directly. With the aid of a pore physical model, a simple calculation of the dimensional distribution of the pore size can be obtained. Mercury intrusion porosimetry has been widely used in the characterization of the pores with diameters in the range from 360μm to 0.0055μm [22].

X-ray microtomography and three-dimensional image analysis are regarded as good techniques to characterize both the pore size (pore diameter ranging from 200μm to 2nm) and the interpore aperture size distribution in engineered tissue scaffolds made of bioactive glass foams [23]. X-ray microtomography measures the 3-D internal structure of a material based on variations of X-ray absorption. Hundreds of radiographs of a sample are taken at small angular increments over 180 degrees of the sample rotation. A computer algorithm inverts this data to produce a 3-D absorption map [24], [25].

Gas adsorption is a prominent method to obtain a comprehensive characterization of porous materials with respect to specific surface area, pore size distribution and porosity [26]. Pore size, pore shape and effective adsorption potential are the factors that determine the pore filling. For micropores (pore size < 2nm) the filling into pores occurs in a continuous way, while for mesopores (pore size in the range of 2nm – 50nm) the filling occurs by the pore condensation, which reflects a first order gas-liquid phase transition [27].

There are also several techniques which have been developed for determining the pore size distribution of porous materials including microscopic tools such as various gas and liquid displacement methods like capillary flow porometry[28]; quantitative methods for the pore characterization[29] are required when scaffolds are tailored for tissue engineering applications. The pore morphology is usually characterized by Scanning Electron Microscopy (SEM). Appropriate measurement

techniques should be chosen according to physical circumstance and requirement.

1.2.1.3 Control of porosity

As mentioned in section 1.1.3, porosity can be controlled by using different processing methods or using different techniques for the same processing method to achieve different pore sizes, interconnectivity, pore volume and pore morphology. Polymer particles, larger than the desired pore size, can be used in sol-gel processing method as pore formers [12],[10], [18]. By controlling the size of the polymer particles, the pore size of bioglass can be controlled as well as by adding surfactant into the sol.

1.2.2 Surface Morphology

1.2.2.1 Effects of surface morphology on bioactivity of bioglass

Since the chemical reaction to form the HCA layer always occurs on the surface of the implants, it is essential that surface roughness as well as surface morphology of bioglass be characterized in research and controlled in applications. Atomic Force Microscopy (AFM) can be used as an effective technique for characterizing surface roughness. In the measurement process, a small probe is scanned across the surface of sample to obtain three-dimensional topographic information of the sample surface[30]. The tip is scanned laterally across the surface, and the vertical movement of the tip is recorded and used to construct a quantitative three-dimensional map of surface morphology as well as the surface roughness. Compared to scanning electron microscopy (SEM), AFM provides more accurate topographic contrast, direct height measurement and require no conductive coating. Thus AFM is an important technique to collect information about surface texture.

1.2.2.2 Measures of surface roughness

The surface roughness can be described in different ways, which are generally

classified into three basic categories including: 1) statistical descriptors, 2) extreme value descriptors, and 3) texture descriptors [31]. Table 1.6 lists the roughness value measured by different approaches.

Among these descriptors, the Ra (arithmetical mean roughness of a surface) measure is one of the most common surface roughness measure adopted in engineering practice. It gives a good general description of the height variations on a surface[31]. Ra measure is the descriptor which is most likely used in research.

Different measurement techniques can be used to inspect and assess the surface roughness of materials which can be ranked into four classes. The first one is the direct measurement method which assesses surface finish by means of stylus type devices. Measurement is conducted by using a stylus drawn along the surface to be measured. The stylus motion perpendicular to the surface is registered. This registered profile is then used to calculate the roughness parameter [32].

The second is a comparison-based technique. The comparison technique uses specimens with surface roughness produced by the same process, material and machining parameters as the surface to be compared [32]. Visual and tactile senses are used to compare a specimen with a surface of known surface finish.

Some work has also been done measuring surface roughness using non contact techniques such as electronic speckle correlation method for example [33]. Finally, there are several other methods for measuring surface roughness. For example, in machine vision technique [34], in which a light source is used to illuminate the surface with a digital system to view the surface with the data being sent to a computer to be analyzed. The digitized data is then used with a correlation chart to obtain actual roughness values. In inductance method [35], an inductance pickup is used to measure the distance between the surface and the pickup. This measurement gives a parametric value that may be used to give a comparative roughness. However, this method is limited to measuring magnetic materials. In an ultrasound method [36], a spherically focused ultrasonic sensor is positioned with a non normal incidence angle above surface. The sensor sends out an ultrasonic pulse to a personal computer for analysis and calculation of roughness parameters.

1.2.2.3 Control of surface roughness

Ceramic materials are hard to machine with good control of surface roughness, so the porosity of materials is the major factor affecting the surface roughness. There are other ways to change the surface roughness of bioglass by using chemical etching, laser surface modification, and heat treatment.

During *surface etching*, the surface of a bioglass is in contact with an acid fluoride salt solution. The solution contains a complexing agent, which forms a complex with ions dissolving from the glass. An acidic fluoride solution suitable for etching must have a considerably high concentration of fluoride, which can be achieved by using a fluoride compound having as a high water-solubility as possible. A good example is saturated aqueous solution of ammonium fluoride, having an ammonium fluoride concentration of approximate 27 M [37].

The acidity of a solution should not be too strong in etching a bioactive glass [37]. Too low a pH causes uniform dissolution and gelling of the surface. A suitable pH was proven to be within the range of 1.5-5, preferably 2-5 [37] . For this reason, strong acids are not used in the etching of bioglasses.

During etching, silicon dissolves from the surface of bioglass because of hydrogen ions. Silicon ions together with fluoride ions form a water-soluble compound SiF^{62-}. [37] Calcium ions are also released, and they can form a water-soluble complex together with acid. This prevents the formation of poorly soluble Ca^{2+} compounds and their precipitates on the surface of the etched glass [37]. The etching time required for the etching depends, among other variables, on the concentration of the etching solution, temperature, composition of bioglass, and ranges from a few seconds to up to several hours.

KrF excimer *laser treatment* has been used to modify the surface topography of materials. [38] This processing technique uses a mask projection micromachining system. Surface treatment of materials with excimer laser radiation often results in formation of a rough columnar or cone-shaped surface topography, which leads to a considerable increase in surface area. As a result, the

search for a non-porous bioactive material with adequate mechanical properties and a high surface are to volume ratio, similar to porous materials, justifying the use of excimer laser surface treatment to promote control the roughning of hydroxyapatite (HA) and glass-reinforced hydroxyapatite (GR-HA). It has been shown that laser surface modification increases the surface area of HA and GR-HA [38].

Heat treatment allows evaporation of volatile species, segregation of selected ions or oxides on surface, and chemical adsorption or reaction with gases in a heat-treatment atmosphere. All of these result in the change of surface composition that can influence surface reactivity [39]. The schedule of heat treatment, including temperature and time is vital in controlling the surface roughness of the resulting materials. The heat-treatment method has been used to change the surface morphology of asymmetric PAN hollow fiber membranes [40], aluminum alloy sheets [41], polyethersulfone hemodialysis membranes [42], holographic gratings [43] and bioglass coatings [44].

1.2.3 Residual Stresses

1.2.3.1 Effects of residual stresses on bioactivity of bioglass

The bioactivity of bioglass mainly depends on the surface reaction between the biomaterial and biological environment, and consequently, control of surface conditions is essential for the success of the implant biomaterials. Besides surface roughness, localized residual stress, which can be created during processes such as heat-treatment in sintering beads, burning in the sol-gel processing, or machining, may also play an important role in determining the biocompatibility of the implanted bioglasses [45], [46].

1.2.3.2 Residual stress measurement

Because stress is not a directly measurable quantity, another quantity must be

measured from which the stress can be calculated. The most commonly used quantity is strain [47]. There are many methods available to calculate residual stress and strain as shown in Table 1.7. In the hole-drilling method, the strain response is measured from the surface by a strain gage. Then, the strain energy released can be calculated from the relation between stress and strain. To release residual stress, mechanical or electro-discharge machining (used for metallic specimen only) is used for making a hole or an annular groove which can be measured by strain gage. The residual stress field can be calculated from the acquired strain distribution as a function of depth with different algorithms or relaxation functions [47].

1.2.3.3 Indentation technique

As materials science continues progress towards studying the properties of materials on smaller and smaller scales, different techniques have been developed to quantify material behavior. Measuring mechanical properties of materials on small scales, like thin films, cannot be done by using conventional uniaxial tensile tests. As a result, techniques measuring material hardness or other mechanical properties by indenting materials with an indenter have been developed.

The original purpose of indentation tests was to determine the hardness of materials [48], and it was therefore called an indentation hardness test. Basically, hardness measurement quantifies the resistance of a material to plastic deformation. Indentation hardness tests can be divided into two classes: microindentation and macroindentation tests. Typical microindentation test use forces less than 2 Newtons (2 N). Usually microindentation provides a relative idea of material hardness instead of a fundamental material property [48]. Thus, micro hardness can only offer a comparative idea of a material's resistance to plastic deformation since varied hardness measurement techniques have varied scales.

One of the effects of the indentation load has on the indentation test is the pile-up or sink-in of surrounding material. If the tested material is work hardened it has a tendency to pile up and form a crater. If the material is annealed, it will sink in around the indentation. Both of these effects add to the error of any hardness

measurement [49]. Another effect is that the indentation left after the indenter and load are removed is known to recover or spring back slightly depending on the properties of tested materials. This effect is called shallowing [49]. This effect is due to the localized elastic recovery.

1.2.3.4 Micro-indentation hardness

In microindentation hardness test, usually a diamond indenter of specific geometry is impressed into the surface of a test specimen using a pre-set applied force. Due to the specificity, microhardness test can be used to observe change in hardness on the microscopic scale. It has been found that the microhardness of almost any material is greater than its macrohardness. The two most commonly used microhardness tests are the Vickers indentation test and Knoop indentation test.

The Vickers hardness test was developed in 1924 by Smith and Sandland as an alternative to the Brinell method to measure the hardness of materials [50]. The Vickers test is often easier to use than other hardness tests since the required calculation is independent of the size of indenter, and the indenter can be used for all materials, especially for ceramics. The basic principle, as with all common measurement of hardness, is to observe the testing material's ability to resist plastic deformation from a standard. The Vickers test can be used for all metals and has one of the widest scales among the hardness tests. The hardness unit of Vickers hardness test is the Vickers Pyramid Number (H_V) or Diamond Pyramid Hardness (DPH), and these hardness numbers can be converted into unit of Pascals. The hardness number is determined by the load over the surface area of the indentation mark and not the area normal to the force. When performing the indentation test, the distance between indents must be more than 2.5~3 times of the indent diameter apart to avoid interaction between the work-hardened regions.

The relationship between the indentation hardness and the yield strength can be approximated as [51]

$$\sigma_y = \frac{H_v}{c} \approx \frac{H_v}{3}$$

(1.4)

where c is a constant determined by geometrical factors usually ranging between 2 and 4.

It is believed that the indenter shape is capable of producing geometrically similar impressions, irrespective of size. The impression should have well-defined points of measurement, and also the indenter should have high resistance to deformation itself. Thus, a diamond in the form of a square-based pyramid satisfies all these conditions. It had been established that the ideal size of a Brinell impression is 3/8 of the ball diameter. As two tangents to the circle at the ends of a chord of 3d/8 long, intersect at 136º, this is used as the included angle of the indenter. The angle has been varied experimentally and it has been found that the hardness value obtained on a homogeneous material remained a constant, irrespective of load [52]. The H_V number is then determined by the ratio of F/A where F is the force applied to the diamond and A is the surface area of the resulting indent. The value of A can be determined from the formula

$$A = \frac{d^2}{2\sin\left(136^\circ/2\right)}$$

(1.5)

which gives:

$$A \approx \frac{d^2}{1.854}$$

(1.6)

Here d is the average diagonal length of the indenter. Hence,

$$H_v = \frac{F}{A} \approx \frac{1.854P}{d^2}$$

(1.7)

where *P* is the maximum indentation load.

A spherical indenter is another alternative option for the hardness measurement in microindentation test. The typical test uses a 10mm diameter steel ball as an indenter. For softer materials, an indenter tip of larger radius is used; for harder

materials, as indenter of smaller size is used, and for even harder materials, a tungsten carbide ball can be substituted for the steel ball. The main advantage of spherical indenters is that it causes less damage to the tested surface than that of the Vickers indenter.

For spherical indenters, the hardness, H, is calculated from the average indent diagonal length, $\bar{d}$, as:

$$H = \frac{P}{\pi \times \bar{d}^2} \tag{1.8}$$

1.2.3.5 Measurement of Young's modulus from micro-indentation

As an important quantity, the elastic contact stiffness, S, can be obtained by fitting the unloading curve and taking the tangent at the peak load (F_{max}) as the slope of the upper portion of the unloading curve ($S = dF/dh$) [53]. Using Sneddon's solution and the result given by Oliver and Pharr [54], the contact depth h_c can be calculated as [54]:

$$h_c = h_{\max} - \varepsilon \frac{F_{\max}}{S} \tag{1.9}$$

where ε is a function of the particular tip geometry (for a perfect Vickers indenter, $\varepsilon = 0.75$). Ideal area function of an indenter can be used to calculate the real projected contact area of A_p ($A_p = 24.5 h_c^2$) at the peak load. For an ideal Vickers indenter, the projected contact area of A_p is the cross-sectional area of the indenter tip at a distance of h_c from the tip apex [53].

After the S and A_p are known, the contact modulus of E can be determined as:

$$E = \frac{\sqrt{\pi}}{2\beta} \frac{S}{\sqrt{A_p}} \tag{1.10}$$

where β is a correction factor only related to the lack of symmetry of the indenter.

For Vickers indenter, β=1.0124 [55].

1.2.3.6 Measurement of Fracture toughness

The fracture toughness of a material is the ability of the material to resist crack propagation. The fracture toughness can be determined from a Vickers indentation under certain indentation loads. Several relations have been developed from the indentation load (P), elastic modulus (E), microindentation hardness (H), crack length (c) and the flexural strength (σ) [56]. The fracture mechanics of a Vickers indentation is complicated, as is the stress field surrounding the indent. The main basis of the indentation technique concerns the crack shape; cracks are assumed to be radial-median cracks beneath the indent, with a center point force leading to crack opening [57] [58]. Satisfying these conditions leads to a specific stable equilibrium relation between the applied load, P, and the crack size, c [59]:

$$P = kc^{3/2}$$

(1.11)

where k is a constant of proportionality.

For the indent of an elastic-plastic material, the indentation following load and unloading creates a crack whose size is related to the stress intensity factor as [59]:

$$K_I = \frac{\chi P}{c^{3/2}} \quad (P > P_C,\ c >> a)$$

(1.12)

where K_I is the stress-intensity factor for the radial-median crack in an ideal case, χ is a dimensionless constant, and P_c is the critical contact load.

For the applicability of indenters used in the indentation of brittle materials, the calculation of fracture toughness using Eq. (1.12) has been evaluated to determine the constant of proportionality, χ from a mechanics analysis of a point load caused by the Vickers indenter tip [60]. The result of such analysis leads to the following, now widely accepted, relation for determining the Mode I fracture toughness, K_{Ic}, from indentation- induced radial median cracks:

$$K_{IC} = \delta\left(\frac{E}{H}\right)^{1/2}\left(\frac{P}{c^{3/2}}\right)$$

(1.13)

where E is the Young's modulus of the materials, H is the hardness, and δ is a dimensionaless indenter-geometry constant (~ 0.016+0.004 for radial-median cracks created by a Vickers indenter [61]) .

1.2.3.7 Control of residual stresses

In order to study the effect of residual stress on the bioactivity of bioglass *in vitro* or *in vivo*, the magnitude of residual stress should be able to be controlled. Actually, uncontrolled residual stress is always undesirable. However residual stress has been used in various fabrication processes. For example, toughened glass and pre-stressed concrete depend on them to prevent brittle failure [62]. Similarly, a gradient in martensite formation creates residual stress in some swords with particularly hard edges (notably the katana), which can prevent the opening of edge cracks [63].

Residual stress exists in the bulk of a material , which can be produced by heterogeneous plastic deformation, thermal contraction, and phase transformation induced by manufacturing processes [64]. Indentation especially micro-indentation using a Vickers indenter is widely used in dental materials to produce well controlled mechanical residual stress[65], [66] .

Because ceramics and glasses are always hard and brittle, cracks size can be used to determine the residual stress. The formation of plastic deformation, elastic deformation and cracks are schematically shown in the Figure 1.2 [67].

From the crack size, the fracture toughness, K_c, can be calculated from the equation:

$$K_c = Y(\theta)\sigma_f (c)^{1/2}$$

(1.14)

where $Y(\theta)$ is a geometric factor that has a value of 1.65 for an indentation induced

flaw with local residual stress [68], 1.24 for flaws without local residual stress and σ_f is the calculated flexural strength. For equivalent semicircular flaw of depth of "a" and half width of "b" [69], c is the crack size $\left[c = (ab)^{1/2}\right]$ [68]. The residual stress is calculated as [70]:

$$\sigma_r = \left[Y\left(2/\pi^{1/2}\right)\sigma_a c^{1/2} - K_c\right] / \left[Y\left(2/\pi^{1/2}\right)c^{1/2}\right]$$

(1.15)

where σ_r is the residual stress, σ_a is the mechanically induced stress at failure, and K_c is the fracture toughness of the brittle materials.

Generally, compressive residual stress has a beneficial effect on the fatigue life and stress corrosion because it delays crack initiation and propagation. On the contrary, tensile stress reduces mechanical performance of materials [64].

The manufacture of successful and safe biomedical devices is based on the supposition that all processing effects and variables are well understood and controlled, resulting in a pure, sterile, and well-performing product. As in any manufacturing industry, there are certain control variables that remain unmeasured. One such variable is residual strain. The most common methodology used to relieve residual strain and stress from processing is heat treatment. However, a complication arises in biomaterials, because when in service, biomaterials cannot be easily removed from biological body for heat treatment. Thus, if residual strain develops during service in a biomedical system, or is present and not fully relieved during manufacturing, it will have significant effect on biological behavior of the materials. Thus, understanding the relationship(s) between bioactivity and residual strain (stress) remains important in making progress in developing and specifying materials for use in biomedical system.

While the mechanical properties of bioactive glasses and bioglass composites have been well studied [71], the interrelation between residual strain and bioactivity have received little attention. Other fields, such as metals and ceramic coatings research, have investigated the effect of residual strain on dissolution rate, known as

chemomechanical effect. Biomaterials, such as hydroxyapatite coating on Ti-6Al-4V substrate, have been found to degrade by cracking and faster dissolution in cyclic bending [72] and a thermodynamic model proposed for such materials [46] predicts faster dissolution under tensile stress. Thus, it needs to understand the interplay between residual strain and bioactivity.

1.2.4 Crystallinity

1.2.4.1 Effects of crystallinity on the bioactivity of bioglass

Crystallinity is the degree of structural order in a solid, often represented by a fraction or percentage as a measure of how likely atoms or molecules are to be arranged in a regular pattern, namely into a crystal. Amorphous or less crystalline materials are found to be more resorbable, and there is evidence to suggest that they may be more beneficial for early bone ingrowth than materials with high crystallinity [73], [74]. Different research groups have obtained different results regarding to the effect of crystallinity on formation of HCA layer. Some results indicated that crystallization did not inhibit the development of a crystalline HCA layer, but the onset time of crystallization increased from 10 h for the parent glass to 22 h for 100% crystallized glass-ceramic [75]. The rate of surface reactions is slower when the percentage of crystallization is more than 60% [75]. It was also reported that a well established crystalline hydroxyapatite layer formed after about 1 day in simulated body fluid (SBF) on bioceramic with 100% crystallinity, similar to that formed on the surface of amorphous bioglass surface [73], [74]; while thin layer of crystalline hydroxyapatite was formed on glass-ceramic with 87% crytallinity only 2 hours in SBF [73].

No matter how crystallinity affects bioactivity, it is certainly an important factor that can determine the biodegradation rate of the implant materials. The control of all the factors such as crystallinity, porosity, surface morphology can result in the better materials for tissue engineering scaffolds.

1.2.4.2 Crystallinity measurement

Different analytical methods have been developed to measure the crystallinity of materials. For simple binary systems, the most frequently used quantitative methods include Fourier-Transformed Raman (FT-Raman) [76], [77], near-infrared (NIR) [78], solid state nuclear magnetic resonance (NMR) [79], Fourier-Transformed infrared (FTIR) [80], and X-ray powder diffraction (XRPD) [81]. Also crystallinity can be measured directly by using diffraction techniques, such as X-ray diffraction, in which greater crystallinity yields a sharply diffracted peak. To get a more in-depth knowledge of crystallinity, sometimes Differential Scanning Calorimetry (DSC) and SEM measurements are also used. When using XRD method, quantitative measurement can be made by calculating the percentage of total peak area above the amorphous halo curve. The error of the XRD measurement mainly comes from mixing homogeneity and preferred orientation of crystalline particles during the preparation of the powder bed [82]. Quantitative crystallinity estimation using DSC has recently been reported, and crystallinity has been calculated from the difference between the heat released for crystallization and the heat required for fusion of the sample divided by the estimated heat of fusion of a 100% crystalline sample [83], [84]. The error for the DSC measurement is mainly from two sources, one is the mixing homogeneity and sampling and the other is the possible phase transition during the DSC-heating process.

1.3. Experimental objectives and scope of this dissertation

To be an implant material, bioglass must have good bioactivity and proper mechanical properties that match those of bone. Thus, the porous characteristics and surface morphology that affect the bioactivity and mechanical properties of bioglass are vital characteristic for bio-applications.

According to the reactions between bioglass implants and their environmental

conditions, the compositions, porosity and pore morphology, surface roughness and morphology, surface residual roughness and crystallinity of bioglass are all important variables to that can be engineered to control the bioactivity of bioglass.

As for the composition and porosity effects, there have been well-established and widely-accepted conclusions of getting better bioactivity. For example, as mentioned previously higher SiO_2 proved to be able to favor the surface reaction because of the high concentration of nucleating sites in gel glasses [7]. Higher porosity and interconnected pores larger than 100 microns proved to be able to induce better ingrowth of bone cells [7, 12, 15, 16].

Some of the characteristics of bioglass such as the surface roughness and the crystallinity have received less attention before and different groups have even reported opposite results or proposed different hypotheses about their effects on bioactivity. It has been shown that the correct roughness of the microparticle surface has favorable effects on the attachment of the proteins to the biomaterial surface [19]. However, it is still unclear how the surface roughness affects the overall bioactivity of the bioglass materials in particular the effects of surface roughness on cell interactions [20]. Hench and Filho showed that bioactivity slowed by a factor of 2 (in crystal line vs amorphous bioglass) [22], while Suominen and Juhanoja [13] reported that crystallinity has no effect on bioactivity. The difference may be caused by different definitions of bioactivity, or differences in the experimental details. More and systematic studies are required to support either of these conclusions.

So far few groups have researched the relationship between residual stresses and the bioactivity of bioglass, but residual stresses do affect the corrosion and dissolution of metal material in significant ways [24]. Generally compressive residual stress has a beneficial effect on the fatigue life and stress corrosion of materials; tensile stresses reduce mechanical performance of materials [23]. Some work has been performed on residual stress and dissolution of other bioceramics, which showed that the rate of supernatant species (OH- for hydroxyapatite [24]) going into solution is affected by the sign of residual stress. On the other hand, compressive stresses should lower dissolution rates for bioceramics.

Residual stress and crystallinity are important process parameters whose effects can hardly be avoided in the production of bioglass implants. The most common methodology employed to relieve residual strains and stresses from forming, manufacturing, or service use are heat treatments. However, many biomedical devices cannot be scheduled for maintenance, such as heat treatment, because once put in service, biomedical materials cannot be easily removed from the body. Thus, if residual strains develop during service in a biomedical device, or were present and not fully relieved during manufacture, it is difficult to predict the behavior of the materials in vivo as a function of such residual stress/strain. Because residual strain can affect the mechanical behavior of all materials, understanding the relationship between bioactivity and mechanical properties remains important in making progress in developing and specifying materials for use in biomedical devices. The mechanical properties of bioactive glasses have been found to be insufficient to result in long lifetimes in vivo [19] and thus load-bearing applications using monolithic materials have been limited. Glassceramic composites are expected to afford some gains in mechanical performance, especially fracture toughness, over the glassy forms without sacrificing much in terms of bioactivity. Long-term understanding of residual stress effects will aid in the development of such novel biomaterials.

Based on the unknown effects of stress and crystallinity in bioglass, there are several objectives of this dissertation work. They include the evaluation of bioactivity through the dissolution of bioglass and the formation of HCA layers; the measurement of residual stress; understanding effectsof residual stress on the dissolution of bioglass in various chemical solution; and understanding the effects of crystallinity on the dissolution and precipitation of bioglass. The variables which are studied in our work and the related quantification and characterization methods of bioactivity are given in Table 1.8. To study the effects of residual stress and crystallinity, several experimental routes are designed and shown in Figure 1.3. The quantitative measurement of the residual stress effect on dissolution of bioglass will be an important addition to current knowledge in biomaterials.

For most crystalline materials, diffraction techniques such as X-Ray and neutron diffraction can be used to measure the structure and even residual stress of bulk materials. However for amorphous materials with local residual stress, such as the bioglass samples used in our experiments, it is obvious that the diffraction methods cannot be applied.

In this case, micro-indentation can be used to measure the local residual stress. The residual stress can be calculated from the equation [85] (1.16) below,

$$K_c = \chi \frac{P}{c^{3/2}} + \frac{2}{\sqrt{\pi}} \sigma_R \sqrt{c} \tag{1.16}$$

where K_c is the local fracture toughness of the material, P is the indentation load, and c is the crack length between the indent center and the crack tip. For experiments which satisfy the two premises, (1) that the cracks are half-penny in shape, and (2) that well-developed indenter cracks are equivalent to half-penny cracks centrally loaded with a crack-opening point force [86], [87], χ is a constant related to the Young's modulus and hardness of the material (to be discussed in Chapter 3).

In this work, miroindentation at various indentation loads, with either a Vickers or spherical indenter, are used to produce local residual stress on the surface of bioglass. Small secondary micro-indents with relatively small indentation loads are made around the primary large indent. Stress measurement is possible at these secondary indents since the residual stress caused by them is negligible compared to the residual stress caused by the primary indents. The residual stress created by the primary indents then is quantified from the indentation test.

At the same time, the crystallinity effect on the dissolution and precipitation of bioglass is also studied. The crystallinity is controlled by heat-treatment. XRD is used to quantify the percentage of the crystallinity degree of the heat-treated bioglass. Microindentation is performed on the crystallized bioglass to examine the effects of residual stress and crystallinity on the dissolution and precipitation of bioglass 45S5.

Characterization of the dissolution behavior is based on the observation of SEM images. The dissolution rate of the indented bioglass in phosphate buffer solution is

related to the growth and widening of the indentation-induced cracks. The effect on the "*in vitro* bioactivity" is quantified by measuring the thickness change of the HCA layer on bioglass.

A major goal of our research is to improve mechanical performance without compromising biological response of bioactive glasses. Two possible strategies to improve fracture toughness are possible: partially crystallize the glass to form a glass-ceramic to lengthen the crack path, or induce residual stress to suppress crack formation and growth. These concepts are not new in the fracture behavior of brittle solids, but a fundamental understanding of how dissolution and bioactivity are related to such microstructural mechanisms is not yet well developed, and provides motivation for our work.

The full potential of bioglass will not be fully realized [88] until the effects of residual stress and crystalinity on the bioactivity of bioglass can be determined in a quantitative manner. In this dissertation, the effects of localized residual stress on the dissolution and bioactivity of bioglass 45S5 are shown in chapters 3, 4, and 5. The dissolution behavior of fully crystallized bioglass 45S5 is discussed in chapter 6. The local precipitation and formation of calcium phosphate on bioglass 45S5 is discussed in chapter 7. All these studies contribute to the understanding of the relationship between mechanical performance and biological response of bioglass 45S5 and also establish the foundation to improve the mechanical properties besides the fracture toughness without sacrificing the bioactivity. The work also provides a rational basis for characterizing the effect of mechanical deformation on the biofunctionality of bioglass. Based on the work, the feasibility to locally adjust residual stresses and crystallinity before implantation to alter bioactivity becomes possible to be used as a strategy for creating gradients of bioactivity on implants to prevent against premature failure in regions where failure probability is high.

1 fast ion exchange of alkali ions with hydrogen ions from body fluids	0h
2 network dissolution	
3 poly-condensation of SiOH + SiOH(Si-O-Si)	1h
4 adsorption of amorphous $Ca+PO_4+CO_3$	
5 crystallization of hydroxyl carbonate apatite (HCA)	2h
6 adsorption of biological moieties in HCA layer	10h
7 action of macrophages	20h
8 attachment of stem cells	
9 differentiation of stem cells	100h
10 generation of matrix	
11 crystallization matrix	
12 proliferation and growth of bone	

Figure 1.1. Steps of bioglass surface reaction stages [1]

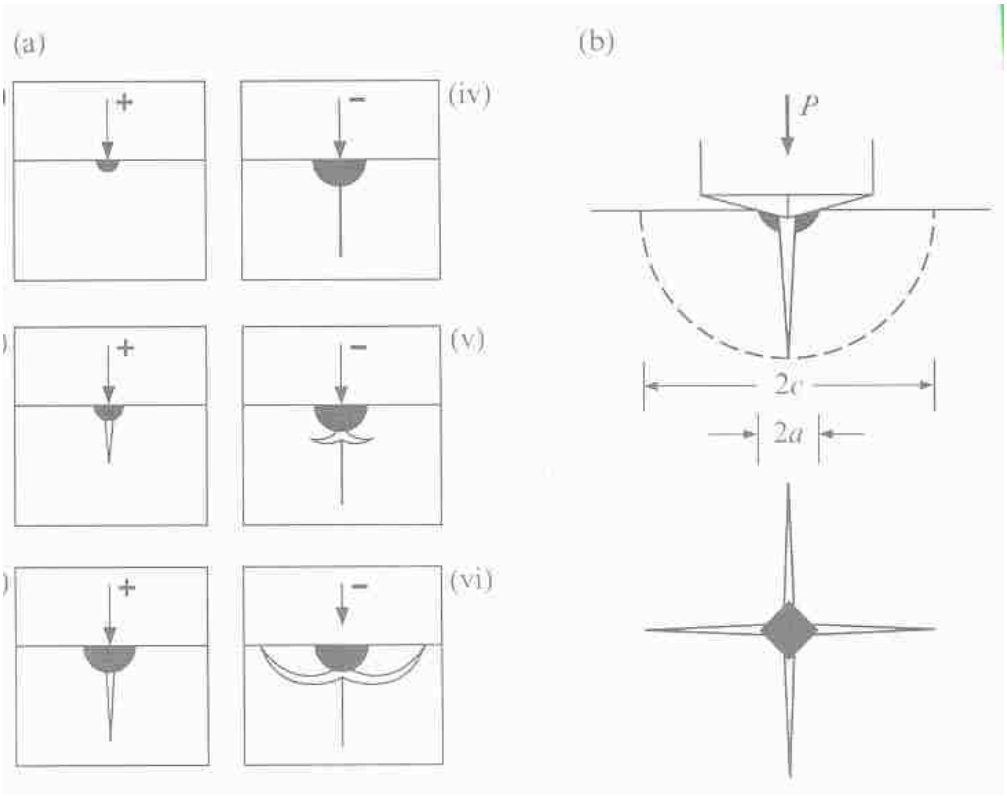

Figure 1.2. Radian-median and lateral crack systems. (a) Evolution during a complete loading (+) and unloading (-) cycle. Dark region denotes irreversible deformation zone. (b) Geometrical parameters of the radial system [67]. (With the permission of Cambridge University Press)

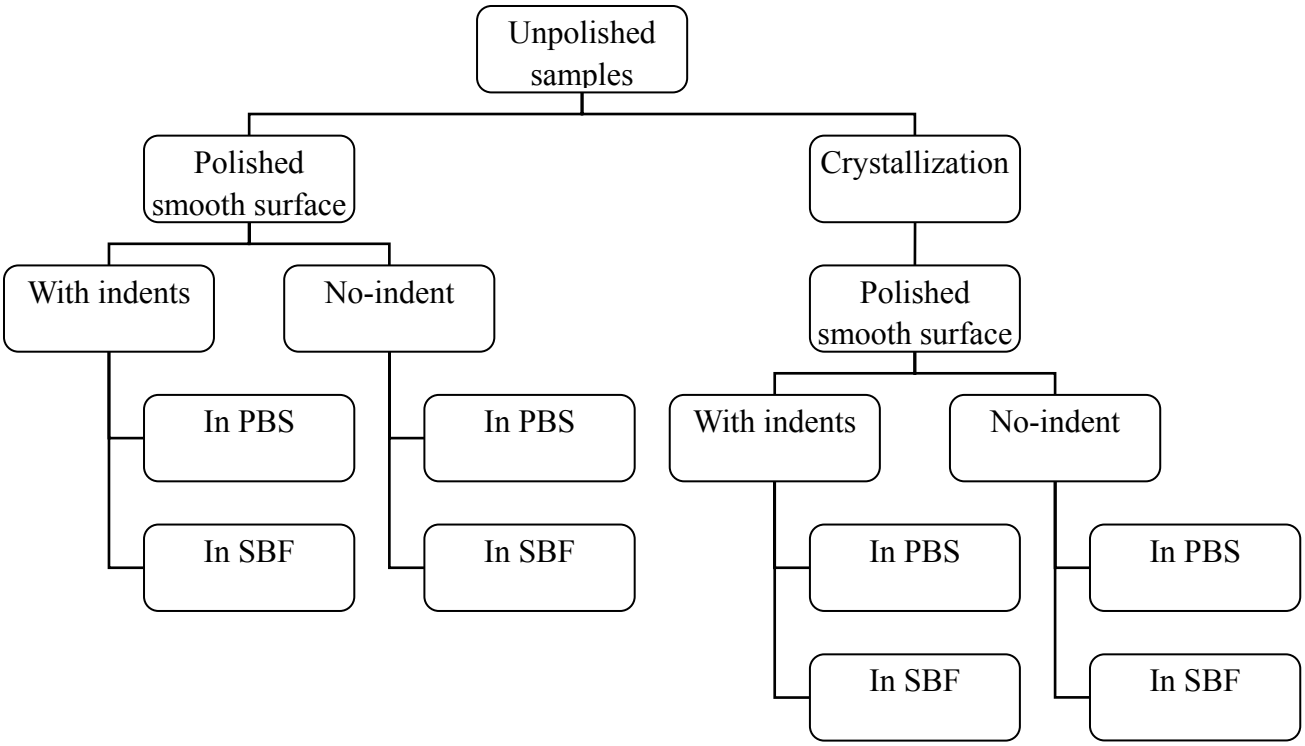

Figure 1.3. Experimental plan for the preparation of samples with variable levels of residual stress and crystallinity

Table 1.1. Examples of classified bioceramics

Bioinert	**Resorbable**	**Bioactive**	**Porous for tissue ingrowth**
Alumina, Zirconia	Tricalcium-phosphate	Hydroxyapatatite (HA), Bioactive glasses, glass-ceramics	HA-coated metals

Table 1.2. The compositions of three common bioglass (in mol%)

	Si_2O	**Na_2O**	**CaO**	**P_2O_5**
45S5	46.1%	24.4%	26.9%	2.6%
58S	60%	-------	36%	4%
77S	80%	-------	16%	4%

Table 1.3. Variables affecting bioactivity of bioglass

Variables in favor of formation of HCA
Compositions (more SiO_2, less P_2O_5) ; Rough surface for Itala group [89] or no effect from Saito group [90] ; Residual stresses; Crystallinity
Variables to facilitate ingrowth of bone cells
Porosity; Interconnected pores (with diameters greater than 100μm for tissue growth)

Table 1.4. Definitions of pores according to the pore sizes (IUPAC classification)

Definition	Pore Diameter (μm)
Micropore	≤ 2
Mesopore	2-50
Macropore	> 50

Table 1.5. Measurement methods for different types of pores

Pore type	**Measurement technique**
Micropore	Adsorption techniques [91]
Mesopore	Adsorption or X-ray micro- tomography [91], [92]
Macropore	Mercury intrusion porosimetry (MIP) [93], X-ray microtomography [92]

Table 1.6. Roughness value measured in different ways

Statistical descriptors	Extreme value descriptors	Texture descriptors
Average behavior of the surface height	Isolated events	Variations of the surface based on multiple events
average roughness	maximum peak height	correlation length
root mean square roughness	maximum valley height	NA
skewness	maximum peak to valley height	NA
kurtosis K	NA	NA

Table1.7. Residual Stress Measurement Methods

Mechanical methods	Hole drilling, curvature measurements, and crack compliance
Diffraction techniques (Non-destructive methods)	Electron, X-Ray and neutron diffraction
Other methods that are being developed	Piezospectroscopy photoelastic methods, magnetic, ultrasonics, and thermoelastic techniques

Table 1.8. Quatification variables and characterization methods

Quantification variables	**Characterization method**
Residual stress	Micro-indentation and nano-indentation
Crystallinity	X-ray diffraction,
Dissolution rate	SEM, Crack extension, Crack tip broadening
HCA layer thickness	SEM, EDS

Chapter 2 Anelastic Indentation Recovery of Bioglass at Room Temperature

2.1 Introduction

The understanding of the near-surface mechanical behavior of bioactive materials is of practical importance for biomedical applications of bioactive materials in the reconstruction and substitution of bone and tooth[94], [95]. Interacting with the surrounding-biological tissues through chemomechanical contact deformation, bioactive glasses are designed to be replaced slowly by the bone growth through bio-resorbable process involving the formation and growth of a biologically active apatite layer. This generally requires that the bioactive glasses maintain reasonable mechanical strength, geometrical shape, and bioactivity under the action of external mechanical loading.

The shape recovery of materials following contact deformation includes elastic recovery and anelastic recovery. The anelastic recovery has been reported for metallic materials[96], [97],[98], [99, 100], polymers[99], [101] [102],[103], [104] and glasses [99]. Most of these investigations focused on the shape recovery at higher temperature than that for the contact deformation. Yang and Li [101] and Yang et al. [103] studied the impression recovery of amorphous polymers with the shape recovery being evaluated at temperatures the same as that for the impression deformation. However, no prior work records the shape recovery of glasses at room temperature. Recently, Everitt et al. [105] , in a preliminary study, observed the bone recovery following microindentation of wet bone. They suggested that the bone recovery was due to viscoelastic behavior of the wet bone. Unfortunately, they did not provide detailed information on their study.

Bioactive glasses have been gradually used as the implant materials for bone replacement for more than two decades. The advantages of using bioactive glasses, such as bioglass 45S5 in the bone replacement include: 1) formation of hydroxyapatite, an inorganic material similar to the major component of the

inorganic phase in bone, and 2) Young's modulus being relatively comparable to that of cortical bone. However, the weak mechanical strength of bioactive glasses has limited their use in various load-bearing conditions. Considering the applications of bioactive glasses in bone repair, augmentation, and substitution, it is important to examine if there exists shape recovery in bioactive glasses for maintaining reasonable geometrical configuration at room temperature, similar to the bone recovery following the contact deformation.

Based on the study of contact deformation, indentation test were developed as a technique to characterize the near-surface mechanical behavior of materials. The advantages of using the indentation test include: 1) the use of a small amount of materials and 2) the evaluation of local deformation of materials of small scale. The evolution of the residual indentation imprints can be quantified by various microscopy techniques. It is known that localized mechanical deformation in a material can be created by an indentation. Such a localized deformation can change the geometrical configuration of a bioactive material and the response of biological tissues to the bioactive material, which in turn alters local biofunctionality of the material. The goal of this thesis is to investigate the geometrical response of bioglass 45S5 to localized mechanical deformation (i.e., the anelastic indentation recovery, at room temperature, using the microindentation technique). The changes of the impression size and the indentation depth with time are examined as a function of the indentation load. A phenomenological model is proposed to explain the anelastic indentation recovery.

2.2. Experimental

Bioglass 45S5 (45%SiO_2, 24.5% Na_2O, 24.5% CaO, 6% P_2O_5, in weight percent) of 10 mm in diameter and 3 mm in thickness was prepared from an annealed rod of 10 mm in diameter. The samples were ground and polished, using isopropyl alcohol (IPA) as a lubricant/coolant, during which the samples were cleaned between

polishing stages with IPA. After final polishing, the polished samples were cleaned in an ultrasonic bath for 20 minutes in acetone, then IPA, and finally ethyl alcohol and were immediately dried with compressed air. The samples were dehydrated for at least one day and later were annealed at 350ºC for 2 hours and furnace-cooled to room temperature before indentation.

Micro-indentations were made on the polished surface of the bioglass samples on a Micro-Combi Tester (CSM Instruments, Needham, MA), using a diamond spherical indenter of 50 μm in diameter. The peak indentation load varied from 50 mN to 500 mN, and both the loading and unloading times were 30 seconds. There was no holding period at the peak indentation load. Arrays of indents were made, with a minimum of 5 indents per peak indentation load (spaced at least 3 times of the indentation size away from each other).

To evaluate anelastic indentation recovery, two different unloading processes were carried out. In the first type of unloading process, the indentation load was completely removed. The size of the imprint marks was measured as a function of time using a light optical microscope. In the second type of unloading process, the indentation load was reduced to 5 mN, which was maintained for 1 hour before completely removing the indentation load. This maintained the intimate contact between the indenter and the sample during the indentation recovery. The displacement of the indenter was recorded as a function of time to evaluate the rate of the indentation recovery.

2.3 Results and Discussion

For the indentations using the first type of unloading process, the change of the imprint size with time was monitored using a light optical microscope after completely removing the indentation load. Figure 1 shows the shrinking of the imprint size for the indentation made by an indentation load of 500 mN. Obviously, the imprint mark shrank with time, demonstrating the behavior of shape recovery.

The imprint marks created by various indentation loads became invisible by the light optical microscope after 12 hours as in figure 2.1.

To evaluate the recovery rate, the second type of unloading process was used. The displacement of the indenter was monitored as a function time. Figure 2.2 shows the time dependence of the indenter displacement for various peak indentation loads. After unloading to the indentation load of 5 mN, at least 10 times less than the peak indentation loads, the indenter remained in intimate contact with the bioglass. Spontaneous depth recovery occurred, that eventually pushed the indenter back to the position corresponding to the almost deformation-free state. A linear dependence between the indentation depth and time was observed. For the indentations made by the indentation loads larger than 300 mN, much long time (more than several hours) was required for the indentation depth to fully recover to the almost deformation-free state. In addition, the indentation depth became a nonlinear function of time after the linear period. No complete test of the indentation-depth recovery was performed in the present study for the indentations made by the indentation loads larger than 300 mN.

Figure 2.3 shows the dependence of the recovery rate of the indentation depth on the indentation loads. For the indentation loads less than or equal to 300 mN, the recovery rate was calculated from the curves of complete recovery, and for the indentation loads larger than 300 mN, the recovery rate was calculated from the curves of the linear period immediately following the unloading. The recovery rate decreases with increasing the indentation load under the indentation condition.

Using dimensionless analysis, Chen et al. [106] obtained the anelastic energy dissipated in an indentation loading-unloading cycle, E_p, as

$$E_p = AF_m^{(m+1)/m} \tag{2.1}$$

where A is a constant dependent on the mechanical properties of materials and the surface profile of indenter, F_m is the peak indentation load, and m is the Meyer index. From the result given by Yang et al. [107], one obtains the size of the anelastic

deformation zone underneath the indenter, c, as

$$c = \left(\frac{3F}{2\pi\sigma_y} \right)^{1/2}$$

(2.2)

where σ_y is the compressive yield stress of the material. Using Eqs. (2.1) and (2.2), the average anelastic energy per unit volume over the anelastic deformation zone, U_p, can be approximately calculated as

$$U_p = \frac{3E_p}{4\pi c^3} = A(\frac{\pi\sigma_y}{6})^{1/2}\sigma_y F_m^{(2-m)/2m}$$

(2.3)

It is generally believed that the strain energy stored in the anelastic deformation zone is a portion of the anelastic energy dissipated in an indentation loading-unloading cycle. Thus, the average density of the stored strain energy, U_s, can be expressed as

$$U_s = \alpha\sigma_y^{3/2} F_m^{(2-m)/2m}$$

(2.4)

where α is a constant dependent on the mechanical properties of the material and the surface profile of indenter. The driving force for the indentation recovery is the derivative of the stored strain energy, dU_s / dc, which is calculated from Eq. (2.4) as

$$\frac{dU_s}{dc} = \frac{dU_s}{dF_m} \cdot \frac{dF_m}{dc} = \frac{\alpha(2-m)}{m} \left(\frac{2\pi}{3} \right)^{1/2} \sigma_y^2 F_m^{(1-m)/m}$$

(2.5)

To the first order of approximation, one can express the recovery rate of the indentation depth, $\dot{x}$, as a power-function of the driving force,

$$\dot{x} = \beta \left(\frac{dU_s}{dc} \right)^n = \chi\sigma_y^{2n} F_m^{n(1-m)/m}$$

(2.6)

where β and χ are two constants, and n (>0) is the exponential index of the driving force. The recovery rate of the indentation depth is a power-function of the

peak indentation load.

In general, $1 < m \leq 2$. Equation (2.6) suggests that the recovery rate of the indentation depth decreases with increasing the peak indentation load, which is supported by the experimental results shown in Fig. 3. Using curve-fitting, one obtains $n(m-1)/m = 1.16$. Depending on the Meyer index, a nonlinear dependence of the depth-recovery on the indentation load is expected.

2.4 Summary

In summary, the anelastic indentation recovery of the bioglass 45S5 was observed at room temperature from the depth recovery and the shrinking of the imprint marks. The indentation recovery was a function of the indentation load. The depth recovery rate decreased with the increase in the indentation load. A phenomenological model was developed, assuming that the driving force for the indentation recovery was a function of the stored strain energy over the anelastic indentation deformation zone. The depth recovery rate was a power-function of the derivative of the stored strain energy with respect to the size of the anelastic indentation deformation zone, which led to a nonlinear dependence of the depth recovery rate on the peak indentation load. Such a relation was supported by the experimental results.

It is known that the bioactivity of bioactive glasses depends on the dissolution of materials and the formation and growth of apatite layer. There exists chemomechanical interaction between biological tissues and bioactive glasses, that plays an important role in the dissolution of materials and the formation and growth of apatite layer. It has been demonstrated that the dissolution of materials is a function of local stress state [1, 2]. The anelastic recovery in 45S5 bioglass allows the stress relaxation through the shape recovery, which reduces the magnitude of local stress due to the contact between the surrounding biological tissue and the implanted bioglass and possibly minimizes the effect of local stress on the bioactivity of bioglass. Combining with the stress effect on the dissolution behavior of bioactive

materials, one can control the bioactivity and biofunctionality of bioactive glasses in the reconstruction and substitution of bone and tooth through the control of local stress and anelastic recovery potentially to achieve the best clinic result.

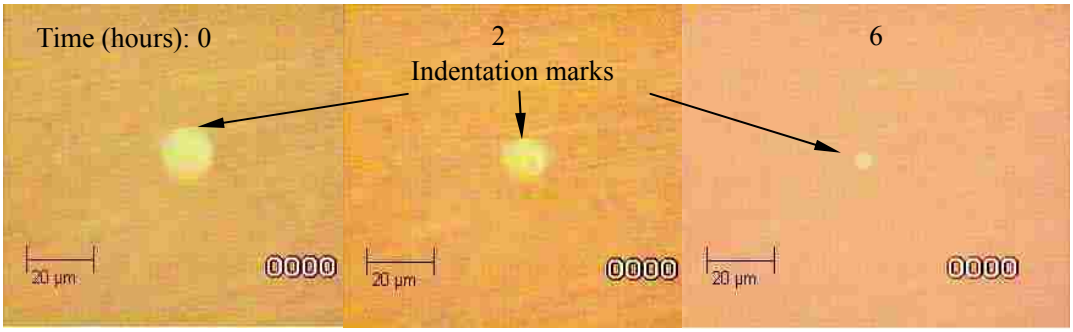

Figure 2.1. Change of the size of an imprint mark with time (maximum indentation load: 500 mN)

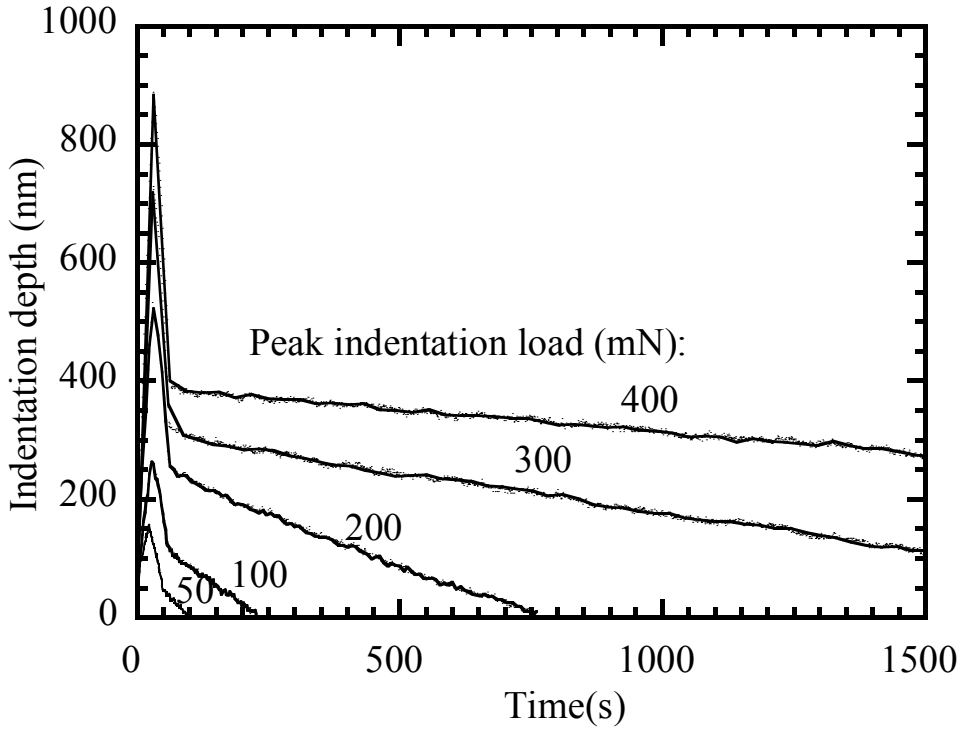

Figure 2.2 Indenter displacement *versus* time curves for various indentation loads.

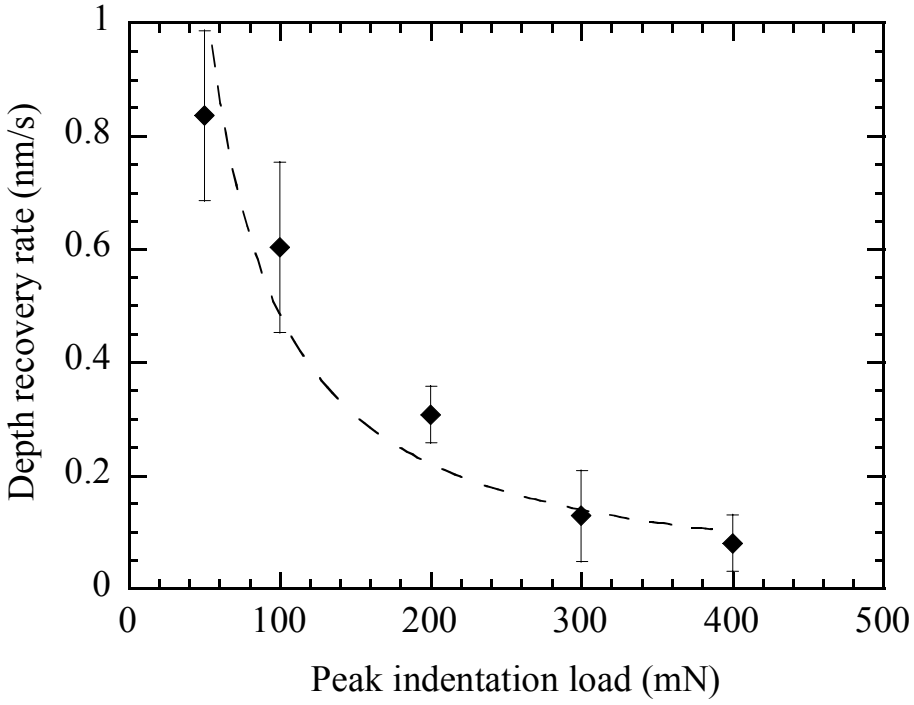

Figure 2.3. Dependence of the recovery rate of the indentation depth on the peak indentation load.

Chapter 3 Surface Morphological Changes Accompanying Dissolution of Bioactive Glass: Effect of Residual Stress

3.1. Background

The interaction of materials with fluid environments has long been studied. The effects of composition of the material and fluid are very important as is evident in materials selection for a industrial applications involving dissolution (corrosion). Often, times there are certain operating regimes in which materials behave differently due to temperature, pressure, composition of the contacting fluid, or stress. The latter variable is of interest in this study, that is relevant to biomedical device and implant applications where service loads and or residual stresses from processing or phase transformations exist, especially for biomaterials that are designed to dissolve and resorb, such as bioactive glasses.

The dissolution behavior of bioglass is dependent on glass composition [108], surface conditions such as chemical [109] and charge modification conditions [110], dose [111] , solution composition [112], [113], and crystallinity [114], [115]. A missing variable in this class of materials has been mechanical stress. The response of a material due to interaction with the environment may take three forms: no effect, the chemomechanical effect (CME), or the mechanochemical effect (MCE). CME is a chemical interaction causing a difference in mechanical performance, and MCE is summarized by mechanical action causing a different chemical response, which has been studied in other materials systems [116], [117], [118], [119], [120]. In our case, the focus is on CME: the residual stress altering the chemical dissolution.

3.2. Experimental

3.2.1 Sample Preparation

A cast and annealed rod of bioactive glass (bioglass 45S5) rod (45wt%SiO_2, 24.5wt% Na_2O, 24.5wt% CaO, 6wt% P_2O_5), 10mm in diameter, was supplied by MO-SCI Specialty Products, L.L.C. (Rolla, MO, 65402). Discs were sectioned from the rod using a slow speed diamond wafering blade into 3mm thick sections using isopropyl alcohol (IPA) used as a lubricant/coolant. Grinding was performed on silicon carbide paper in the sequence P500 (360grit), P600 (400grit), P800 (500grit), P1200 (600grit), P2400 (800grit), and P4000 (1200grit). Grinding was performed on the laboratory benchtop by hand to prevent thermal shock with isopropyl alcohol (IPA) used as a lubricant/coolant. Polishing was performed on a short nap cloth using diamond pastes in the sequence 6, 3, 1, and 0.25μm with an oil based lubricant. Discs were cleaned in between polishing stages with IPA and, after final polishing, were cleaned in an ultrasonic bath for 20 minutes each in acetone, then IPA, and finally ethyl alcohol. Samples were immediately dried with compressed air followed by desiccation for at least one day before indentation.

3.2.2Indentation

Micro-indentations were made on the polished surfaces of the bioglass samples using a diamond Vickers indenter on a Micro-Combi Tester (CSM Instruments, Needham, MA). The maximum indentation loads (P_{max}) varied from 30mN to 2000mN (30mN, 50mN, 70mN, 90mN, 100mN, 150mN, 200mN, 300mN, 400mN, 500mN, 2000mN). The loading rate was fixed at 200mN/min with no holding time at maximum load. The loading-unloading curves were recorded, and the sizes of the indentation marks and the crack lengths were measured through an optical microscope directly after testing. Samples were stored in a desiccator following indentation. Arrays of indents, with a minimum of 5 indents per maximum load

(spaced at least 3 indent diameters away from each other), were placed on equivalent specimens prior to *in vitro* testing.

3.2.3 Immersion *in vitro*

Samples were placed, indent side up, in ~1L of phosphate buffer solution (PBS) maintained at 37°C in an agitated water bath for 1, 3, 5, 7, 9, 14, and 21 days. The PBS itself was not agitated, and was sealed to prevent contamination and evaporation. For each batch of PBS used, 5mL of magnesium chloride solution (3.8g $MgCl_2$ in 100mL of de-ionized water (DI-H_2O)) and 1.25mL of potassium dihydrogen phosphate solution (3.4g KH_2PO_4 in 50mL DIUF-H_2O, diluted with 50mL DI-H_2O to make 100mL, with trace 1N sodium hydroxide to maintain pH 7.2) was added to 1L DI-H_2O.

3.2.4 Materials Characterization

X-ray diffraction of the as received bioglass was performed using a Bruker AXS diffractomer (Siemens), scanning between 10 and 80° 2θ at a rate of 1°/minute with Ni filtered Cu Kα radiation. Scanning electron microscopy (SEM), with energy dispersive x-ray capability (EDS) was performed on a Hitachi S3200 instrument. Bioglass discs were gold-palladium coated prior to SEM and were not re-immersed in PBS. All time-lapse SEM studies were performed on equivalent specimens of bioglass. Samples were washed, dried, and kept in a desiccator between characterization studies.

3.3. RESULTS AND DISCUSSION

3.3.1 Indentation Characteristics

Brittle materials may form three different types of cracks when indented with a

Vicker's indenter: 1) Palmqvist cracks (cracks emanate from each of the corners of the indent but do not pass underneath the indent); 2) half-penny cracks (radial-median cracks: similar to Palmqvist cracks but emanating from the under the center of the indent from one indent corner to another on the same diagonal – usually formed at higher loads than Palmqvist cracks [121]; and 3) lateral cracks (cracks that form on the sides of the indent and intersect the surface between the corner cracks). Depending on the load, the bioglass was observed to display half-penny and lateral cracks, although, from simple visual inspection, it was very difficult to distinguish Palmqvist from half-penny cracks. After immersion in PBS (and dissolution of the indented area), the cracks emanating from the corners of the indents appeared to be half-penny cracks exclusively.

SEM micrographs of as indented bioactive glass (prior to any immersion in PBS) are shown in Figure 3.1. Sharp cracks emanating from the indent corners were observed for all loads reported herein (loads <30mN had no noticeable cracks as observed in the optical microscope). The indent diagonal length, $d = 2a$, and crack length, $2c$, where a and c are marked on Figure 3.1 for an as indented specimen. The hardness, crack length, fracture toughness, crack ratio (crack length/half indent diagonal; c/a), and residual energy were quantified as a function of maximum indentation load prior to immersion in PBS.

Hardness

Hardness, H, was calculated from the average indent diagonal length, $\bar{d}$, according to the well known relation for a Vickers indenter:

$$H = \frac{1.854 \cdot P}{\bar{d}^2} \quad (3.1)$$

where P was the maximum indentation load. The hardness as a function of maximum indentation load is shown in Figure 3.2a, wherein hardness appears to be independent of indentation load, although there is considerable scatter in the data.

Crack Length

The main purpose of measuring crack lengths from Vickers indentations in brittle materials is ultimately to gather data concerning their fracture toughness. The fracture mechanics of a Vickers indent are complicated, as is the stress field surrounding the indent. The main basis of the technique concerns the crack shape; cracks are assumed to be radial-median cracks below the indent, with a center point force leading to crack opening [122, 123]. Satisfying these conditions leads to a specific stable equilibrium relation between the applied load, P, and the crack radius, c:

$$P = kc^{3/2}$$

(3.2)

where k is a constant of proportionality. The maximum indentation load as a function of crack length, Figure 3.2b, shows good correlation with the stable equilibrium relation 3.2. The value of k from the linear curve fit (forced through zero) was 8.651. It can be seen that for small loads the crack size is effectively smaller than the predicted relation. For such small loads, the associated measurement error in the magnitude of the crack length could certainly explain deviation from Equation 3.2.

Fracture Toughness

For an elastic-plastic indent, the residual stress surrounding the indent following load and unload leaves a residual stress-intensity relating to the crack size that can be characterized by [121]:

$$K_R = \frac{\chi P}{c^{3/2}} \quad (P > P_C,\ c >> a)$$

(3.3)

where K_R is the residual stress-intensity of the radial-median crack in an ideal case, χ is a dimensionless constant, and P_C is the critical contact load. The residual stress-intensity becomes the critical stress-intensity factor, K_C, (toughness in vacuum, T_o) when $c = c_I$ (the pop-in crack length).

For applicability of indenters used in ceramic systems, the calculation of fracture toughness using the classical relations 3.2 and 3.3 has been evaluated to determine the constant of proportionality, χ (in eq. 3.3) from a mechanics analysis of the point load caused by the Vickers indenter tip [124]. The result of such analysis led to the following, now widely accepted, relation for determining the mode one fracture toughness, K_{IC}, from measurements of indenter induced radial median cracks:

$$K_{IC} = \delta \left(\frac{E}{H} \right)^{1/2} \left(\frac{P}{c^{3/2}} \right)$$

(3.4)

where E is the Young's modulus of elasticity, H is the hardness, and δ is non-dimensional indenter-geometry constant (established to be 0.016±0.004 for radial-median cracks caused by a Vickers indenter [125]).

Of interest to the bioglass tested herein, where difficulty exists in determining the nature of the cracks as viewed from the surface, it has been shown [126] that despite the nature of cracks caused by a Vickers indenter in a glass-ceramic (either Palmqvist or radial-median) the estimation of fracture toughness more accurately follows bulk values if a radial-median crack geometry is assumed using Equation 3.4. Thus our analysis employed Equation 3.4. Figure 3.2c shows the fracture toughness of the bioglass as a function of indentation load. The elastic modulus of the bioglass was reported by the manufacturer to be 30-35 GPa as determined by ASTM standard C623-71 [127] and an average value of 32.5 GPa was used in the calculations. The fracture toughness is observed to decrease with increasing load reaching a minimum value of 0.23 ± 0.07 MPa $m^{1/2}$ for $P_{max} \geq$ 350mN. Measurement error in the small crack lengths at small load could explain the decreasing toughness with increasing load.

Crack Ratio

The ratio of the crack length to indent size was characterized to determine any

effects of load dependence on the toughness. Figure 3.3a shows the magnitude of the crack size, c (half the total length from crack tip to crack tip) and the indent size, a (half the length of the indent diagonal from corner to corner) as a function of maximum indent load. The change in the ration between the crack size and the indent size is plotted in Figure 3.3b, where the ratio c/a is observed to change as a function of indentation load above ~90mN, then approach a steady state value of c/a = 2.8.

3.3.2 Residual Energy

The amount of energy being transferred from the indenter to the sample during an indentation test is approximately to be the integration of the force displacement curve. Dissipation of that supplied energy can take various forms: elastic, plastic, or anelastic deformation; reduction in specific volume through densification and crystallization; creep; or even production of heat. Indented regions may also contain residual mechanically induced elastic strain energy. The return of elastic strain energy is prohibited due to local geometrical changes, such as permanent deformation, or crack surfaces binding upon each other [121] and thus remains in the indent region to elicit compressive and or tensile stresses.

The residual stresses remaining after indentation have been analyzed in great detail [121, 122] and Bowden and Gardiner [128] imaged the residual stress distribution surrounding a Vickers indent in single crystal silicon in a quantitative manner by measuring Raman shift, as has been observed for birefringent glasses in polarized light studies. Residual tensile stress occurs at the crack tips, and a compression stress field emanates from the indent outward in the shape of a 4-leaf clover.

Determining the amount of anelastic energy lost, or stored in the material, during the indentation cycle gives insight to the possible stress and strain fields that linger after all indentation loads have been removed, and furthers our aim in understanding the interaction between strain energy and dissolution/bioactivity. Force-displacement

curves (P-δ) were numerically integrated to determine the anelastic energy of the indents (the shape of the curves required integration with respect the displacement axis). Figure 3.4a is a typical P-δ curve indicating the areas associated with the elastic energy, and anelastic energy (consumed and stored energy in the material), with the total energy being the sum of the two regions. Based on the smoothness of the loading and unloading curves, it was surmised that the loading rate was faster than that required to observe pop-in of half-penny cracks during indentation.

The anelastic energy is plotted against the maximum indentation load in Figure 3.4b. The data were curve-fitted with a power-law to determine the exponential dependence on the load. The slope change in the curve fit data (from 0.3 over the range $30<P_{max}<70$mN to 2.5 for $P_{max}>70$mN) could indicate that a threshold load exists, above which a much higher degree of energy is dissipated due to a microstructural mechanism rather than elastic energy return. Potential mechanisms for such a drastic change could be localized densification of the glass or more extensive cracking, such as formation of lateral cracks during unloading. A load limit may exist before densification of the glass occurs due to indentation forces (i.e., an activation energy must be overcome). Nanocrystallites have been discovered beneath indents in bulk metallic glass at room temperature [129], presumably nucleated and grown during indentation due to the energy obtained through heating of deformation [129].

In other materials systems, both brittle and ductile, the slope of the anelastic (plastic) energy is a constant over various indentation loads. For instance, in zirconium-based bulk metallic glass the anelastic energy exponent is 1.5 [130] for loads higher than those reported here. In ductile metals such as Sn3.5Ag, the exponent is 1.6 [131] for equivalent loads. The measure of the tendency of a glass to devitrify underneath the indented region should be related to the bond energies of the species that nucleate to form crystallites (likely the species with the smallest bond energies: Ca-O and Na-O bonds rather than Si-O or P-O bonds [132]). In the case of bioglass, the crystallization kinetics determined by Clupper and Hench [132] revealed

that the activation energy for devitrification of bioglass 45S5 was 350 kJ/mol. The mechanical interaction of the indenter tip with the specimen surface could then be thought of as supplying the driving force for the devitrification process when mechanical energy is converted to heat, or results in compression of bonds such that they are close enough to then achieve a minimum in bond energy by densifying the structure.

3.3.3 Dissolution and Bioactivity

Figure 3.5 shows a selection of indents after various times of immersion in PBS, and several observations can be made from the figure. Dissolution nucleates seemingly randomly on the bioglass surface. Regions undergoing dissolution appear to grow by spreading laterally over time and do not appreciably deepen. The region surrounding the indents may or may not dissolve at the same rate as the bulk bioglass depending on the maximum indentation load. Indentation crack tips blunt due to local dissolution within 1 day of immersion along with the damaged center region of the indent. Small indents (maximum load $\leq$ 100mN) are seen to be consumed by the lateral spreading of the dissolution more rapidly than larger indents (maximum load $\geq$ 100mN); indents made with a load $\geq$ 200mN are surrounded by undissolved bioglass, for up to 9 days.

Upon closer examination of the indents, Figure 3.6 shows that the intact region surrounding indents is actually being dissolved (P_{max} = 500mN, 9 days in PBS). The intact, smoother region is being dissolved at a much slower rate than indented surface, resulting in a different appearance. Presumably, the ultimate morphology of the slowly dissolving region would be similar to that on the bulk surface given enough time, which is indeed the case. Undercutting of the compressed region of the indent between the cracks was also observed, seemingly along subsurface lateral crack interfaces. As such, an indication of the three dimensional structure of the subsurface strain field can be gleaned from Figure 3.6a,b,c, and indicates that the

dissolution of regions surrounding indents is complex.

It is possible that the residual elastic compressive strain present surrounding indents with sufficient anelastic energy storage was slowly undermined by undercutting of the indented region along the transition zone between the residual field and the stress free bulk, in which case, the previously compressed region would have relaxed and then had a lower free energy to allow for dissolution, resulting in the dimpled appearance of the "compressed zone" in Figure 3.6.

In addition, small precipitates are observed as spheres where the bioglass has been dissolved (Figure 3.6b), but their chemistry was not quantified due to their small size and large interaction volume of the energy dispersive analysis probe in the SEM. The small precipitates were not found on the surface on the indent within the perimeter of the transition zone between the bulk surface and the indent.

The difference in dissolution rate between regions around the indent and far from the indent can be explained by two possible mechanisms: 1) the indented region is under compressive strain, and or 2) the indented region has been devitrified and somewhat crystallized. A striking correlation between calculated residual strain/stress fields and the undissolved region surrounding the indents is found when comparing the work of Bowden and Gardiner [128] to the SEM images of the indented and *in vitro* tested specimens. A schematic of the strain field is reproduced in Figure 3.6b where light regions are highest compression and the darkest regions (at the crack tips) are in tension.

Compressive stress has been reported to reduce dissolution rates of hydroxyapatite coatings [133, 134], and high degrees of crystallinity in bioglass (>60%) have been reported to result in increased time to HCA layer formation, that can be surmised to be due to a decrease in dissolution rates [135]. A complication of the interpretation of the effect of crystallinity is that many additional variables affect the dissolution rate, such as: 1) the connectivity of the residual glassy phase, which affects the net flux of ions going into solution and formation of silanol bonds; 2) the pH; 3) the rate at which ions exchange; the hydroxylation of the surface; and the concentration of ions in solution [135].

The dissolution of a material in an environment to achieve equilibrium depends on three driving forces: 1) reduction of the net chemical potential to zero, 2) reduction of stored strain energy, and 3) reduction of surface free energy. The treatment of Sergo *et al*. [133] concerning the interaction between chemical and mechanical driving forces for thermodynamic equilibrium are not reproduced here, but are summarized in two expressions:

$$\Delta G^o - \frac{\sigma_{kk}}{3}\Omega = -RT \ln \frac{K_{PS}^{\sigma}}{K_{PS}} \qquad (3.5$$

while setting the free energy change, ΔG^o, to zero for equilibrium conditions it is found:

$$\frac{\sigma_{kk}}{3}\Omega = RT \ln \frac{K_{PS}^{\sigma}}{K_{PS}}$$

(3.6)

where σ_{KK} is the trace of the stress tensor, Ω is the molar volume of the material, and K_{PS}^{σ} and K_{PS} are the solubility products of the stressed material and unstressed material respectively. It can be seen from Equation 3.5 that a compressive stress (-) increases the free energy and thus would prohibit dissolution, whereas tensile stresses (+) aids to decrease the free energy and thus promotes dissolution. Equation 3.6 demonstrates that if the stress state were well characterized and the system was in equilibrium, the solubility product under stress could be calculated.

The solubility products for bioglass are complicated, as many reactions are occurring simultaneously, making it difficult to calculate the change of the solubility product as a function of stress. It remains unclear if regions that had been indented sufficiently to slow down dissolution ($P_{\max}$ > 200mN) had a short-or long-term effect on bioactivity, since after three weeks the indentations could not be clearly identified with absolute certainty. Also under question is the critical load required to see a difference in apparent dissolution. It seems likely that even though the thermodynamics require a compressively stressed region to dissolve less slowly, the

driving force would be necessarily small for small degrees of residual strain; thus, for small loads, a minimal effect was observed and was governed by kinetics.

After two weeks immersion, Figures 3.7a and b show remnants of former indent locations (white arrows) based on the structure of the newly forming mineralized layer of what is likely hydroxyapaptite (Ca/P ratio of 1.71 by EDS) with some needles, likely dicalcium phosphate as seen in Figure 3.7c (Ca/P ratio of 1.1 to 1.2 by EDS). Without *in vivo* testing, there is no certain way to predict if indented regions would change the local bioactivity from Class A to Class B, thereby only permitting extracellular response, since mineral deposition seems to proceed, albeit in a different morphology around indents for up to two weeks.

3.3.4 Materials Characterization

XRD confirmed that the bioglass 45S5 rod obtained from MO-SCI Corporation was amorphous, and when the bioglass was measured again after 3 weeks immersion in PBS no significant differences were observed, Figure 3.8. Intensity variations seen in Figure 3.8 show that there is a broad amorphous peak in each condition centered at ~ 32° (note: the scans are from different representative samples). Crystallites (as seen in the SEM) were not detected by XRD, because there was not enough volume present to result in significant diffraction intensity over the background.

3.4 Summary

The effect of a micro-indentation load on the dissolution of bioactive glass 45S5 was revealed that compressive strain fields inhibit dissolution. A critical indentation load (~200mN) was required to impart sufficient residual energy into the glass before an appreciable effect was observed for *in vitro* dissolution testing. This critical load also seems to coincide with the first appearance of lateral cracking. The morphology of the surface in the area surrounding micro-indents in bioglass 45S5

was found to have a markedly different appearance than that of the surface away from the indent after immersion in PBS. Dissolution within an area circumscribed by a radius approximately equal to the radial-median crack length, *c*, was observed to be much slower than the surface away from the indent, presumably due residual compressive strain. On the contrary, the crack tips, regions known to have an associated tensile strain [128], dissolved much more rapidly than the bulk surface causing the crack tips to blunt within 1 day of immersion in PSB. The indented region under compression did not appear to start dissolving until after 1 week in PBS, likely due to strain relaxation due to undercutting of the indented region.

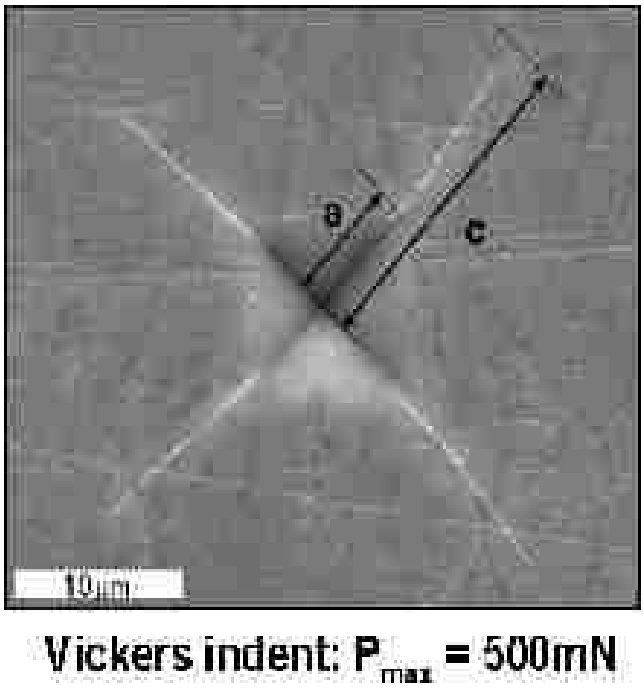

Figure 3.1. Secondary electron micrograph of as-indented bioactive glass. 500mN maximum load. a, c, denote the half indent diagonal and half crack lengths respectively. Marker bar is 10μm.

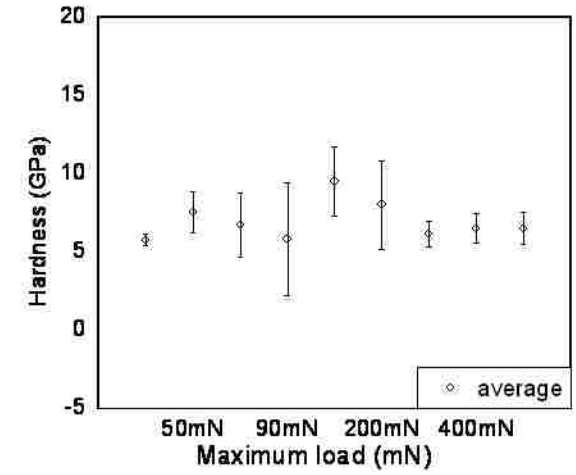

a)

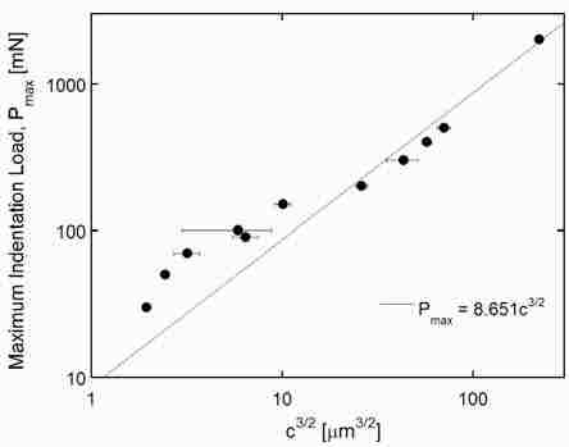

b)

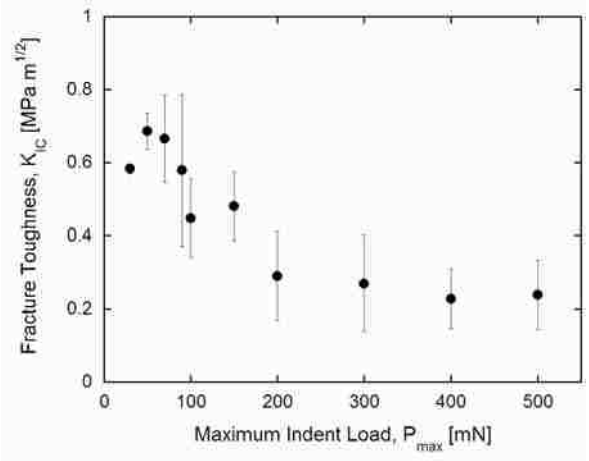

c)

Figure 3.2. a) Hardness as a function of maximum load. b) Maximum load as a function of crack length to the 3/2 power. c) Critical stress intensity factor (indentation fracture toughness) as a function of maximum load. Average of 5 indents for each load + one standard deviation

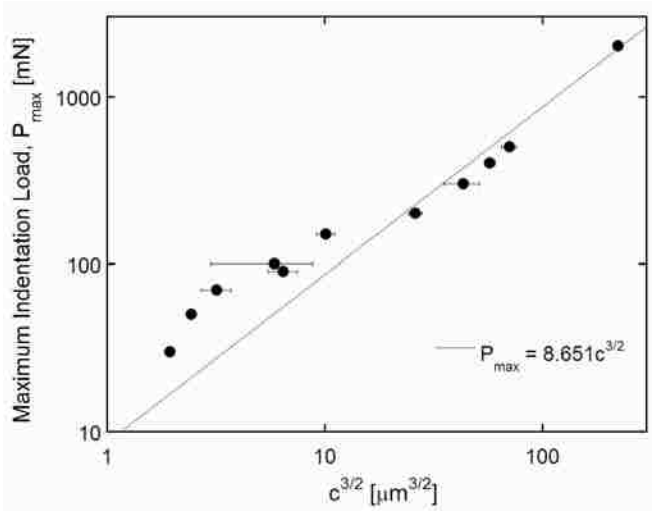

a)

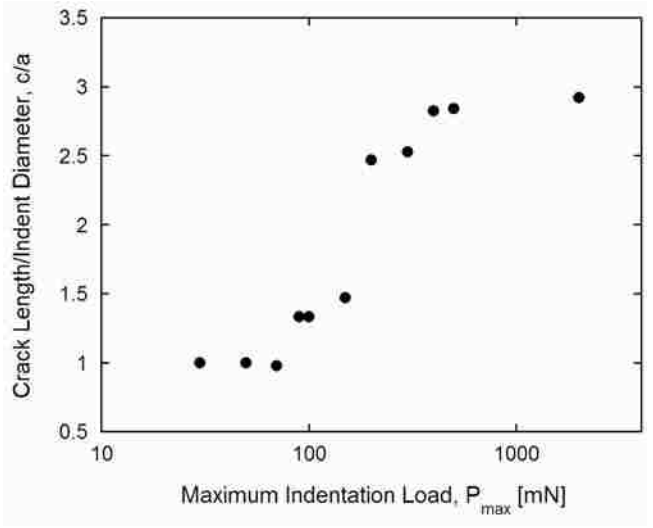

b)

Figure 3.3. a) a, c, as a function of maximum load. b) ratio of crack length to indent diameter, c/a, as a function of maximum load. Average of 5 indents for each load + one standard deviation.

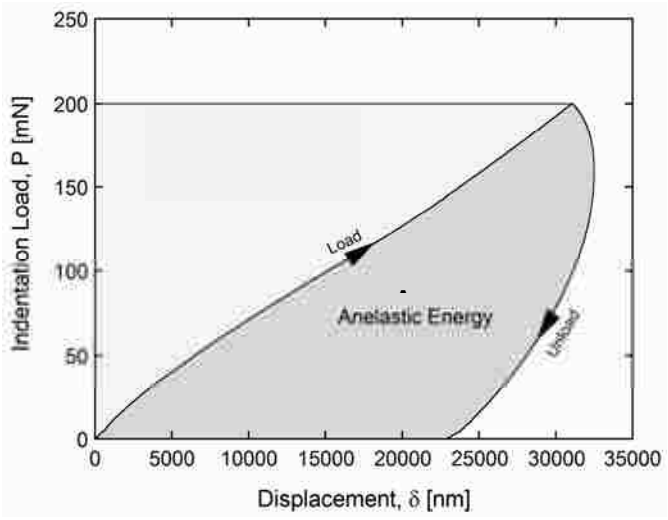

a)

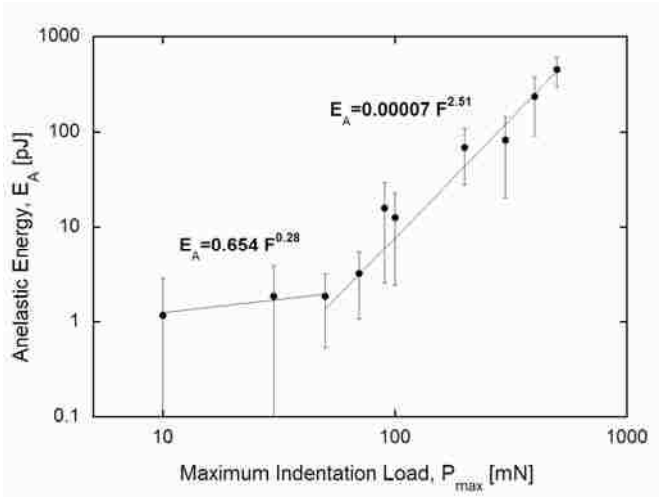

b)

Figure 3.4. a) Schematic diagram superimposed on a typical load-displacement curve for 200mN maximum load; EA and EE denote the anelastic and elastic energy of the indentation process. b) Aneslastic energy as a function of maximum indentation load. Power-law curve fits show fitting parameters. Average of 5 indents for each load + one standard deviation.

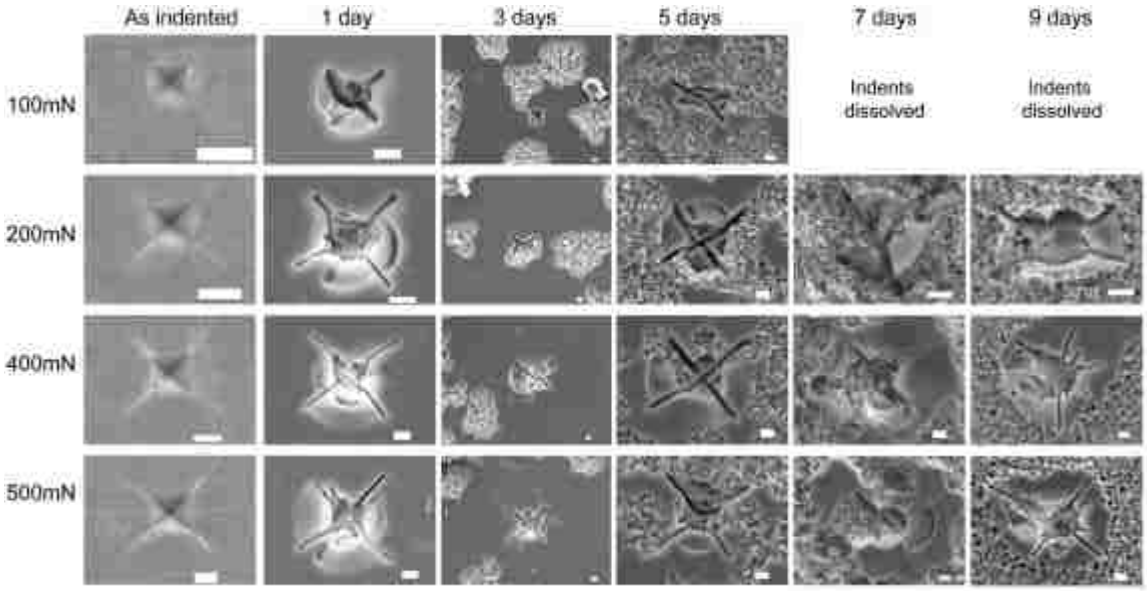

Figure 3.5. Selection of secondary electron micrographs of indented and indented and immersed specimens for various maximum loads and immersion times. All marker bars are 5μm. Surfaces after 3 days immersion are shown at lower magnification to demonstrate the random nucleation and growth of dissolved regions and precipitation of minerals. It can be seen from the images that sufficiently high indentation loads limit the dissolution of bioactive glass surrounding the indents, even after 9 days immersion.

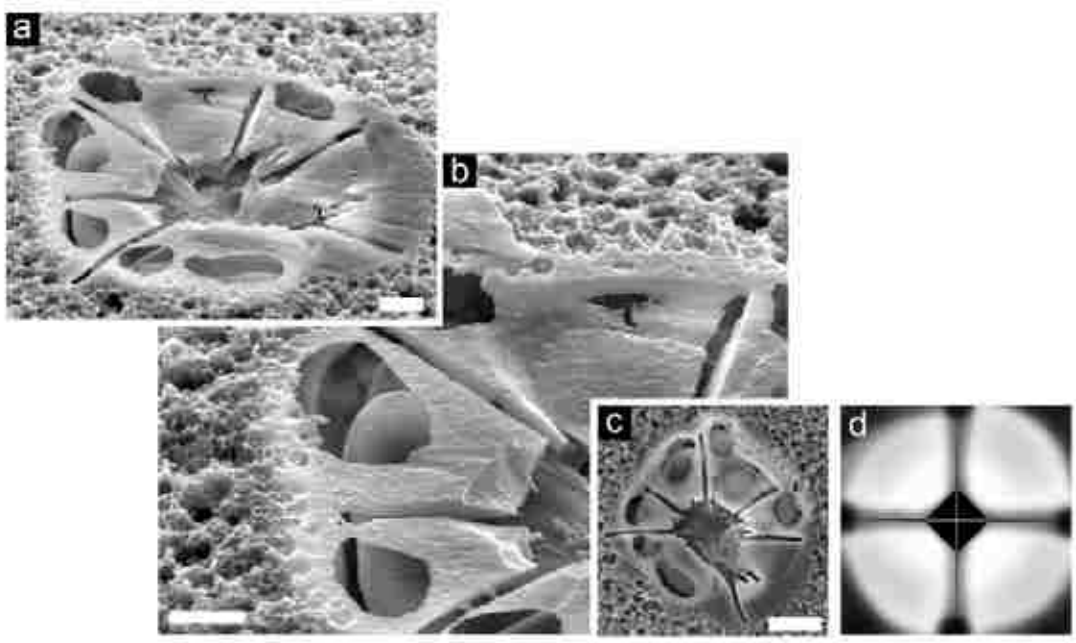

Figure 3.6. a) Secondary electron micrograph of 500mN indent after 9 days immersion in PBS; 30° tilt, marker bar is 5μm. b) zoomed region of a) showing undercutting and precipitation of minerals on the surface; marker bar is 5μm. c) Plan view of same indent showing the extent of the undissolved region surrounding the indent, approximately about a radius equal to the crack length circumscribed around the indent; marker bar is 20μm. d) Schematic diagram of the stress field surrounding an indent as imaged with photoelastic methods, or raman spectroscopy. Whiter regions are higher compression and the darkest regions are tension (at crack tips). The surface of the indent and cracks are black to show no information gathering due to scattering.

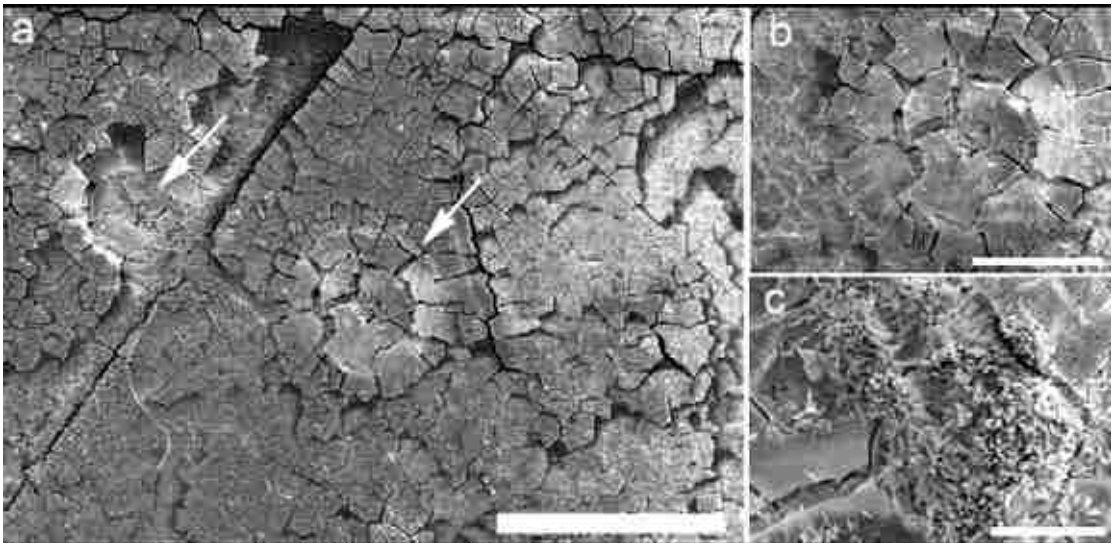

Figure 3.7. Secondary electron micrographs of a) indented sample surface after 2 weeks immersion in PBS; marker bar 500μm, white arrows indicate indent locations. b) higher magnification of a); marker bar is 200μm. c) sample surface after 2 weeks immersion in PBS far away from indentations, where mineral phases precipitated on surface; marker bar is 50μm.

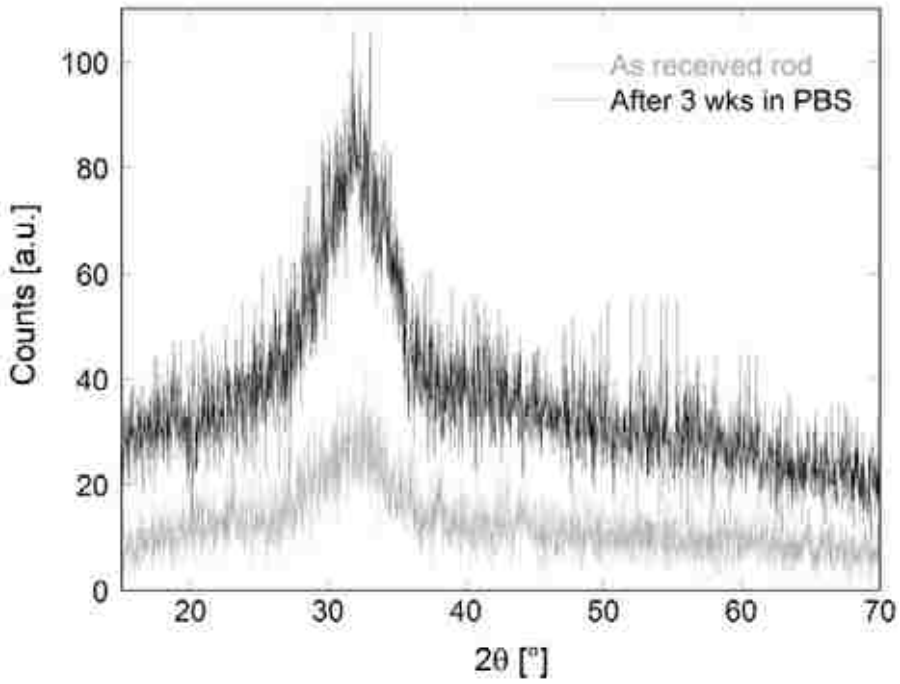

Figure 3.8. XRD spectra from as received bioactive glass and that immersed for 3 weeks in PBS, clearly showing that no mass crystallization has occurred of the glass, nor the surface. Although the presence of minerals phases is apparent in Figure 7, they are not measured by XRD.

Chapter 4 Indentation-induced residual stresses in 45S5 bioglass and the stress effect on the material dissolution

4.1. Background

Concerns about the bioactivity of bioactive glasses under mechanical stresses and the stress-assisted reaction have stimulated an interest in understanding the evolution of local stresses and their effect on local material dissolution. We studied the development of local mechanical stresses and the stress effect on the material dissolution at the crack tip in 45S5 bioactive glass, using the microindentation technique. The indentation test is a technique to characterize localized mechanical behavior of materials. The advantages of using the indentation test involve the use of small amount of materials and the creation of local elastoplastic deformation of materials for measuring the dependence of the surface evolution on the indentation load, local deformation, and material properties. The local stress created by indentation is characterized by the method of the indentation fracture around the indentation imprints. The stress-assisted dissolution of 45S5 bioactive glass at the crack tip is investigated in phosphate buffer solution, and the dependence of the dissolution rate (the crack propagation speed) is correlated with the indentation load.

4.2. Experimental

Sample preparation

Cast and annealed rods (10mm in diameter) of 45S5 bioactive glass (45wt%SiO_2, 24.5wt% Na_2O, 24.5wt% CaO, 6wt% P_2O_5) were received from MO-SCI Specialty Products, L.L.C. (Rolla, MO, 65402). Sample sectioning and surface preparation were carried out in accordance with the procedure given in the previous chapter to produce polished 3mm thick discs. Following the surface preparation, the discs then annealed in air at 350^{o}C for 2 hours and furnace-cooled to room temperature to

remove the residual stresses generated from grinding and polishing.

Microindentation

Microindentations were made on the polished discs using a diamond Vickers indenter on a Micro-Combi Tester (CSM Instruments, Needham, MA). The indentation loading-unloading rate was fixed at 200mN/min with a hold time of 5 second at the peak load. A minimum of 5 indents were made per load. The indentation imprints were measured using optical microscope (OM) and scanning electron microscopy (SEM). Large indents (primary indents) were created using the indentation load in the range of 200 to 500 mN to an array of indentations. The distance between the large indents was at least 3 times that of the indentation size. Radial cracks were formed along the corners of the indentations due to stress concentration. An array of small indents (secondary indents) in each quadrant was made along the direction of 45º to the diagonal of the large indents. The indentation load varied from 30 to 90 mN. Figure 4.1 shows a set of typical indentations on the surface of a 45S5 bioactive glass. Radial cracks were also observed for the indentations by small indentation loads. The loading-unloading curves were recorded; and SEM was used to measure the indentation size and the crack length. The samples were stored in a desiccator following the indention before the *in vitro* dissolution testing as well as between the *in vitro* testing and the SEM measurement.

***In vitro* dissolution testing**

The indented discs with the indented surface up were placed in a PBS of ~ 1L in an agitated water bath at a uniform temperature of 37 °C. The PBS used was made from 5mL of magnesium chloride solution (3.8g $MgCl_2$ in 100mL of de-ionized water (DI-H_2O)) and 1.25mL of potassium dihydrogen phosphate solution (3.4g KH_2PO_4 in 50mL DIUF-H_2O, diluted with 50mL DI-H_2O to make 100mL, with trace 1N sodium hydroxide to maintain pH of 7.2) added to 1L DI-H_2O. The PBS was not agitated itself and was sealed to prevent contamination and evaporation. The specimens were immersed into the PBS for 1, 3, 5, or 9 days.

Materials characterization

SEM with energy dispersive x-ray capability (EDS) was performed to characterize the morphology of the indentation imprints on a Hitachi S3200 instrument. The indented and dissolved bioactive glass discs were gold-palladium-coated prior to SEM. The samples were stored in a desiccator between the characterization study.

4.3. Results and Discussion

4.3.1 Indentation hardness

Figure 4.2 shows the SEM micrograph of the primary indent made at the peak indentation load of 400mN. Radial cracks emanated from the corners of the indent due to the stress concentration from the contact between the Vickers indenter and the bioactive glass. The indentation-induced cracks were observed for all the indentations made in the experimental conditions. The diagonal length of the indent was $d = 2a$, and the length of the radial crack $2c$, as shown in Fig. 4.2. The indentation size, hardness, crack length, fracture toughness, and residual stresses were quantified as a function of maximum indentation load prior to the immersion in the PBS.

The Vickers hardness, H, was calculated using the average diagonal length, $\bar{d}$, of the indent as

$$H = \frac{1.854 \cdot P}{\bar{d}^2} \quad (4.1)$$

where P is the peak indentation load. Figure 4.3 shows the dependence of the indentation hardness on the indentation load. The indentation hardness appears to be independent of the indentation load for the experimental conditions with the average indentation hardness of 7.47±0.51 GPa, comparable to 7.18 GPa for the unannealed

45S5 bioactive glass shown in the last chapter. The difference could be due to the residual stresses in the unannealed bioactive glass.

4.3.2 Indentation-induced cracks in the stress-free bioactive glass

For the indentation of a stress-free glass by the Vickers indenter, the length of a radial crack induced by the indentation is a function of the indentation load, which can expressed as [136]

$$P = \frac{K_{IC}}{\delta}\left(\frac{E}{H}\right)^{-1/2} c^{3/2}$$

(4.2)

where K_{IC} is the fracture toughness, δ is an empirical constant of 0.016 ± 0.004 for the Vickers indentation[137], and E is Young's modulus of the material. Figure 4.4 shows the dependence of the crack length on the indentation load for the primary indents, corresponding to the indentations of the bioactive glass at the stress-free state. The indentation load is proportional to the $c^{3/2}$ for the indentation loads larger than 200 mN, following Eq.(4.2). For the indentations with the peak indentation load of 100 mN, the crack length is larger than the predicted value from the relation. This is likely due to the subsurface damage induced during the grinding and polishing, which caused the bioactive glass to have less resistance to the propagation of the indentation-induced cracks. At small indentation loads, there is significant contribution from the subsurface damage to the formation and propagation of surface cracks, and the contribution of the subsurface damage becomes less and less important for the indentations of large loads. The Young's modulus of the 45S5 bioactive glass was reported by the manufacturer to be 30-35 GPa as determined by ASTM standard C623-71. Using an average value of 32.5 GPa in Eq. (4.2), we obtained the fracture toughness of 0.11±0.02 MPa·m$^{1/2}$ – two times less than the fracture toughness of the unannealed bioactive glass shown in Chapter 3.

4.3.3 Indentation-induced cracks around the primary indents

The secondary indentations were made around the primary indents as shown in Fig. 4.1. Figure 4.5 shows the variation of the crack length of the secondary indentations with the distance to the primary indent made at the indentation load of 500 mN for various indentation loads. As expected, larger indentation loads led to larger crack lengths. For the same indentation load, the crack length increased with increasing distance away from the center of the primary indent. This trend suggests that the local residual stress created by the primary indentation is compressive, which decreases with the distance away from the center of the primary intent.

It is known that an indentation causes localized deformation and creates residual stress surrounding the indent. Equation (4.2) does not take account of the effect of residual stresses and becomes inapplicable to the analysis of the indentation-induced cracks formed by the secondary indentations due to the development of local residual stresses around the primary indents. The residual stress around an indentation is complex. It depends on the material properties and the indentation load. Several models have been developed to use the method of the indentation fracture to measure the residual stresses around an indent. The effect of the residual stress on the crack propagation in an indentation was considered in detail. The resultant stress intensity factor is a linear function of the residual stress and is dependent of the crack length. For a residual stress acting over a portion of crack surfaces, the resultant stress intensity factor is a linear function of the square root of the crack length[138], and, for a residual stress acting over a line segment of the crack surface (i.e., the residual stress is described by a line residual force), it is a linear function of the reciprocal of the square root of the crack length[139].

Under the action of a uniform residual stress of σ_R, the resultant stress intensity factor, K, for the crack growth in an indentation can be expressed as[138]

$$K = \delta \left(\frac{E}{H} \right)^{1/2} \frac{P}{c^{3/2}} + \sigma_R \sqrt{\alpha \pi c}$$

(4.3)

where α is a crack-geometry factor. When the material is subjected to compressive residual stress ($\sigma_R < 0$), the residual stress causes the closure of the crack and the reduction of the resultant stress intensity factor. Under tensile residual stress ($\sigma_R > 0$), the tensile stress assists the crack propagation and increases the stress intensity factor. For indentations by a Vickers indenter, the equilibrium condition for the crack growth yields[140]

$$K_{IC} = \delta \left(\frac{E}{H} \right)^{1/2} \frac{P}{c^{3/2}} + \frac{2\tilde{\sigma}_R}{\sqrt{\pi}} \sqrt{c}$$

(4.4)

which gives

$$P = \frac{c^{3/2}}{\delta} \left(\frac{E}{H} \right)^{-1/2} \left(K_{IC} - \frac{2\tilde{\sigma}_R}{\sqrt{\pi}} \sqrt{c} \right)$$

(4.5)

Here $\tilde{\sigma}_R$ is the local average residual stress around the indent. It is worth pointing out that Eq. (4.5) is based on the assumption that there exists a spatial distribution of residual stresses surrounding the crack. This is different from the approach used by Zhang et al. [139], who used a line residual force in their analysis.

Figure 6 shows the dependence of the crack length of the secondary indentations on the indentation load. For comparison, Eq. (4.5) is used to fit the experimental results with the indentation hardness of 7.47 GPa and the fracture toughness of 0.11 MPa·m$^{1/2}$ obtained in previous sections. The fitting curves are also depicted in Fig. 4.6. Clearly, Eq. (4.5) describes the relationship between the crack length and the indentation load of the secondary indentations in the stress field created by the primary indentations. It is worth mentioning that the residual stress field measured is a local average stress including the contribution of the primary indentation and the other secondary indentations since the space between the secondary indentations was

not larger than 3 times that of the indentation size. In addition, the field of the residual stress around an indent has radial and transverse components. It would be almost impossible to measure the individual stress component from the indentation test, even though a smaller indenter size such as those in nanoindentation can be used.

Figure 4.7 shows the variation of the local average residual stress around the primary indent. The primary indentation produced large compressive stress near the indent, which decreases with the increase in the distance from the center and approaches the stress-free state. It is known that the radial component of the residual stress created by the indentation is compressive and the transverse component is tensile[141]. This result suggests that the local average stress reflects more characteristics of the radial component of the local residual stress along the direction of 45º to the diagonal of the indentation.

The dependence of the average local residual stress on the indentation load for the primary indentations is depicted in Fig. 4.8 for the secondary indentations at the location of 5 μm to the center of the primary indent. The average local residual stress is compressive with the magnitude increasing with the increase in the indentation load for the primary indentations. The higher the indentation load, the larger the average local residual stress is at equivalent locations. This result is consistent with the observation of larger indents under larger indentation loads. It should be mentioned that there is little effect of the interplay between the primary indentation and the secondary indentations on the average local residual stress, since the secondary indentations at the distance of 5 μm to the primary indent were performed without the other secondary indentations nearby. These stresses represent the residual stresses created solely by the primary indentations.

4.3.4 Material dissolution

The dissolution behavior of the 45S5 bioactive glass around the indents was studied following primary indentations. The indented discs were immersed in a PBS solution at temperature of 37°C to mimic body temperature. Figure 4.9 shows the sequence of the surface evolution around the indents in the PBS solution over unannealed 45S5 bioactive glass.

Dissolution occurred first at the edges of the cracks and around/at the indents, as shown in Fig. 4.9b, without the presence of the dissolution in the other area, suggesting the stress-assisted reaction for the material dissolution. This preferential dissolution caused immediate blunting of the crack tips and widening of the cracks. The dissolution at the center of the indents was likely due to the local subsurface damage created in the indentation deformation. Following the material dissolution around the indents, material dissolved randomly over the surface as shown in Fig. 4.9c, and there was deep dissolution in the cracks and the center of the indents. After continuous exposure to the PBS solution for 9 days, the material dissolution reached the entire surface and created rough surface except the surface of the indents, which became much smoother than the surrounding surface. Undercutting dissolution of the ring-type was observed around the indents, indicating the formation of lateral crack consistent with the edge dissolution at the locations of A and B in Fig. 4.9b. Surrounding the indent, the surface became smooth. This is likely due to the average local compressive residual stress as measured in previous section, which reduced the dissolution and prevented further dissolution over the surface. This is in accord with the observation by Reis et al. [142] and Sergo et al. [46] that compressive stress reduced the dissolution rate of hydroxyapatite coatings, suggesting that local stress state plays an important role in controlling chemical reactions over the surface of solids.

Figure 4.10 shows the variation of the crack length with time for the cracks formed by the primary indentations. The crack length increases with the increase in the immersion time. The cracks created by larger indentation loads initially have higher growth rate. The growth rate gradually decreases with time due to less driving

force available for the cracks created by the indentation loads of 200, 300, and 400 mN. It should be pointed out that, after the fifth day, the indents created by the small indentation load of 100 mN were dissolved. This suggests that the average local compressive stress from the indentation could not prevent the dissolution of material, but only reduce the dissolution rate.

It is known that the crack growth can be described by the theory of thermal activation process. The atomic mobility, μ, at the crack tip is a function of the local residual stress in front of the crack tip and can be expressed as [143],[144]

$$\mu = \mu_0 \exp\left(\frac{-Q + \Omega\sigma_h}{RT}\right)$$

(4.6)

where μ_0 is an experimental constant, Q the activation energy for the rate process, Ω the activation volume, R the gas constant, T the absolute temperature. σ_h is the trace of the stress tensor, which is positive for tension stress and negative for compressive stress. For a dissolution process being controlled by atomic diffusion at the crack tip, the change in the crack length as a function of time can be expressed as

$$c - c_i = \alpha\sqrt{\mu t}$$

(4.7)

for a constant σ_h. Here, α is a constant and t is time. Assuming that σ_h can be approximated as a constant in front of the crack tip for the first 3 days and $\Omega\sigma_h << RT$, one obtains from Eqs. (4.6) and (4.7)

$$c - c_i = \alpha\sqrt{\mu_0 t}\exp\left(\frac{-Q}{2RT}\right)\left(1 + \frac{\Omega\sigma_h}{2RT}\right)$$

(4.8)

The increase in the crack length is proportional to the square root of the immersion time and is a linear function of the average local stress. In general, $\sigma_h \propto P$. Thus Eq. (4.8) can be written as

$$c - c_i = \alpha\sqrt{\mu_0 t}\exp\left(\frac{-Q}{2RT}\right)(1+\beta P)$$

(4.9)

where β is a geometrical constant, depending on the activation volume of the material and the surface profile of the indenter.

The experimental data in Fig. 10 was curve-fitted with Eq. (4.7) for the immersion time up to 3 days, obtaining the parameter of $(c-c_i)/\sqrt{t}$. The dependence of the parameter of $(c-c_i)/\sqrt{t}$ on the indentation load is depicted in Fig. 4.11. A linear relation between the parameter $(c-c_i)/\sqrt{t}$ and the indentation load is observed in good accord with Eq.(4.9), suggesting that the assumption of a constant σ_h is reasonable for the *in vitro* dissolution testing up to 3 days.

With the growth of the crack due to the material dissolution in the PBS solution, the material dissolution caused the motion of the crack surfaces and the blunting of the crack tip. Figure 4.12 shows the evolution of the crack-tip radius with the immersion time, in which the embedded micrograph shows the tip blunting and the lateral widening of a crack formed by an indentation load of 100 mN. The growth rate of the tip radius decreases with increasing immersion time, similar to the crack growth. In contrast to the growth of the crack length, the cracks formed by the indentation load of 100 mN have the highest growth rate in the blunting of the crack tip, while the cracks formed by the indentation load of 500 mN have the smallest growth rate for the tip blunting. This trend may be associated with the confinement of the surrounding material on the crack. For the indentations by small indentation loads, the plastic deformation zone is smaller and the compressive residual stress near the crack surface is lower. There is less resistance to the dissolution of material, which allows the presence of faster widening of the cracks and the faster blunting of the crack tips.

4.4. Summary

The mechanical response and the stress state in a bioactive glass determine the load-bearing applications and bioactivity of the bioactive glass. The residual stress developed in the handling and fabrication of bioactive glasses can influence the dissolution behavior and biofunction of bioactive glass as implant materials for bone replacement. Using the microindentation technique and indentation fracture, the local residual stress created in the 45S5 bioactive glass by indentation was studied around the indents along the direction of 45 º to the diagonal of the indents. The material around the indent was in a compressive stress state along the radial direction after the indentation. The average local residual stress increased with the increase in the indentation load, and the magnitude decreased with increasing distance away from the center of the indent. The compressive residual stress reduced the dissolution rate of the bioactive glass and retarded the dissolution of the indents formed by the primary indentations with the indentation load larger than 200 mN.

From the theory of thermal activation process, a simple relation was derived among the change of the crack length, the dissolution time, and the indentation load for the material dissolution in a short time period. The change in the crack length was proportional to the square root of the immersion time and was a linear function of the indentation load. The experimental results for the crack growth in the PBS solution supported this relationship. The lateral growth of the cracks was also observed. The blunting rate of the crack tip decreased with the immersion time, and the cracks generated by small indentation load had higher blunting rate than those created by high indentation load.

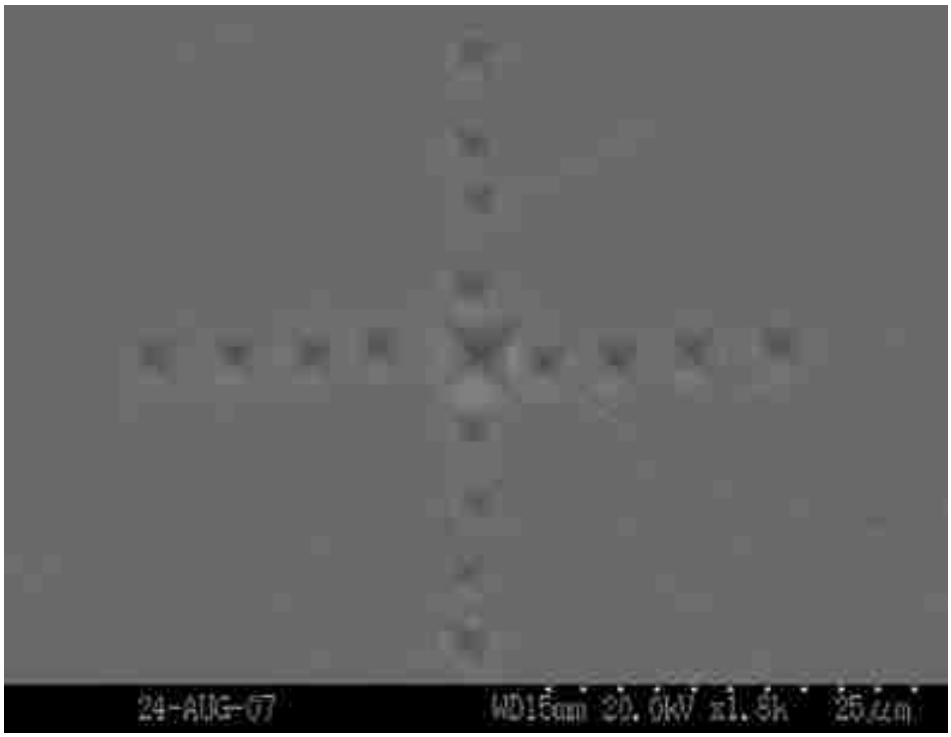

Figure 4.1. Secondary electron micrograph of a primary indent (F_{max}=200mN) and the secondary indents

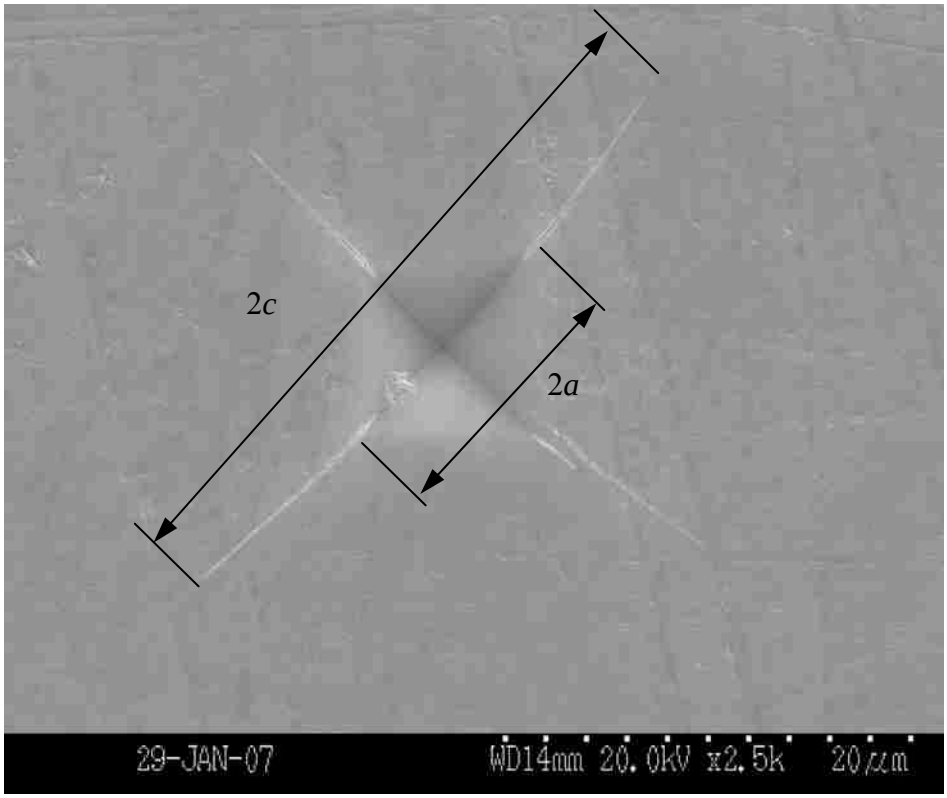

Figure 4.2. Secondary electron micrograph of the primary Vickers indent (with diagonal of length 2a) made at the peak indentation load of 400mN in the 45S5 bioactive glass, showing the formation of radial cracks of length 2c.

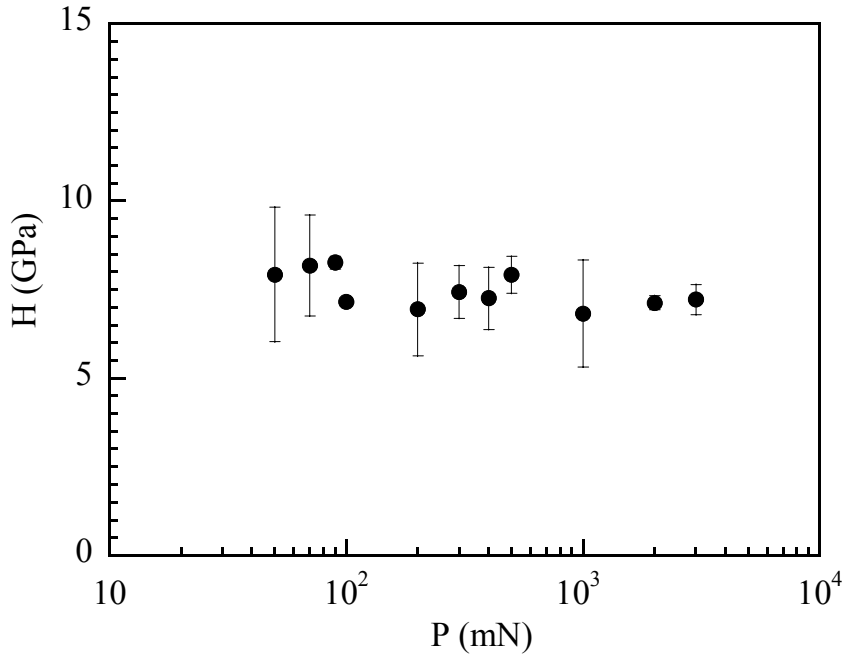

Figure 4.3. Dependence of the indentation hardness on the peak indentation load

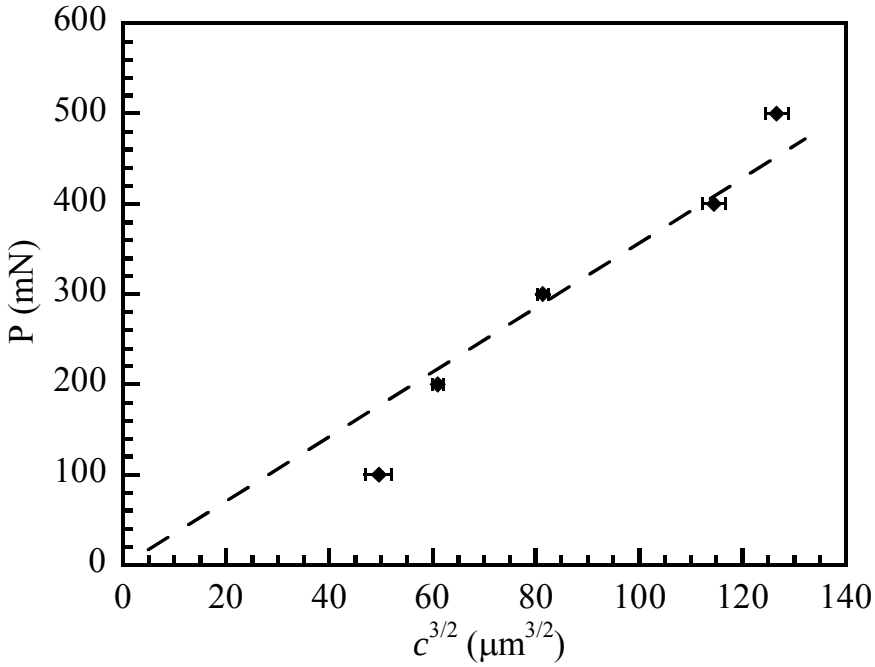

Figure 4.4. Dependence of the crack length on the indentation load for the indentations on the stress-free bioactive glass

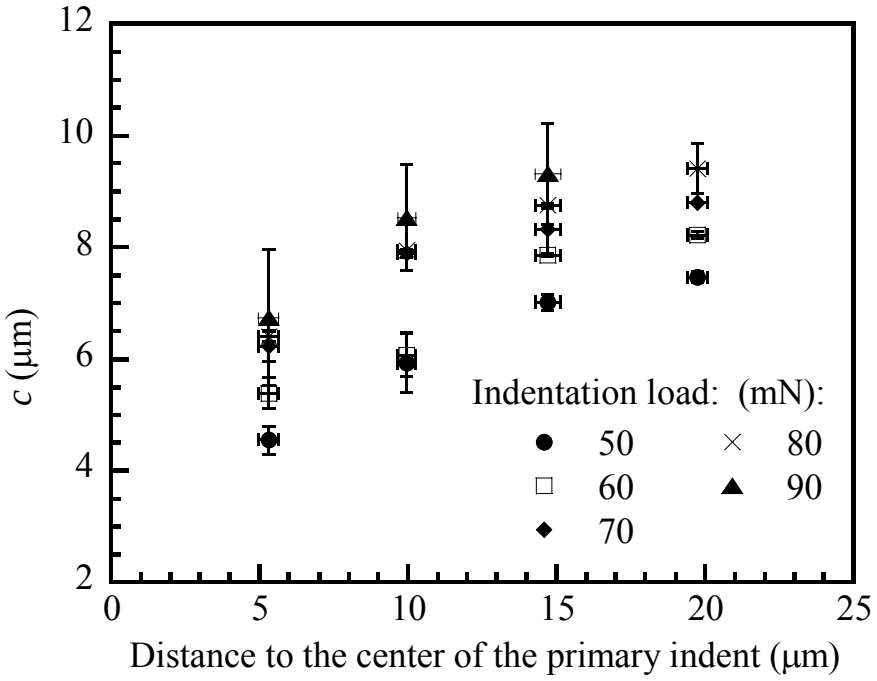

Figure 4.5. Variation of the crack size of the secondary indentations with the distance to the primary indent (indentation load for the primary indent: 500 mN)

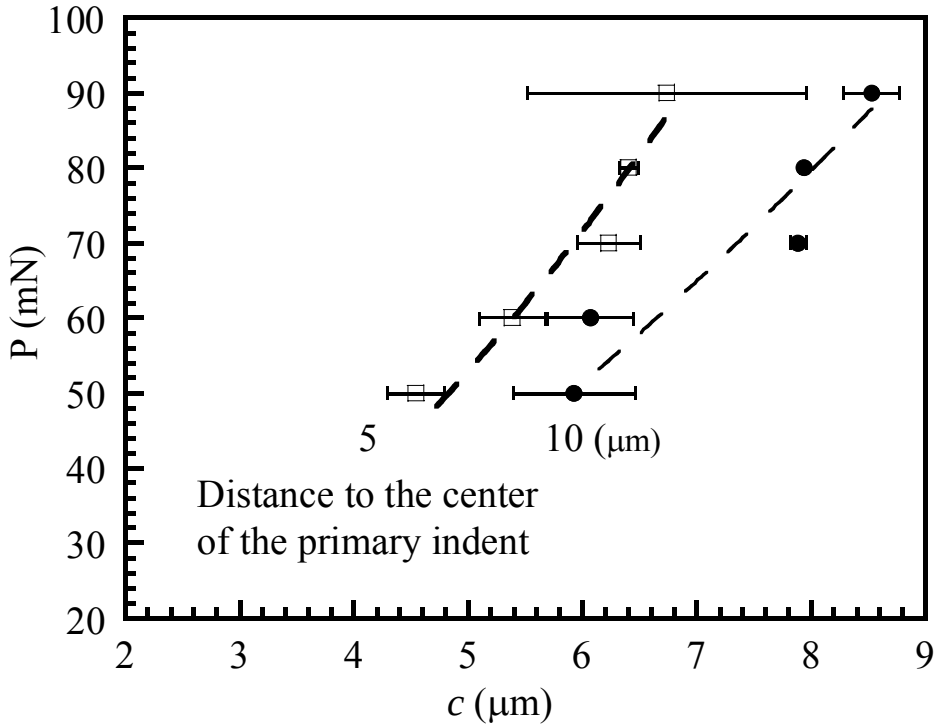

Figure 4.6. Dependence of the crack size of the secondary indentations on the indentation load (indentation load for the primary indent: 500 mN)

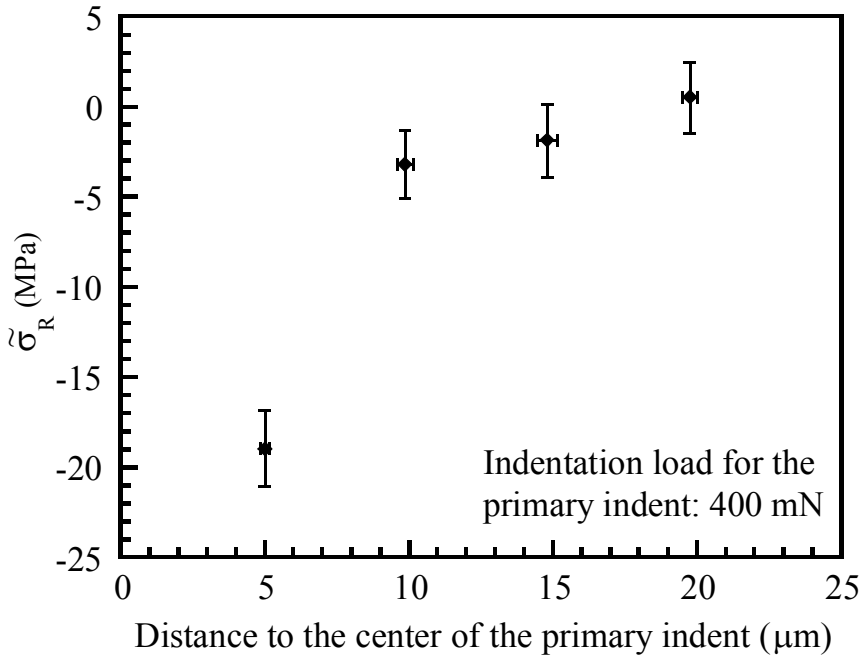

Figure 4.7. Variation of the average local residual stress with the distance to the primary indent (indentation load for the primary indent: 400 mN). Negative stress is compressive.

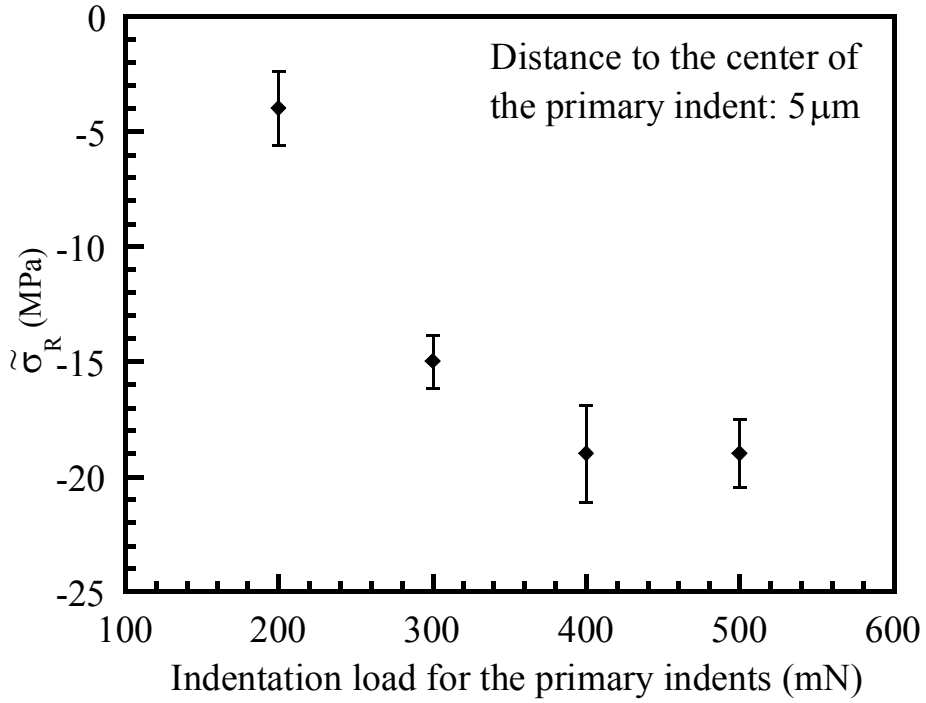

Figure 4.8. Dependence of the average residual stress on the indentation load for the primary indentation at a fixed distance of 5 μm from the center of the primary indent.

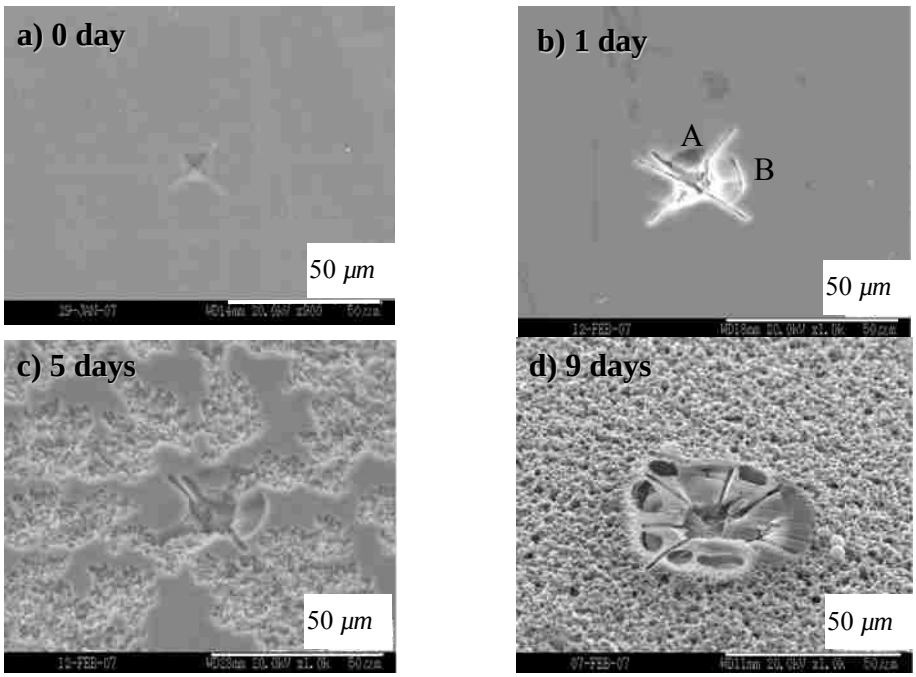

Figure 4.9. Morphological evolution around the indent as a function time (indentation load: 500 mN); a) 0 day, b) 1 day, c) 5 days, and d) 9 days (Note: the 45S5 bioactive glass shown was unannealed.)

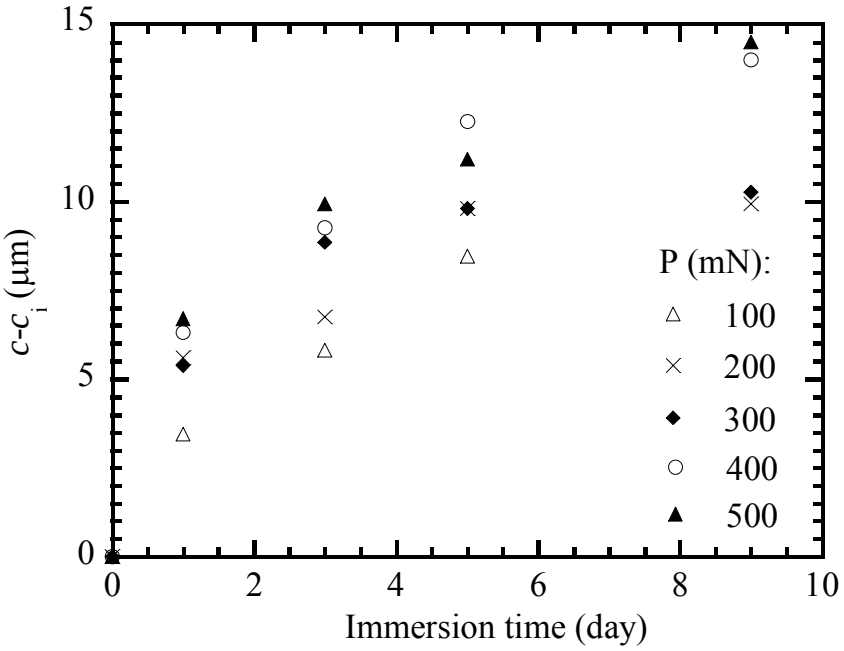

Figure 4.10. Growth of the crack length with time in the PBS solution for the cracks created by the primary indentations (c_i: half of the initial diagonal length of the indentation crack before in-vitro dissolution testing). Cracks with primary load of 100mN could not be found after 5 days immersion.

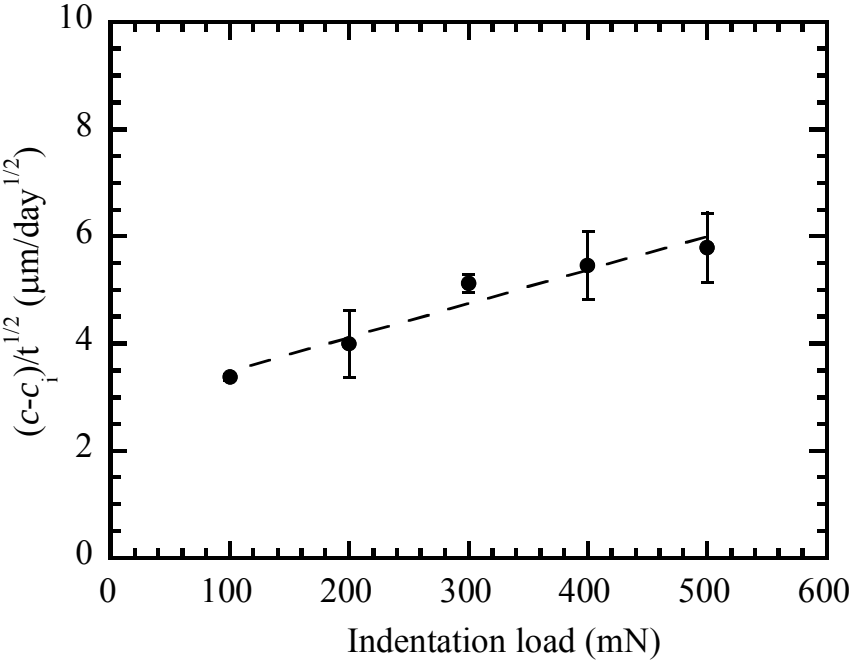

Figure 4.11. Dependence of the parameter of $(c - c_i)/\sqrt{t}$ on the indentation load

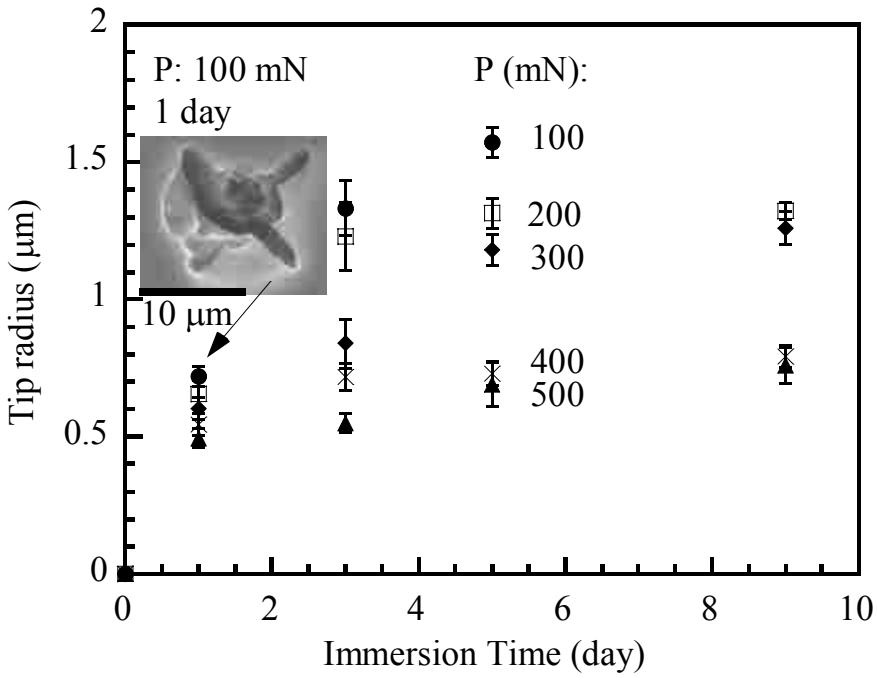

Figure 4.12. Growth of the crack tip with time in the PBS solution for the cracks created by the primary indentations. The embedded micrograph shows the lateral widening of the crack and the bluningt of the crack tip for the cracks made by an indentation load of 100 mN.

Chapter 5 Local surface damage and material dissolution in 45S5 bioactive glass using spherical indenter: Effect of the contact deformation

5.1. Background

Localized deformation can change local chemomechanical response of a bioactive material and alter the local dissolution and biofunctionality of the material. We used a spherical diamond indenter to study the indentation deformation of 45S5 bioglass, and to examine the effect of the indentation deformation on the material dissolution of 45S5 bioglass in the PBS solution. Ring cracks, radial cracks and local surface damage due to the contact between the indenter and the 45S5 bioglass are revealed. The dependence of the growth of the radial cracks on the indentation load is also discussed.

5.2. Experimental

The samples were cut, grinded and polished as described in Chapter 3. The polished samples then were heat-treated in air at 350ºC for 2 hours and furnace-cooled to room temperature to remove the residual stresses generated in the grinding and polishing before indentation.

Microindentations were made on the polished surface of the discs using a diamond, spherical indenter of 50 μm in radius on a Micro-Combi Tester (CSM Instruments, Needham, MA). The peak indentation load applied to the indenter was in the range of 500 mN to 3000 mN. The indentation loading-unloading rate was 500 mN/min; and the holding time was 5 seconds at the peak load. Arrays of indents were created with a minimum of 5 indents for each indentation load, and the spacing between two nearby indents was at least 3 times larger than the size of the indents. The impression marks were measured using an optical microscope and a scanning

electron microscope (SEM). After the indentations, the specimens were immediately stored in a desiccator.

The indented-samples later were placed into a PBS solution of ~1 L in an agitated water bath with the indented surface up. The PBS solution used was made as the procedures described in Chapter 3. The PBS solution was not agitated and was sealed to prevent from contamination and evaporation. The temperature was maintained at 37°C to mimic the body temperature. The specimens were immersed into the PBS solution over the periods of 1, 3, 5, 7or 9 days,

5.3. Results and discussion

5.3.1 Microindentation

Figure 5.1 depicts the SEM micrographs of the impression marks over a 45S5 bioglass by the indentation loads of 800 and 3000 mN prior to the immersion test. Both ring cracks and radial cracks are observed around the indents, depending on the indentation load. This is in contrast to the indentations made by a Vickers indenter, in which only radial cracks were observed[94]. There is only one ring crack for the indentation made by the indentation load of 800 mN. In contrast, there are multiple ring cracks and 6 radial cracks, as shown in Fig. 1b, emanating from the periphery of the indentation mark/the outmost ring crack for the indentation made by the indentation load of 3000 mN. This result suggests that the ring cracks were first formed at small indentation loads and the radial cracks were formed after the formation of the ring cracks at large indentation loads. The formation of the radial cracks was likely due to the stress concentration at the damaged surface in the 45S5 bioglass around the ring cracks, although there were no sharp edges on the surface of the spherical indenter. The stress concentration caused the formation and propagation of local radial cracks.

Figure 5.2 shows the dependence of the size of the impression marks on the indentation load. The indentation size varied linearly with the indentation load. Such

a behavior is different from the parabolic relation for the indentation of ductile materials and likely is due to the formation and propagation of the surface damage over the 45S5 bioglass during the indentation. More mechanical work was dissipated for the development of anelastic deformation.

From the size of the impression marks, d, one can calculate the indentation hardness, H, as

$$H = \frac{4P}{\pi \bar{d}^2} \quad (5.1)$$

where P is the peak indentation load and $\bar{d}$ is the average size of the impression marks. The dependence of the indentation hardness on the indentation load is depicted in Figure 5.3. The indentation hardness gradually increases from 3.5 GPa at the indentation load of 800 mN to 6.1 GPa at the indentation load of 2000 mN. For the indentation loads larger than 2000 mN, there is only a slight change in the indentation hardness, and the indentation hardness can be approximated as a constant of 6.2 GPa. This value is slightly less than 7.47±0.51 GPa obtained from the indentations made by a Vickers indenter[94]. Such a difference is due to the effect of the indenter-surface profile, which produces different stress distribution underneath the indentation.

For brittle materials, the indentation-induced surface cracks include the median crack, radial crack, and lateral crack. Approximating the indentation-induced median-radial cracks as centre-loaded half-penny cracks, Lawn et al. [145] obtained the relationship between the size of a median-radial crack and the indentation load for sharp indenters as

$$P = \chi c^{3/2} \quad (5.2)$$

where c is the distance between the center of the indentation mark and the crack tip, and χ is a constant depending on the mechanical properties of the material and the indenter profile. Equation (5.2) has been supported by various experimental results.

Recently, Dériano et al. [146] found that their experimental results of the indentation fracture of silica-rich glasses deviated from Eq. (5.2) and suggested that the deviation was due to the densification underneath the indentation and the formation of ring cracks.

Consider that the radial cracks started at the periphery of the ring cracks in the indentation of the 45S5 bioglass. It is reasonable to assume that the radial cracks can be approximated as quadrant-penny cracks with the center of the cracks being at the periphery of the outmost ring crack and are subjected to concentrated force at the center of the cracks due to the indentation deformation. Thus, the size of the radial crack becomes $(c - d/2)$; and one can modify Eq. (5.2) as

$$P = \chi(c - d/2)^{3/2} \quad (5.3)$$

Figure 5.4 shows the dependence of the crack size on the indentation load. The indentation load is proportional to the 3/2 power of $(c - d/2)$, supporting Eq.(5.3). This trend suggests that the ring cracks hindered the propagation of the radial cracks likely due to local densification underneath the indentation. Under such conditions, it is unclear if the fracture toughness of the 45S5 bioglass can be evaluated from the radial cracks created by spherical indentations.

The inelastic energy, E_{in}, dissipated in an indentation cycle is the area enclosed by the loading-unloading curve and the displacement axis that represents the energetic contribution to the formation and propagation of surface damage and local inelastic deformation. Using dimensional analysis, Chen et al. [106] showed that the inelastic energy is a power function of the indentation load as, $E_{in} \propto P^n$ (n is a force exponent). Figure 5.5 shows the dependence of the dissipated inelastic energy on the indentation load. In contract to the indentation of ductile materials[106], [147], [107], there are two force exponents. For the indentation loads less than or equal to 1000 mN, the force exponent is 1.5, which is consistent with the dimensional analysis for perfect plastic materials. For the indentation loads larger than 1000 mN,

the force exponent is 2.6, which suggests that more mechanical work was dissipated in the indentation cycle. The difference is likely due to the formation and propagation of the radial cracks. At large indentation loads, the radial cracks were created as indicated in Fig. 4, which produced new crack surfaces in addition to local surface damage and inelastic deformation. The formation of the radial cracks required the compensation of surface energy from the mechanical work. This resulted in more dissipation of mechanical work and the high force exponent. Obviously, there exists a critical indentation load, at which the radial cracks will start to nucleate during the indentation of the 45S5 bioglass.

5.3.2 Material dissolution

The effect of the indentation deformation on the dissolution behavior of the 45S5 bioglass was studied following the indentations. The indented 45S5 bioglass were immersed in a PBS solution at temperature of 37 °C to mimic the body temperature. Figure 5.6 shows the sequence of the surface evolution around the indents by an indentation load of 3000 mN in the PBS solution. The region around the cracks first underwent the material dissolution as shown in Fig. 5.6b, which suggests the stress-assisted reaction for the material dissolution. The material dissolution widened the gaps between the crack surfaces. Severe dissolution occurred over the contact zone, which revealed multiple ring-type grooves and debris. This is consistent with the observation of the ring cracks. The presence of the debris indicates that local subsurface damage and densification were produced during the indentation. Continuous exposure to the PBS solution led to more material dissolution over the damaged area and deep dissolution along the cracks, as shown in Figs. 5.6c and 5.6d. In the meantime, the exposure to the PBS solution also caused random dissolution of materials over the surface away from the area surrounding the indents as shown in Fig. 5.6e. A typical surface morphology of a 45S5 bioglass is shown in Fig. 5.6f after continuous exposure to the PBS solution for 9 days. The entire surface experienced

the material dissolution and became rough except the area surrounding the indents produced by the indentation loads larger than 2000 mN, which became much smooth. This is likely due to the residual compressive stresses created by the indentations, which hindered the dissolution of the 45S5 bioglass in the PBS solution over a long period of the immersion. It should be pointed out that the deformed surfaces created by the indentation loads less than 1500 mN were completely dissolved after 1 day.

Figure 5.7 shows the material dissolution at an crack tip after 1 day's immersion in the PBS solution for the indentation made by an indentation load of 3000 mN. The crack tip blunted and the gap between the crack surfaces became wide. This is due to local residual, tensile stress, which assisted the material dissolution. All of these results suggest that the dissolution behavior of the 45S5 bioglass is a function of local stress state.

Figure 5.8 shows the dependence of the distance of the crack tip to the indentation center on the immersion time for the radial cracks. The crack size increases with the increase in the immersion time. The growth speed for the cracks made by large indentation loads is higher than that for the cracks made by small indentation loads since large indentation load created higher local residual stress at the crack tip than that made by small indentation load. It is worth pointing out that the radial cracks produced by the indentation load of 1000 mN were completely dissolved after 1 day's immersion. This suggests that the radial cracks did not pass through the indentation-created plastic zone.

It is believed that water reacts with glasses in the vicinity of a crack tip and weakens the bond strength. This allows the propagation of cracks in aqueous environment when subjected to local residual-tensile stress. (i.e. stress-assisted cracking). The stress-assisted cracking process is complex, which can be divided into three regions [148]. In region I, the crack growth is activated through the chemomechanical interaction between water and the material and the growth speed is a function of the local stress. In region II, the crack-growth speed is much faster than the reaction rate for the chemomechanical interaction and the growth behavior is independent of atomic motion at the crack tip. In region III, the crack growth is

related to the bond rupture.

Several models [149] have used the stress-assisted chemical reaction theory to analyze the stress-assisted crack growth and associated the crack-growth speed with the stress intensity factor or the strain energy release rate. From the rate theory [150], Sergo et al. [151] suggested that the stress-assisted dissolution is a function of the hydrostatic stress. Thus, following the analysis given by Pollet and Burns [152], one can express the dependence of the crack-growth speed, V, on the local stress in the vicinity of a crack tip in the region of the stress-dependent crack growth as

$$V = A\exp\left(\frac{-Q}{RT}\right)\sinh\left(\frac{\sigma_h\Omega - R_E}{RT}\right)$$

(5.4)

where A is a constant dependent upon the lattice-vibration frequency and atomic space, Q is the activation energy of the adsorption-desorption procession, R is the gas constant, T is the absolute temperature, Ω is an activation volume, and R_E is two time of the solid-liquid interface energy. σ_h is the trace of the stress tensor in the front of the crack tip, which is positive for tensile stress and negative for compressive stress. For $\sigma_h\Omega - R_E << RT$, Eq. (5.4) can be simplified as

$$V = A\exp\left(\frac{-Q}{RT}\right)\frac{\sigma_h\Omega - R_E}{RT}$$

(5.5)

In general, one can assume $\sigma_h \propto P$ if the characteristic time for the relaxation of the local stress in the vicinity of the crack tip is much larger than the immersion time. Thus, Eq. (5.5) becomes

$$V = A\exp\left(\frac{-Q}{RT}\right)\frac{\alpha P - R_E}{RT}$$

(5.6)

The growth speed of the radial cracks is a linear function of the indentation load. From Fig. 5.8, one can calculate the crack-growth speed through the curve fitting.

Figure 5.9 shows the dependence of the crack-growth speed on the indentation load. A linear relation is observed between the crack-growth speed and the indentation load, which is in good accordance with Eq.(5.6). The result suggests the presence of the stress-assisted crack propagation in the 45S5 bioglass, when the indented 45S5 bioglass was immersed in the PBS solution. The crack growth is associated with the stress-assisted material dissolution in the vicinity of the crack tip. The local stress can enhance or suppress the dissolution of material and the propagation of surface cracks in the PBS solution, dependent upon the stress state.

5.4 Summary

The biofunctionality of bioactive glasses depends on the chemomechanical interaction in the human physiological solution. Using the microindentation technique, the local deformation of the 45S5 bioglass was studied, and the behavior of the material dissolution around the indents was investigated. For the indentations made by the indentation loads of larger than 1000 mN, the radial cracks were created in addition to the multi-ring cracks over the contact zone. The indentation hardness gradually increased with the indentation load and reached a constant of 6.2 GPa for the indentation load larger than or equal to 2000 mN. An empirical relation was proposed to correlate the size of the radial cracks with the indentation load that was supported by the experimental results. The inelastic energy dissipated in an indentation cycle was a power-function of the indentation load with a transition from a small force exponent of 1.5 to a large force exponent of 2.6 at the indentation load of 1000 mN. The transition likely corresponded to the formation of the radial cracks, which emanated from the periphery of the ring cracks.

The effect of the indentation deformation on the dissolution behavior of the 45S5 bioglass in the PBS solution was examined. The bioglass surrounding the indents experienced different dissolution behavior from the surface away from the indents. Fast dissolution occurred over the indentation-created damaged zone, including the

edges of the cracks. Multiple small debris and ring-type grooves were observed. This suggested that, in addition to the ring cracks over the contact zone, the indentation created local subsurface damage underneath the indentation. The depth and width of the grooves and the cracks increased with the immersion time. Smooth surface was formed over a long period of the immersion surrounding the indents that was likely due to the confinement of the material dissolution controlled by local compressive, residual stress. In contrast, the bioglass away from the indentation-influenced zone showed random dissolution in a short time period and eventually grew over the entire stress-free surface.

The growth of the radial cracks in the PBS solution showed the stress-corrosion behavior, falling into the category of the region I. A simple relation was proposed between the crack-growth speed and the indentation load from the rate theory. The experimental results for the crack growth of the radial cracks supported this relationship. Local material dissolution and the tip blunting were also demonstrated. All of these results indicate the potential of using local stresses to control the biofunctionality of bioactive glasses in the human physiological solution.

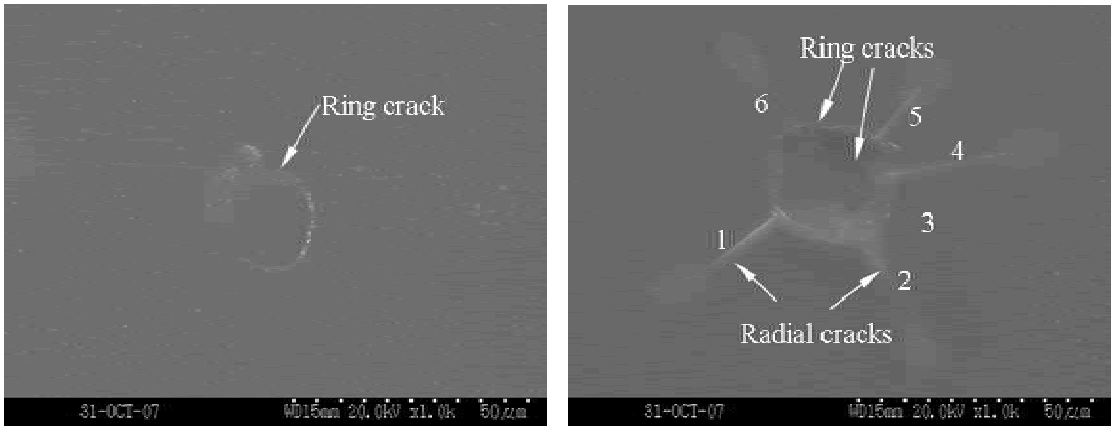

Figure 5.1. Surface cracks created by the spherical indentations, a) a ring crack (indentation load: 800 mN), and b) multiple ring cracks and six radial cracks (indentation load: 3000 mN).

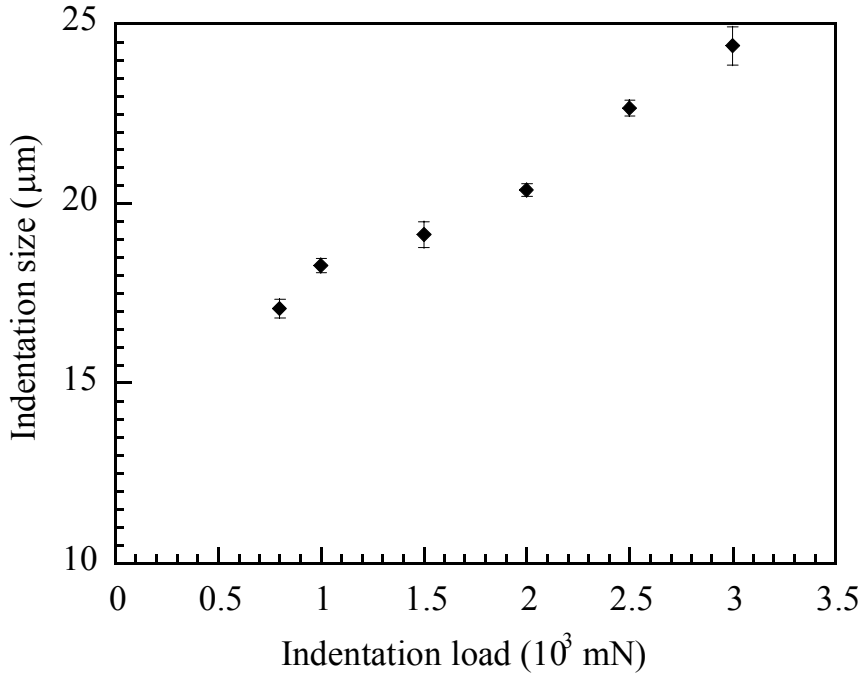

Figure 5.2. Dependence of the indentation size on the indentation load

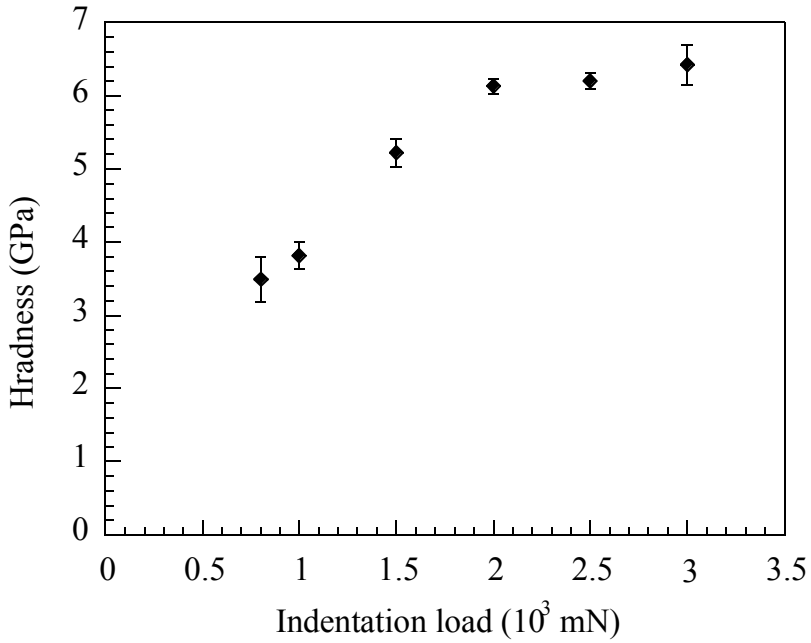

Figure 5.3. Dependence of the indentation hardness on the indentation load

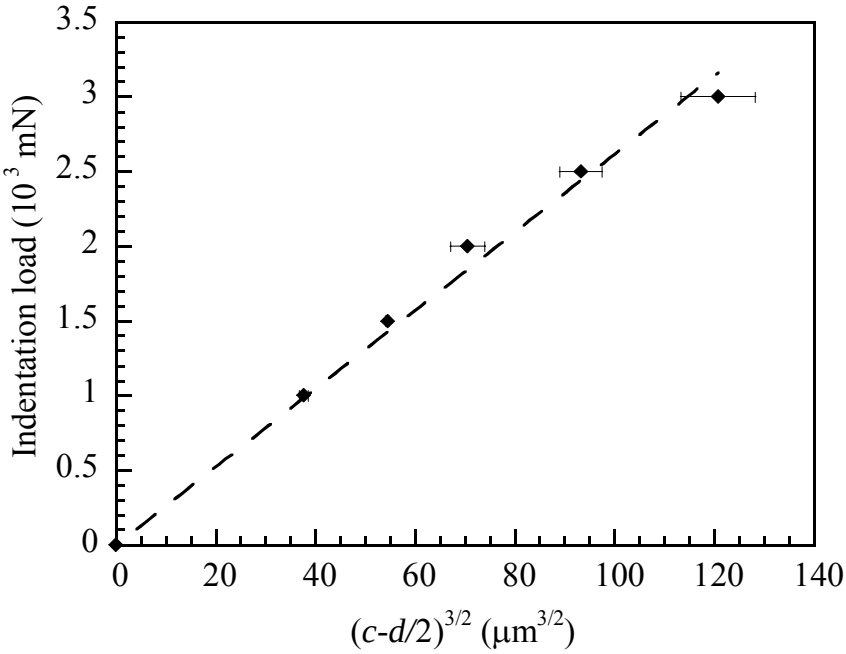

Figure 5.4. Dependence of the size of the indentation-created radial cracks on the indentation load

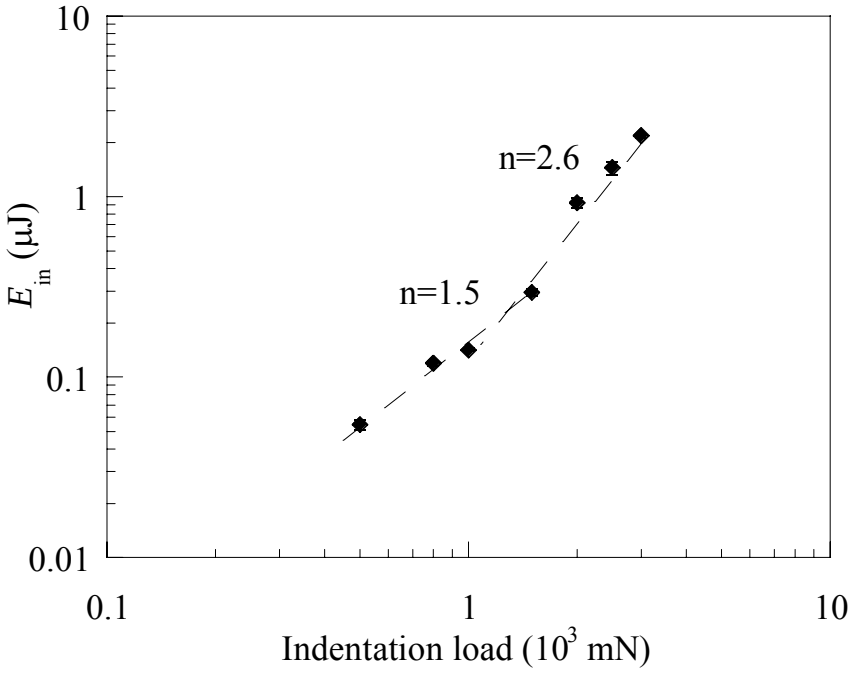

Figure 5.5. Dependence of the inelastic energy on the indentation load

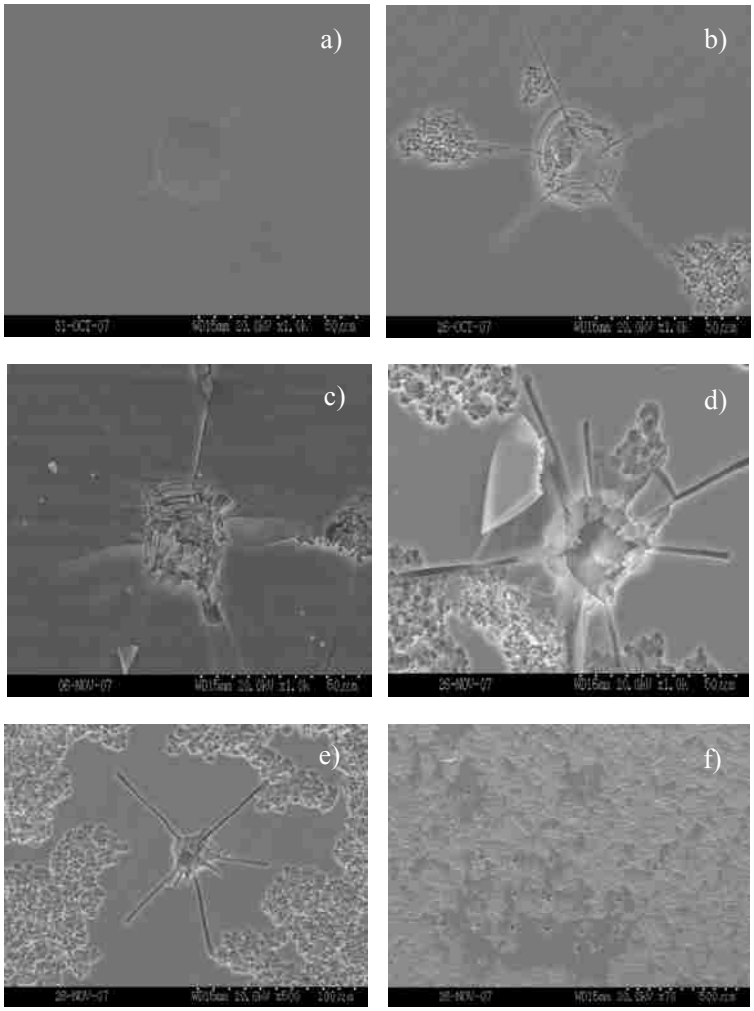

Figure 5.6. SEM micrographs of the morphological evolution around the indents (indentation load: 3000 mN); a) as-indented surface, b) 1-day's dissolution, c) 3-days' dissolution, d) 9-days' dissolution, e) an enlarged view of the surface topology around the indent, and f) the global view over the indentation region.

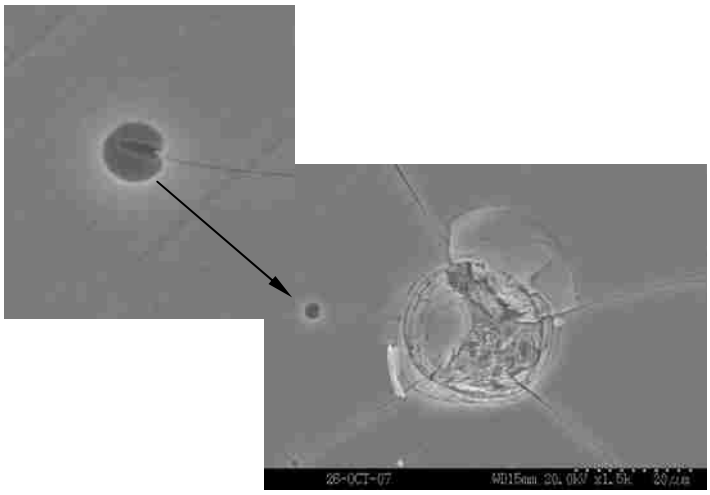

Figure 5.7. Material dissolution at the crack tip for an indent created by an indentation load of 3000 mN (immersion time: 1 day).

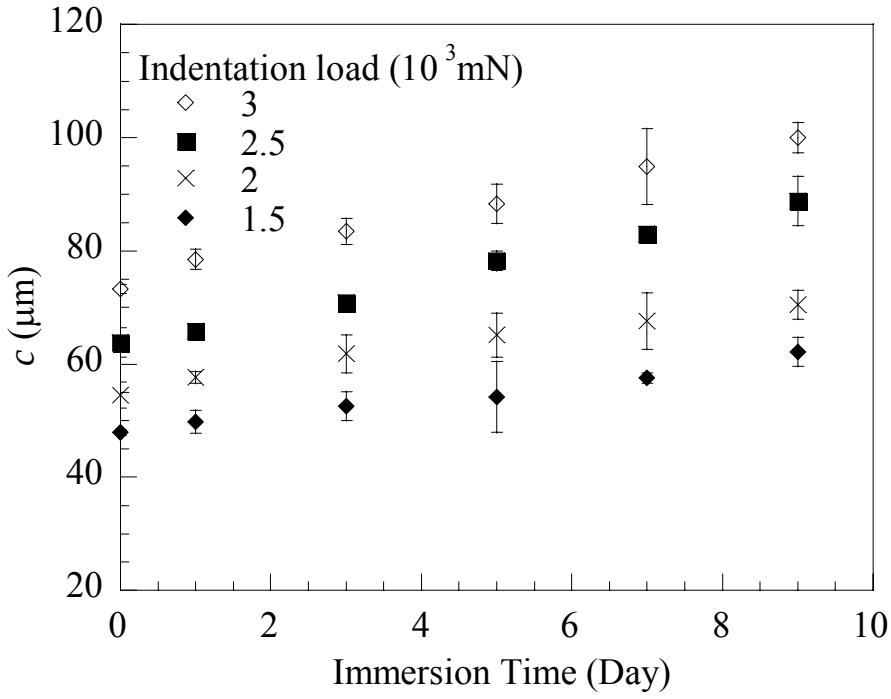

Figure 5.8. Dependence of the distance of the crack tip to the indentation center on the immersion time for the radial cracks

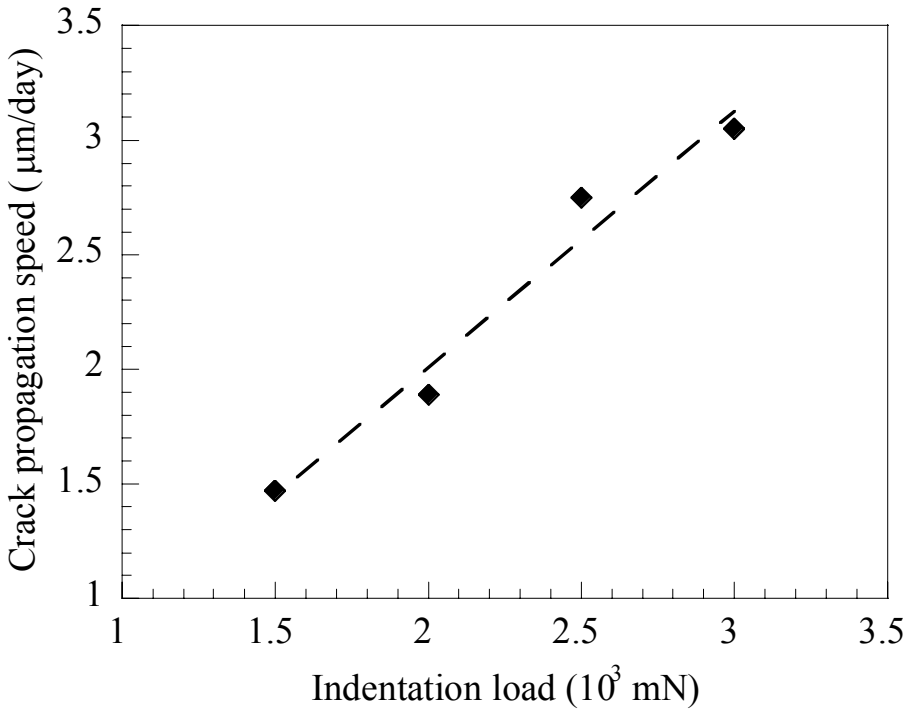

Figure 5.9. Dependence of the crack propagation speed on the indentation load

Chapter 6 Indentation Behavior of Crystallized 45S5-Bioglass

6.1. Background

We previously studied the effect of localized stress on the dissolution of 45S5-bioglass of vitreous state in phosphate buffer solution and stress-dependent dissolution of the 45S5-bioglass. Considering the importance of the effect of crystallinity on the mechanical strength and bioactivity of crystallized bioglasses for the implant applications of bioactive glasses, we next focused on studying the localized mechanical deformation of crystallized 45S5-bioglass, the material dissolution and the formation of hydroxyapatite-surface layer. The contact modulus, indentation hardness, and fracture toughness are evaluated, using the microindentation technique. The formation of hydroxyapatite-surface layer over the crystallized 45S5-bioglass is examined in phosphate buffer solution (PBS).

6.2. Experimental

Sample Preparation

The samples were cut, grinded, polished and annealed as described in Chapter 3. The annealed samples were immediately dried with compressed air and followed by desiccation for at least one day before indentation.

Indentation

Microindentations were made on the polished surface of the crystallized 45S5-bioglass, using a diamond Vickers indenter on a Micro-Combi Tester (CSM Instruments, Needham, MA). The maximum indentation loads (F_{max}) varied from 100mN to 500mN. The loading rate was 200 mN/min, and there was a holding time of 5 s at the peak indentation load. The loading-unloading curves were recorded, and

the sizes of the indentation marks and the crack lengths were measured, using an optical microscope immediately after the indentation. The indented samples were stored in a desiccator following the indentation. Arrays of indents, with a minimum of 5 indents per maximum indentation load (spaced at least 3 times of the indent size between the indents), were created prior to *in vitro* immersion testing.

In vitro immersion testing

The indented discs with the indented surface up were placed in a PBS solution of ~ 1 L in an agitated water bath to maintain a uniform temperature of 37 °C. The PBS used was made following the procedures described in Chapter 3. The specimens were respectively immersed into the PBS for 1, 3, 4, 5, 7, and 9 days.

Materials characterization

X-ray diffraction of the as-received 45S5-bioglass was performed, using a Bruker AXS diffractomer (Siemens) with scanning between 10° and 80° and a scanning rate of 1 °/minute. Scanning electron microscopy (SEM) with energy dispersive x-ray capability (EDS) was performed to characterize the surface morphology of the indentation imprints on a Hitachi S3200 instrument. The indented and immersed 45S5-bioglass discs were gold-palladium-coated prior to SEM. The samples were stored in a desiccator between the characterization studies.

6.3. Results and discussion

The X-ray diffraction was conducted to examine 45S5-bioglass in both vitreous state and crystalline state. For the 45S5-bioglass in vitreous state, there is a broad diffraction peak that corresponds to an amorphous structure. No peaks associated with any crystalline phase can be observed. Figure 6.1 shows the X-ray diffraction patterns of the crystallized 45S5-bioglass after the heat treatment (650 ºC for 8

hours). Obviously, the 45S5-bioglass was fully crystallized, and there was no glass structure present in the material. Figure 6.2 shows a typical microstructure of the crystallized 45S5-bioglass. The grain size of the crystallized 45S5-bioglass was determined to be about 40 microns. Instead of grain boundary groove, grain boundary ridges were present over the surface, suggesting the possible segregation over the grain boundaries in the crystallized 45S5-bioglass.

6.3.1 Indentation characteristics

The indentation tests were carried out using the load-control mode. Prior to a full indentation, a pre-load of 5 mN was applied to the indenter in order to maintain the contact between the indenter and the surface of the sample and to avoid the effect of impact. Figure 6.3 shows typical indentation loading-unloading curves for the indentation of the crystallized 45S5-bioglass. There exists slight difference in the loading curves for three different peak-indentation loads that is likely due to the effects of local inhomogeneity and crystal orientation.

Figure 6.4 shows typical SEM micrograph of the surface morphology surrounding an indent made by an indentation load of 400 mN. Both edge cracks and radial cracks have been observed around the indent, depending on the indentation load. The formation of the radial cracks was likely due to the stress concentration at the edges of the Vickers indenter, and the formation of the edge cracks was due to the surface-tensile stress created by the indentation. The surface-tensile stress caused the formation and growth of local edge cracks and subsurface damage in the crystallized 45S5-bioglass.

The dependence of the diagonal length of the impression marks, D, on the indentation load, F, is depicted in Fig. 6.5. Using a curve-fitting, one obtains $D = 0.50F^{1/2}$ (D is in the unit of micrometer, and F is the indentation load in the unit of milli-Newton). The indentation size proportionally varied with the square root of the indentation load. Such a behavior is different from the linear dependence

of the indentation size on the indentation load for the indentation of 45S5-bioglass by spherical indenters [153]. This is likely due to the microstructural effect; one material was in vitreous state and the other in crystalline state.

Form the size of the indents, one can use the following equation to calculate the Vickers hardness,

$$H = \frac{1.854F}{\bar{D}^2} \quad (6.1)$$

where $\bar{D}$ is the average diagonal length of the indents. Using the curve-fitting result of Fig. 6.5, the average Vickers hardness is calculated as 7.42 GPa. Figure 6.6 shows the variation of the Vickers hardness with the indentation load, in which the Vickers hardness was calculated by using the average diagonal length of indents and the corresponding indentation load. There are scatterings around the average Vickers hardness, depending on the indentation load. Such scatterings are likely due to local inhomogeneity in the crystallized 45S5-bioglass. From Fig. 6.5, one obtains the Vickers hardness of 7.42±0.95 GPa, which is the same as 7.47±0.51 GPa obtained from the indentations of vitreous 45S5-bioglass [94]. The crystallization has no significant effect on the indentation hardness, which represents the plastic deformation under the localized loading.

It is known that the unloading behavior of a material at the onset of unloading is mainly controlled by elastic recovery is used to calculate the contact modulus. Figure 6.7 shows the dependence of the contact modulus on the indentation load. The contact modulus decreases with the increase in the indentation load due to the formation and propagation of subsurface damage underneath the indentation. The indentation-induced subsurface damage caused less elastic recovery. Using the results shown in Fig. 7, one obtains the average contact modulus as 12.14±1.15 GPa, which is less than 43.33 GPa for the 45S5-bioglass in vitreous state (the Young's modulus of 45S5-bioglass in vitreous state is 32.5 GPa [94] and the Poisson's ratio is assumed as 0.5 in the calculation). Such a difference likely reveals the formation of defects, such as grain boundaries, during the crystallization and the indentation-induced subsurface

damages which reduces the apparent contact modulus of the crystallized 45S5-bioglass.

As shown in Fig. 6.4, both the radial and edge cracks were formed during the indentation. This phenomenon suggests that the crystallized 45S5-bioglass is brittle. Following the approach given by Evans and Charles [154], one can approximate the indentation-induced radial cracks as center-loaded half-penny cracks and express the load dependence of the size of the radial cracks as

$$F = \frac{K_{IC}}{\delta}\left(\frac{E}{H}\right)^{-1/2} c^{3/2}$$

(6.2)

where K_{IC} is the fracture toughness, δ is an empirical constant of 0.016 ± 0.004 for the Vickers indentation [155], and E is Young's modulus of the material. Figure 6.8 shows the dependence of the diagonal length of the radial cracks on the indentation load. The indentation load is proportional to the 3/2 power of the diagonal length of the radial cracks in accord with Eq.(6.2). This suggests that the indentation-induced radial cracks during the indentation of the crystallized 45S5-bioglass can be approximated as centre-loaded half-penny cracks. Using the indentation hardness of 7.42 GPa and the Young's modulus of 9.11 GPa (as calculated from the contact modulus with the Poisson ratio of 0.5), one obtains the fracture toughness of 0.038±0.004 MPa·m$^{1/2}$. The fracture toughness of the crystallized 45S5-bioglass is about 3 times less than the fracture toughness of 0.11±0.02 MPa·m$^{1/2}$ of annealed 45S5-bioglass [94]. Obviously, the crystallized 45S5-bioglass is much more compliant and weaker than the 45S5-bioglass in vitreous state. Thus, 45S5-bioglass in vitreous state is preferred for clinic applications.

6.3.2 Material dissolution and precipitation

The effect of the indentation deformation on the dissolution behavior of the

crystallized 45S5-bioglass was studied. Figure 6.9 shows the dissolved surface away from the indents after one-day's and three-days' immersion. There are random dissolutions over the surface of unindented area. Faster dissolution occurred at the grain boundaries. Materials were leached into the PBS solution, while the grain boundary ridges dissolved at much slower rate than that of the surrounding materials. This is likely due to the segregation in the grain boundaries, which increases the resistance to the dissolution in the PBS solution. After five-days' immersion, precipitation occurred over entire surface of the crystallized 45S5-bioglass that prevented further observation of the dissolution around the grain boundaries and the material surface.

Figure 6.10 shows the surface evolution of the crystallized 45S5-bioglass around the indents after various times of immersion in the PBS solution. In addition to material dissolution over the damaged surface by the indentation, material dissolution occurred randomly over the surface of the crystallized 45S5-bioglasses after one day's immersion; faster dissolution was observable over the damaged zone than that in the undamaged area. The faster dissolution likely was due to stress-corrosion cracking and material removal in the solution. Broadening and growth of surface cracks were noticeable similar to the growth of cracks as observed in the 45S5-bioglass of vitreous state [94]. The material dissolution progressed in both the vertical and the lateral directions with high dissolution rate in the lateral/radial direction. Such behavior reflected the effect of surface diffusion, a fast process for atomic migration, which allowed the dissolved material to diffuse away from the surface at a fast rate in the lateral/radial direction. In contrast, there was no significant material dissolution along the lateral direction around the sites of the indents. This is due to the effect of residual stresses as created by the indentation. According to the rate theory [14, 15], atomic mobility is a function of local residual stress with compressive stress suppressing atomic migration and limiting the material dissolution. The lack of lateral material dissolution around the indents reflects the presence of local compressive stress as created by the indentation, which is in accord with the observation in the indentation of 45S5-bioglass of vitreous state

[94].

After four days' immersion, precipitation occurred. Precipitates of rectangular prism as shown in Fig. 6.10 began to nucleate and were present randomly over the surface. There is a needle-type precipitate, likely dicalcium phosphate for the indentation made by an indentation load of 400 mN. The remnants of the indentation sites are still visible. Such multifaceted precipitates are different from the spherical precipitates present in the immersion of 45S5-bioglass of vitreous state [156] and suggest that the precipitates are in a crystal state. Significantly different surface morphology is observed after five-days' immersion in the PBS solution. There is a mineralized layer covering the entire surface of the crystallized 45S5-bioglass. The indent sites become invisible. In comparison with the formation of the mineralized layer over a 45S5-bioglass of vitreous state after two weeks' immersion, the results indicate that the presence of the crystal structure enhances the formation rate of the mineralized layer.

To characterize the chemical composition of the mineralized layer, Energy Dispersive. Spectroscopy (EDS) was used to examine the ionic relationship among calcium, phosphate and silica. Table 1 lists the EDS results. There is little change in the calcium-silica ratio for the first five-days' immersion and a decrease in the calcium-phosphate ratio with the immersion time. There is a formation of a hydroxyapaptite layer (Ca/P ratio of 1.68 by EDS) after seven-days' immersion and a formation of dicalcium phosphate (Ca/P ratio of 1.25 by EDS) after nine-days' immersion. It is very difficult if not impossible to evaluate the effect of localized deformation on bioactivity and biofunctionality of the crystallized 45S5-bioglass without *in vivo* testing. However, the presence of localized deformation changes the dissolution rate of the crystallized 45S5-bioglass as shown in Fig. 6.9 for the immersion in the PBS solution up to four days.

6.4 Summary

Using the microindentation technique, the localized deformation of the fully crystallized 45S5-bioglass was studied, and the behavior of material dissolution around the indents was investigated in the indentation load range of 100 mN to 500 mN. Both the radial and edge cracks were created during the indentation, which introduced subsurface damage underneath the indentation. An indentation hardness of 7.42±0.95 GPa was obtained, which is independent of the indentation load under the experimental conditions and the same as 7.47±0.51 GPa obtained from the indentations of vitreous 45S5-bioglass. The contact modulus slightly decreased with the increase in the indentation load due to the formation and propagation of subsurface damage underneath the indentation, and the average contact modulus was 12.14±1.15 GPa about 3 times less than that for 45S5-bioglass of vitreous state. The fracture toughness of the crystallized 45S5-bioglass was also about 3 times less than that of annealed 45S5-bioglass in vitreous state.

The effect of the indentation deformation on the dissolution behavior of the crystallized 45S5 bioglass in the PBS solution was examined. Random surface dissolution was present with fast lateral dissolution rate over the undeformed surface. Surface precipitation occurred after four days' immersion, and a mineralized layer was formed over the entire surface of the crystallized 45S5 bioglass after five days' immersion. There was a decrease in the calcium-phosphate ratio with the immersion time. It was proven that a hydroxyapaptite layer (Ca/P ratio of 1.68 by EDS) was formed after seven-days' immersion and a dicalcium phosphate (Ca/P ratio of 1.25 by EDS) was formed after nine-days' immersion.

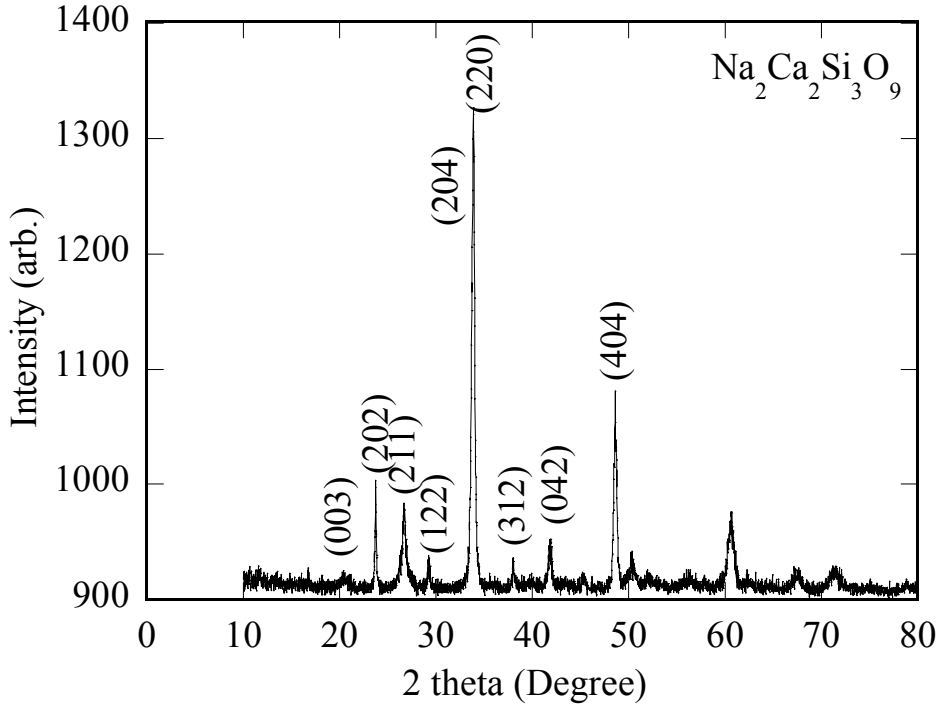

Figure 6.1. XRD diffraction patterns of fully crystallized 45S5-bioglass

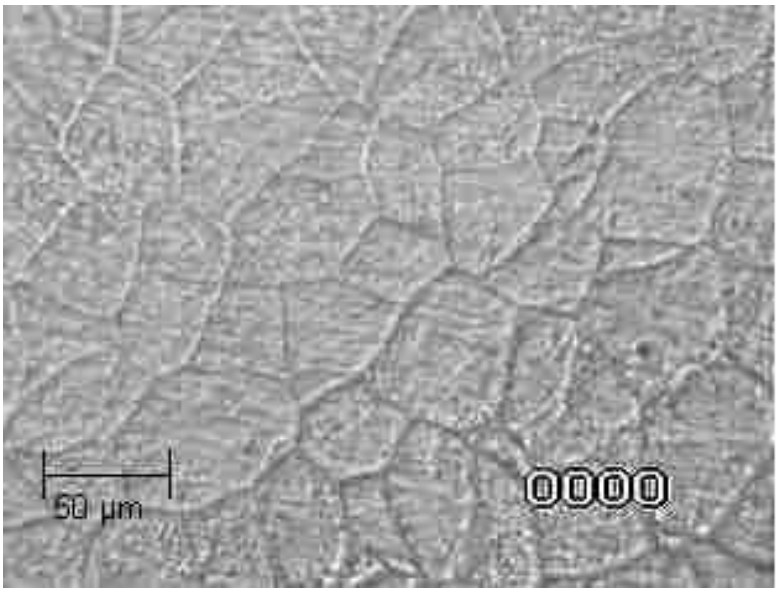

Figure 6.2 Microstructure of the crystallized 45S5-bioglass

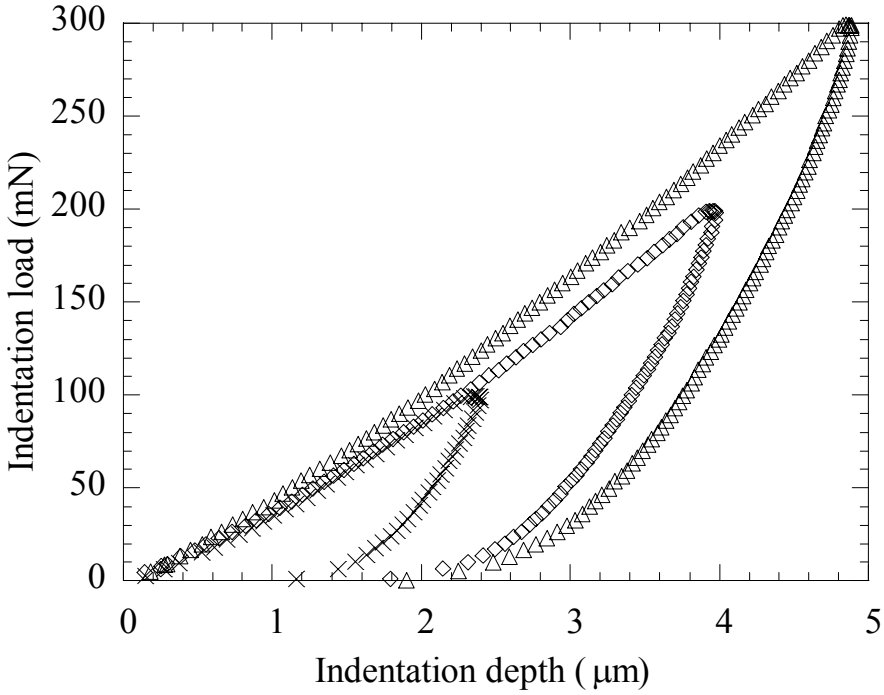

Figure 6.3. Typical indentation curves for the indentation of the crystallized 45S5-bioglass

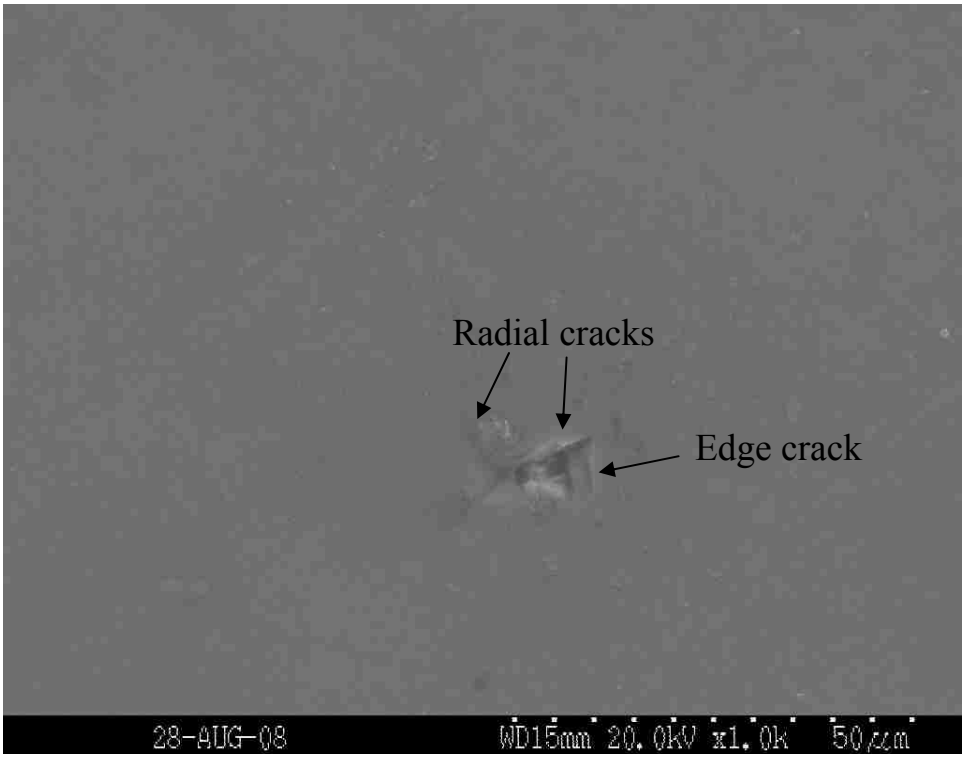

Figure 6.4. Surface cracks created by the indentation at an indentation load of 400mN

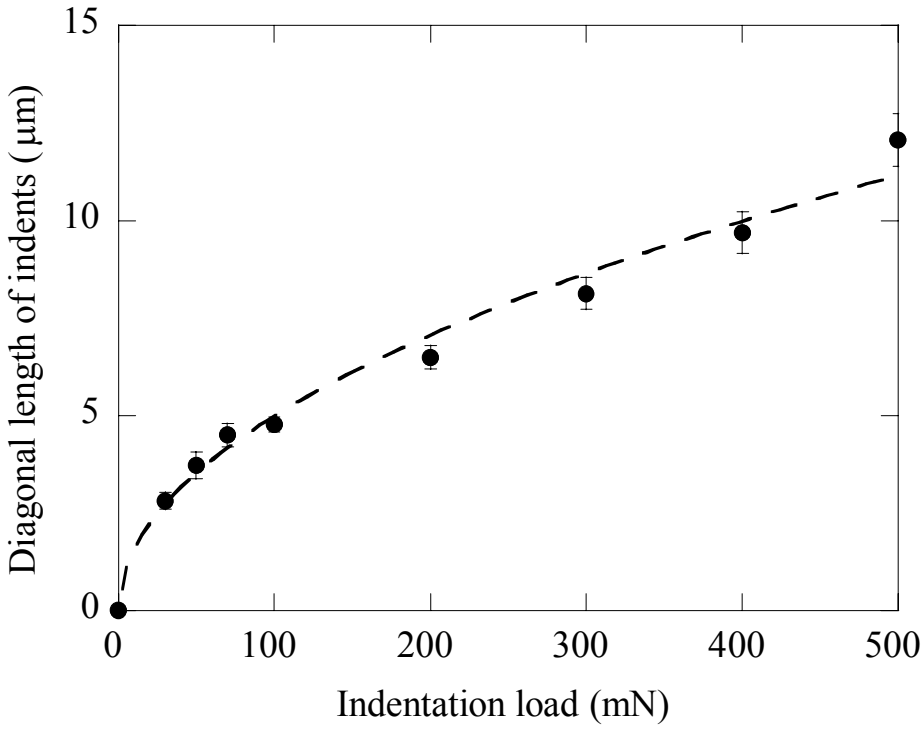

Figure 6.5. Dependence of the diagonal length of indents on the indentation load

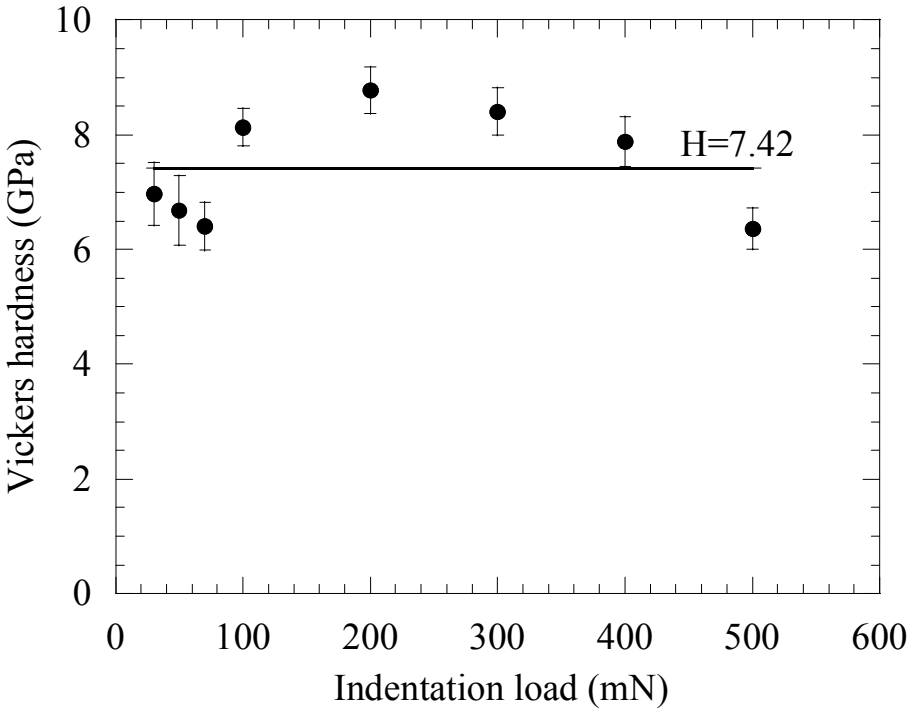

Figure 6.6. Variation of the Vickers hardness with the indentation load

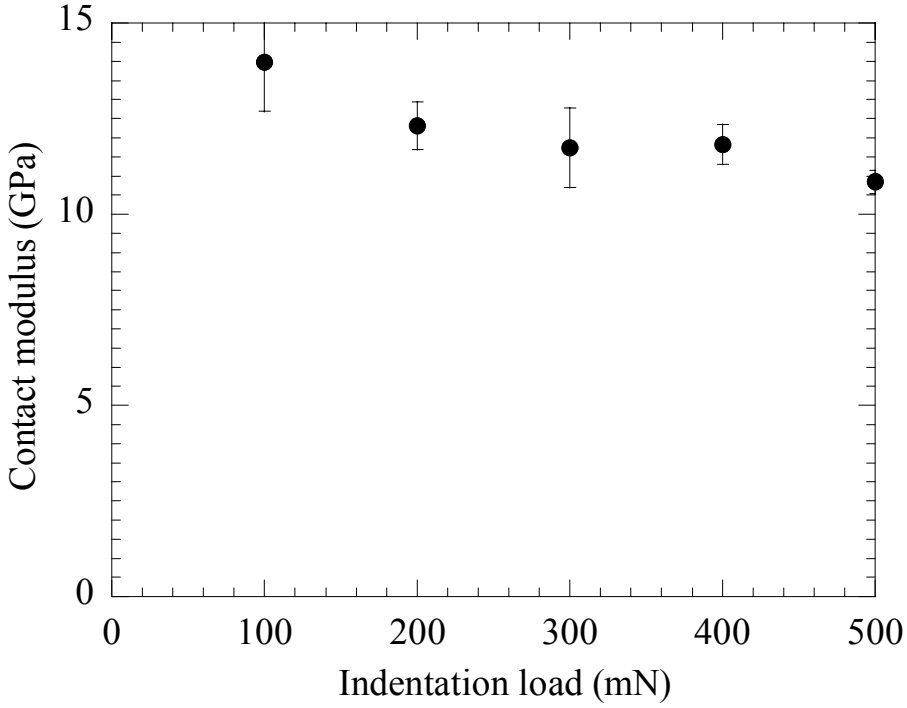

Figure 6.7. Dependence of the contact modulus on the indentation load

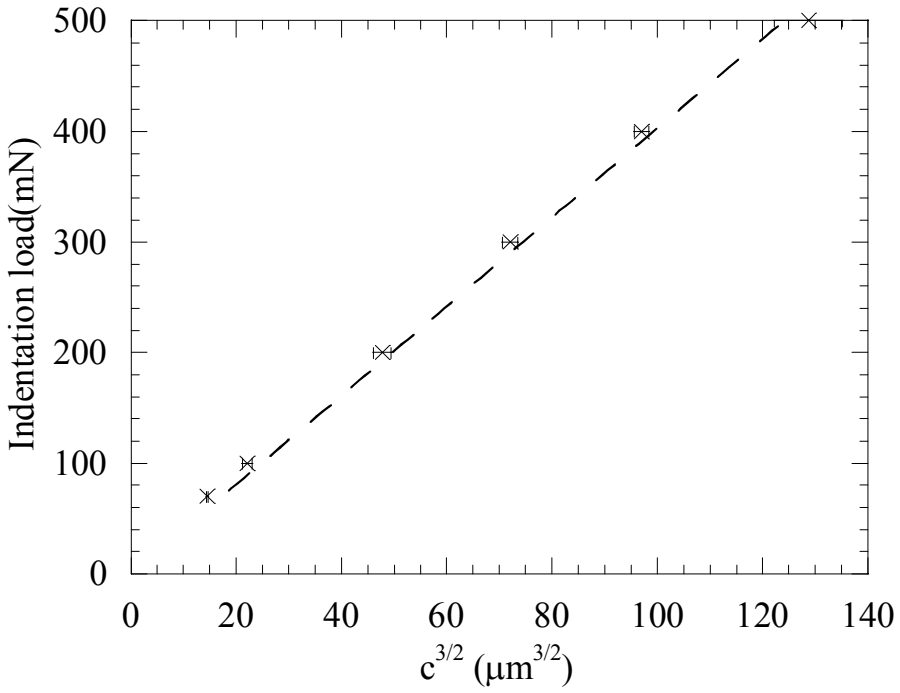

Figure 6.8 Dependence of the size of the radial cracks on the indentation load

a)

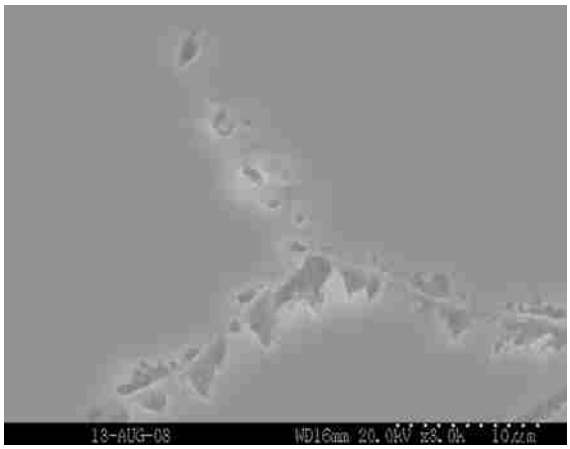

b)

Figure 6.9. Surface dissolution of the crystallized 45S5-bioglass after immersion in PBS; a) 1 day's immersion and b) 3 days' immersion.

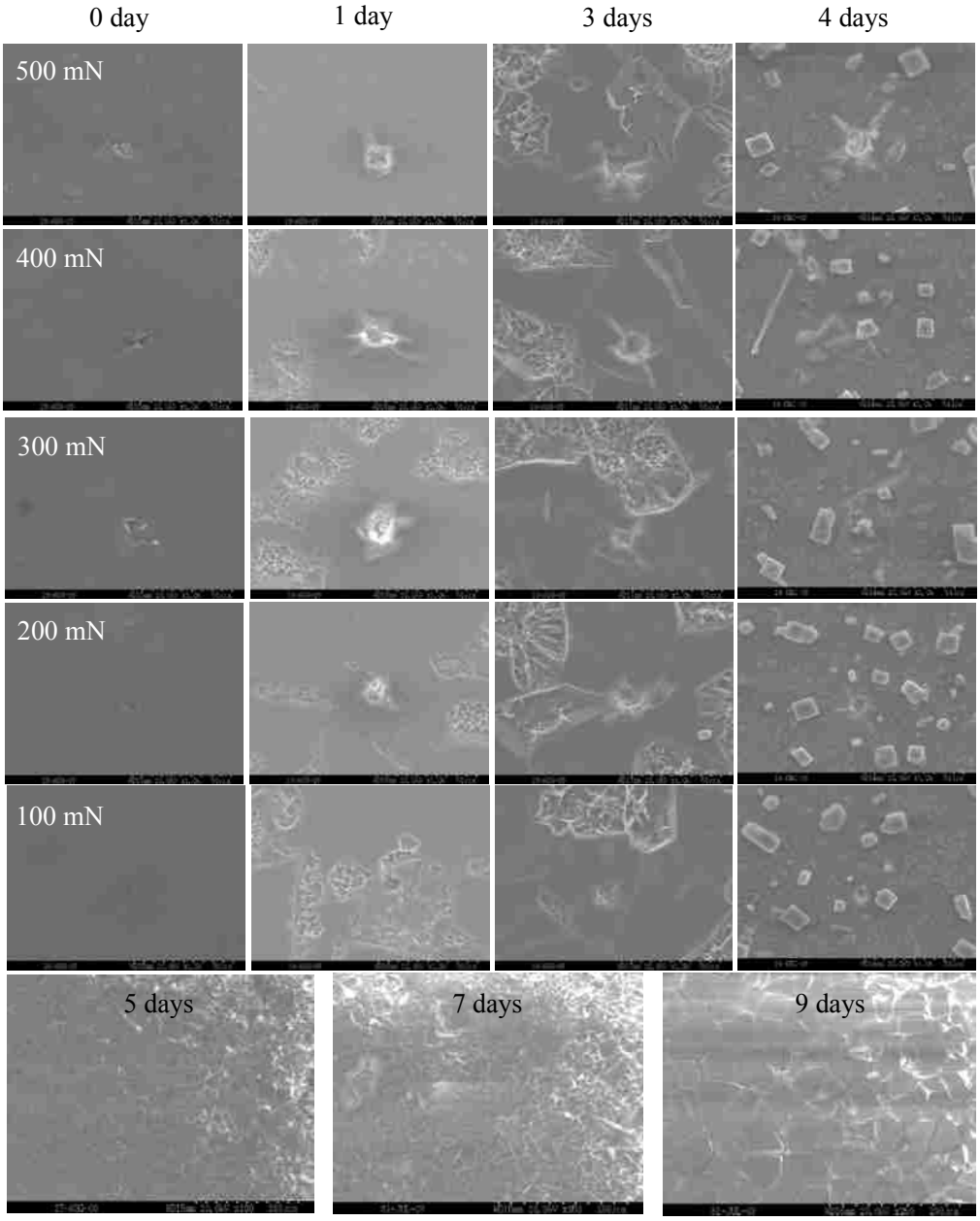

Figure 6.10. SEM micrographs of the surface evolution of the crystallized 45S5-bioglass around the indents after various times of immersion in the PBS solution

Chapter 7 Localized mechanical behavior of Ca-P precipitate layers

7.1 Introduction

The understanding of bioactivity and mechanical behavior of bio-implanted materials is an important area in the research and development of biomaterials. There are two approaches generally used to evaluate the bioactivity of bio-implanted materials. The first involves the assessment of the formation ability of an apatitic layer over a solid surface in simulated body fluid (SBF), which is an *in vitro* test as developed by Kokubo et al. [157]. This approach has been used to test bioactivity of various materials, including metals [158], [159], ceramics [160], [161], and polymers [162], [163]. The second is the bioactivity index, I_b, of a biomaterial which is related to the time taken for the material to form more than 50% bond with bone upon implantation ($100/t_{0.5bb}$, bb-bond to bone) [164]. Both approaches depend on kinetics of the apatite formation in physiological or simulated physiological environment. To understand the kinetics of the apatite formation in physiological environment, Prakash et al. [165] assumed a linear relation between the thickness of the apatite layer and the concentration of PO_4^{3-} ions in SBF and developed a semi-empirical relation for the time dependence of the apatite layer thickness by introducing an equilibrium thickness of the apatite layer, which is a curve-fitting parameter. However, their analysis did not consider the effect of ion migration on the growth of the apatite layer.

The apatite layer offers a good interface between implanted materials and physiological fluid not only to induce ingrowth of natural bone but also to bear mechanical loading because of mechanical contact at joints. The mechanical properties of apatites play an important role in controlling the service life and performance of implanted materials and the ingrowth of natural bone. However, there are only limited reports on mechanical properties of apatites. Using ultrasonic

interferometer coupled with a solid media pressure apparatus, Katz and his co-worker [166] reported an elastic modulus of 114 GPa for polycrystalline hydroxyapatites, including mineral and synthetic. Silva et al. [167] summarized the mechanical properties of dense hydroxyapatite ceramics with Young's modulus in the range of 70-120 GPa. None of these investigations focused on the apatite layer formed on a bioglass surface. We studied localized mechanical behavior of the Ca-P precipitate layers formed on the surface of 45S5 bioglass in SBF, using the indentation technique. The Energy Dispersive X-ray analysis (EDS) is used to identify the precipitate phases in the Ca-P layers. Both the contact modulus and the indentation hardness of the Ca-P layers are determined as a function of the layer thickness; and the dependence of the contact modulus and the indentation hardness on the layer thickness is discussed.

7.2. Experimental

The samples were cut, grinded, and polished as the procedures described in Chapter 3. The polished samples then were heat-treated in air at 350ºC for 2 hours and furnace-cooled to room temperature to remove the residual stresses generated in the grinding and polishing.

The annealed, polished samples were immersed in a SBF solution of ~1 L , which was maintained at 37 °C to mimic the body temperature in an agitated water bath for 1, 2, 3, 5 or 7 days, respectively. The SBF solution was prepared by dissolving 5.403 g NaCl, 0.736 g $NaHCO_3$, 2.036 g Na_2CO_3, 0.225 g KCl, 0.182 g K_2HPO_4, 0.310 g $MgCl_2 \cdot 6H_2O$, 11.928 g 2-(4-(2-hydroxyethyl)-1-piperazinyl) ethane surfonic acid (HEPES), 0.293 g $CaCl_2$, 0.072 g Na_2SO_4 and 1.5 ml 1mol/L NaOH into double distilled water in sequence. HEPES and NaOH served as buffers to keep the pH value at 7.4. During the immersion, the SBF solution was in a stationary state; and there was no agitation in the SBF solution. Samples were immediately dried with compressed air and stored in a desiccator following the

immersion.

The immersed samples were divided into two groups, one for Scanning Electron Microscopy (SEM) and EDS and the other for microindentation. Microindentations were made on the Ca-P precipitate layers formed on the immersed samples, using a diamond Vickers indenter on a Micro-Combi Tester (CSM Instruments, Needham, MA). The peak indentation load applied to the indenter was in the range of 25 mN to 300 mN, and the loading rate and unloading rate were 200 mN/min with no holding time at the peak load. Arrays of indents were made with a minimum of 5 indents for each indentation load, and the spacing between two nearby indents was at least 3 times larger than the size of the indents. The indenttaion marks were measured using an optical microscope and a SEM. After the indentations, the specimens were immediately stored in a desiccator.

SEM with EDS capability was performed on a Hitachi S3200 instrument. The immersed samples were gold-palladium coated prior to SEM. All time-lapse SEM studies were performed on equivalent samples of bioglass. Samples were washed and dried, then kept in a desiccator in between characterization studies.

7.3. Results and Discussion

7.3.1 Growth of the Ca-P precipitate layers in SBF

Ca-P precipitates were present soon after the bioglass samples were immersed into the SBF solution. Figure 7.1 shows the typical surface topology of the polished bioglass before being placed in SBF. The bioglass samples had smooth surface. Figure 7.2 shows the typical surface topology of the Ca-P precipitate layers growing on the surface of the bioglass samples. After only one day's immersion, a thin Ca-P layer formed on the polished surface of the bioglass samples, while some deep scratches and micro-indents, which were made in purpose before the immersion, were still visible. After three days' immersion, the polished surface of the samples was fully covered by a homogeneous Ca-P layer, and all the scratches and indents

were invisible under SEM. After seven days' immersion, structure of double layers was observed. Random precipitates grew over the Ca-P layers.

All the Ca-P precipitate layers cracked into multiple pieces due to drying in the vacuum chamber of SEM. The crack size increased with the increase in the immersion time, which was a function of the thickness of the Ca-P precipitate layers. By titling the samples for 90 degree, the thickness of the Ca-P precipitate layers was measured. Figure 3 shows the dependence of the thickness of the Ca-P precipitate layers on the immersion time. For comparison, the results obtained by Prakash et al. [165] also are shown in Figure 7.3. Using a curve-fitting for the results from the present study and those from Prakash et al. [165], one can easily find that the thickness of the Ca-P precipitate layers is proportional to the square root of the immersion time. This is typical for the material growth controlled by diffusion and suggests that the growth of the Ca-P precipitate layers was controlled by the ions diffusion to the polished surface of the bioglass.

As pointed out by Prakash et al. [165], the Ca-P precipitation involves the dissolution of HPO_4^{2-} ions in SBF into PO_4^{3-} and the reaction of Ca^{2+} with PO_4^{3-} and OH^- to form $Ca_5(PO_4)_3(OH)$. Thus, the growth rate of the Ca-P precipitate layer depends on the diffusion of PO_4^{3-} and Ca^{2+} ions to the polished surface of the bioglass. In general, there is an excess amount of Ca^{2+} ions in SBF solution, the formation and growth of the Ca-P precipitate layer are determined by the concentration of PO_4^{3-}, which gradually decreases with time. Since there was no growth of the Ca-P layer on the periphery of the bioglass, it is believed that materials dissolution could occur from the periphery of the bioglass as suggested by Prakash et al. [165].

7.3.2 EDS characterization of the Ca-P precipitate layers

Generally, the bioactivity of a bioceramics is dependent on the formation ability

of hydroxyapatite (HA) on the surface of the bioceramics in a physiological environment. However, HA is not the only phase of Ca-P composition forming in a physiological environment [168], [169]. Actually, octacalcium phosphate (OCP), dicalcium phosphate (C_2P) and hydroxyapatite are all possible precipitates which could form in SBF.

The EDS analysis on the Ca-P precipitate layers were used to determine the change of the Ca/P ratio with the immersion time. Figure 7.4 shows the dependence of the Ca/P ratio in the Ca-P precipitate layers on the immersion time in SBF. The Ca/P ratio was about 1 for the immersion time of 0.5 and 1 day in SBF, suggesting the precipitation of C_2P (dicalcium phosphate). Then, the Ca/P ratio increased with increasing the immersion time and approached to a constant of 1.7 after 5 days' immersion, which is close to 1.67 for the stoichiometric HA [170]. HA layer formed on the surface of the bioglass after 5 days' immersion in SBF.

The variation of the Ca/P ratio with the immersion time suggests that the growth of the Ca-P precipitate layers started with a stage of high phosphate concentration before the formation of the HA layer or C_2P was the precursor for the growth of HA precipitates on 45S5 bioglass in SBF. According to Lu and Leng [171] in the analysis of the nucleation of Ca-P precipitates in SBF, the nucleation rate of OCP is substantially higher than that of HA, and HA is the most stable phase thermodynamically in SBF. C_2P precipitation is thermodynamically impossible in normal SBF, unless there are high concentrations of calcium and phosphate ions in SBF [171]. The dissolution of HPO_4^{2-} ions from the bioglass into PO_4^{3-} in SBF resulted in the increase of phosphate ions at the beginning of the immersion, which led to a thermodynamically unstable solution and the formation of C_2P precipitate layer. With the dissolution of HPO_4^{2-} ions into PO_4^{3-} being slowed down, the concentration of PO_4^{3-} decreased with time. The ratio of Ca/P in SBF increased due to an excess amount of Ca^{2+} ions in SBF, and HA began to form.

7.3.3 Indentation characteristics

The Ca-P precipitate layer, especially the HA layer, as a transition phase not only is essential for controlling the bioactivity of the bioglass but also plays an important role in bearing mechanical loading due to impact and wear. The mechanical behavior of the Ca-P precipitate layers determines the structural integrity of the implanted materials and the physiological realization and clinic performance of surgery.

The mechanical behavior of the Ca-P precipitate layers on 45S5 bioglass was studied by using the microindentation technique. The indentation tests were carried out using the load-control mode. Prior to a full indentation, a pre-load of 5 mN was applied to the indenter in order to maintain the contact between the indenter and the surface of samples and to avoid the effect of impact. Figure 7.5 shows typical loading-unloading curves for the indentations of the Ca-P precipitate layers, which were formed after 7 days' immersion in SBF. There exists slight difference in the loading curves for three different peak-indentation loads, which is likely due to the effects of local inhomogeneity. For the peak indentation load of 300 mN, the maximum indentation depth was less than 5 m. From Fig. 7.3, it is concluded that all the indentations did not penetrate over the interface between the Ca-P precipitate layer and the 45S5 biglass.

Figure 7.6a shows typical SEM micrograph of the surface morphology surrounding an indent made by an indentation load of 200 mN on a Ca-P precipitate layer, which was formed by immersing the 45S5 bioglass in SBF for 7 days. In contrast to the indentation on the 45S5 bioglass [94], [153], there are no cracks surrounding the indent. Local pile-up is visible around the indent. Figure 7.6b shows an array of indents on the same sample. The distance between the indents is at least three times of the indentation size. Numerous precipitates are observed on the surface of the Ca-P layer.

Using the SEM micrograph, one can measure the size of the indentations and calculate the indentation hardness, H, as

$$H = \frac{1.854F}{\bar{D}^2}$$

(7.1)

where F is the indentation load, and $\bar{D}$ is the average diagonal length of the indents. Figure 7.7 shows the dependence of the indentation hardness on the thickness of the Ca-P precipitate layers. The indentation hardness first decreased from the value of 7.0 GPa for the 45S5 bioglass to 0.28 GPa for the Ca-P layer of 7.51 m in thickness, then increased with the thickness to a value of 0.65 GPa for the Ca-P layer of 15.81 m in thickness, and finally decreased slightly with the increase in the thickness of the Ca-P precipitate layers. The results suggest that the indentation hardness of the 45S5 bioglass is much larger than those of the Ca-P precipitate layers.

According to Sargent [172], the indentation hardness of a film/substrate structure is determined by a weighted average of the volume of plastically deformed material in the film, V_f, and that in the substrate, V_s, as

$$H = \frac{H_f V_f + H_s V_s}{V_f + V_s}$$

(7.2)

Here, H_f and H_s are the indentation hardness of the film and substrate, respectively. In general, the size of plastic zone underneath indentation is about 1.5 to 2 times of the indentation depth. Thus, for a shallow indentation of a film/substrate structure with the indentation depth a few times less than the film thickness, the contribution of substrate to the indentation hardness of the film/substrate structure becomes negligible. As shown in Fig. 7.5, the maximum indentation depth was 4.83 m which is 4.8 times less than 23.1 m of the Ca-P layer thickness for the samples immersed in SBF for 7 days. The ratio of $V_s / (V_f + V_s)$ is approximately equal to zero. Therefore, the indentation hardness of 0.40 GPa can represent the indentation hardness of the HA layers formed on the 45S5 bioglass in SBF. The low indentation hardness of the HA layers likely is due to

the loose structure, as shown in Fig. 7.6a. There are numerous small cavities randomly distributing over the surface of the Ca-P layers, which has less resistance to the penetration of the indenter.

The contact modulus of the Ca-P precipitate layers can be calculated from the unloading curves and the size of indentations. The contact stiffness of S is first calculated by fitting the upper portion of the unloading curves, and the contact modulus of E_c is determined as

$$E_c = \frac{\sqrt{\pi}}{2\beta}\frac{S}{\sqrt{A_p}} \quad (7.3)$$

where A_p is the projected contact area, and β is a correction factor of 1.0124 for Vickers indenter [173].

Figure 7.8 shows the dependence of the contact modulus of the Ca-P precipitate layers on the Ca-P layer thickness. The contact modulus decreased from 36.0 GPa for the 45S5 bioglass to 5.7 GPa for the Ca-P precipitate layers of 13.0 m in thickness, then increased with the increase in the thickness of the Ca-P precipitate layers and became a constant of 12.0 GPa for the HA layers. The contact modulus of the Ca-P layers is less than the 45S5 bioglass. Assuming that the Poisson ratio of the 45S5 bioglass is in the range of 0.3 to 0.5, one can use the contact modulus to obtain the elastic modulus of the 45S5 bioglass as 27 to 32.8 GPa, which is in accord with the value of 30–35 GPa as determined by ASTM standard C623-71[94].

As a good first-order approximation, it has been suggested that the indentation depth needs to be less than 10% of the film thickness [174], [175] to avoid the substrate effect on the measurement of the contact modulus of film. For the indentations of the HA layers formed by immersing the samples in SBF for 7 days, the maximum indentation depth is 4.8 times less than the thickness of the HA layers. Thus, the 45S5 bioglass substrate has relatively negligible effect on the contact modulus of the HA layers measured from the indentations; and one can approximate 12.0 GPa as the contact modulus of the HA layer formed on the surface of the 45S5 bioglass in SBF.

Using the Poisson ratio of 0.3 to 0.5, the Young's modulus of the HA layers is found to be in the range of 9.0 to 10.9 GPa. The Young's modulus of the HA layers is much smaller than that of the sintered-formed HA (70-120 GPa [167], [1]), while it is very close to that of the cortical bone (7-30GPa [1]). Such a large difference in the Young's modulus is due to the difference in the microstructure of the HA. In contrast to the sintered-formed HA, the HA layer formed in SBF is loose structure consisting of spherical aggregates [176]. The loose structure with spherical aggregates causes the decrease in mechanical integrity of the 45S5 bioglass in physiological environment, while it promotes the ingrowth of natural bone.

7.4. Summary

The bioactivity of bioglasses depends on the growth of the Ca-P precipitate layer and the mechanochemical interaction in the human physiological solution. Using SEM, the growth behavior of the Ca-P precipitate layers on 45S5 bioglass in SBF was characterized. The thickness of the Ca-P precipitate layers increased with the immersion time and was proportional to the square root of the immersion time. This result suggested that the growth of the Ca-P precipitate layer on 45S5 bioglass in SBF was totally controlled by the diffusion of PO_4^{3-} and Ca^{2+} ions to the surface of the bioglass as expected. The Ca-P ratio in the Ca-P precipitate layers was identified by using EDS, which increased with the immersion time and approached a constant of 1.67 for stoichiometric HA. The results demonstrated that a hydroxyapaptite layer (Ca/P ratio of 1.67 by EDS) was formed after 5 days' immersion and a dicalcium phosphate (Ca/P ratio of 1.25 by EDS) was formed after 0.5-1 day's immersion.

Using the indentation technique, the localized deformation of the Ca-P precipitate layer on 45S5 bioglass was determined. The indentation hardness decreased from a value of 7.0 GPa for the 45S5 bioglass to 0.28 GPa for the Ca-P layer of 7.51μm in thickness, then increased with the thickness to a value of 0.65

GPa for the Ca-P layer of 15.81μm in thickness, and finally decreased with the increase in the thickness of the Ca-P precipitate layer. The indentation hardness of the HA layer formed in SBF was found to be 0.40 GPa. The contact modulus decreased from 36.0 GPa for the 45S5 bioglass to 5.7 GPa for the Ca-P precipitate layer of 13.0μm in thickness, then increased with the increase in the thickness of the Ca-P precipitate layer and became a constant of 12.0 GPa for the HA layer. The low indentation hardness and contact modulus of the Ca-P precipitate layers on the surface of the 45S5 bioglass was due to the formation of loose structure.

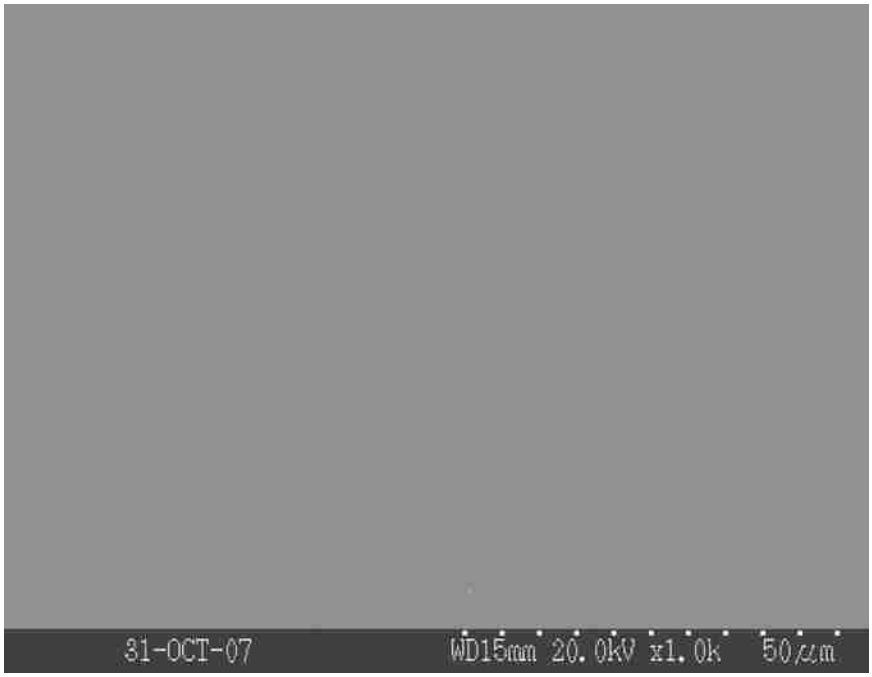

Figure 7.1. surface topology of the bioglass 45S5 samples before the SBF immersion.

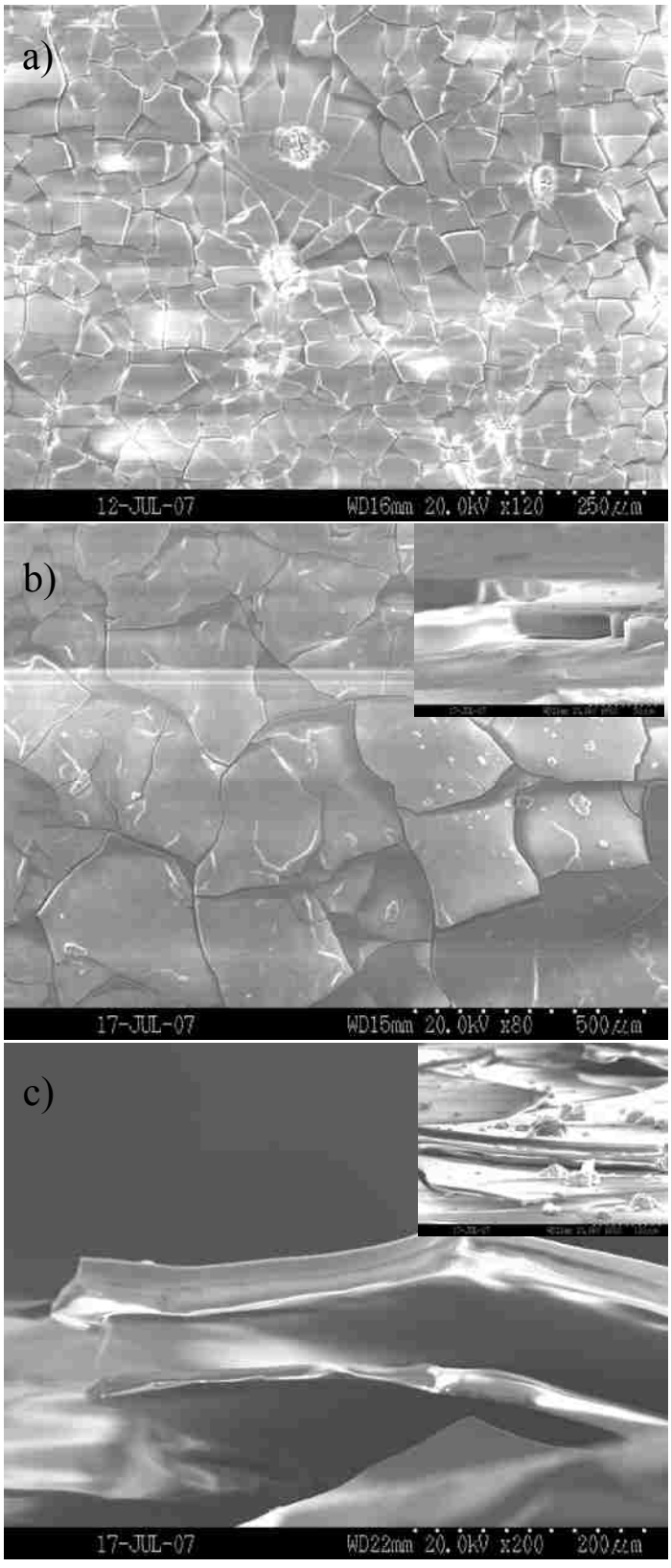

Figure 7.2. Evolution of surface topology of the Ca-P precipitate layers on the surface of the bioglass samples in SBF, (a) after 1 day's immersion; (c) after 3 days' immersion; (c) after 7 days' immersion.

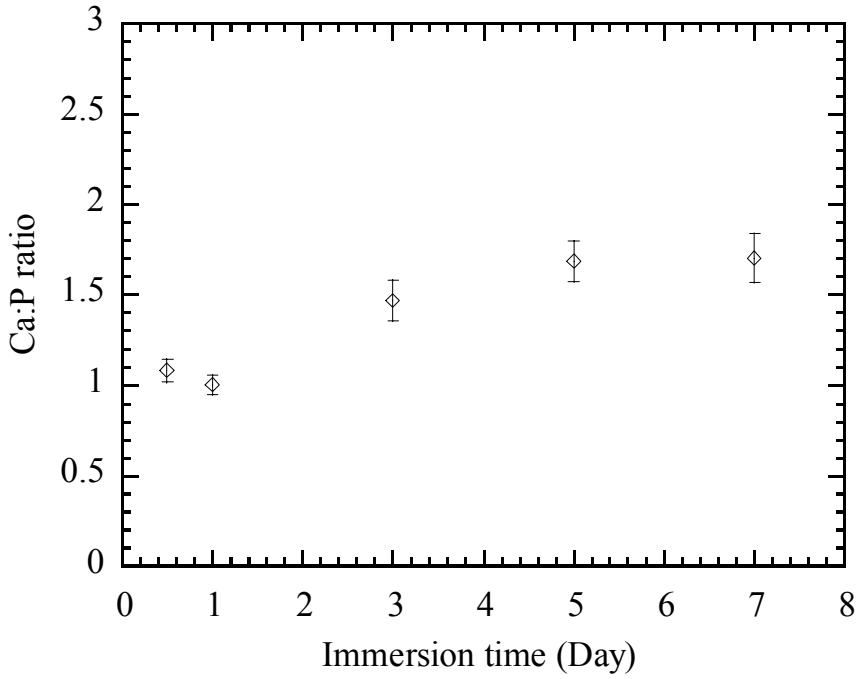

Figure 7.3. Variation of the Ca/P ratio in the Ca-P precipitate layers with immersion time

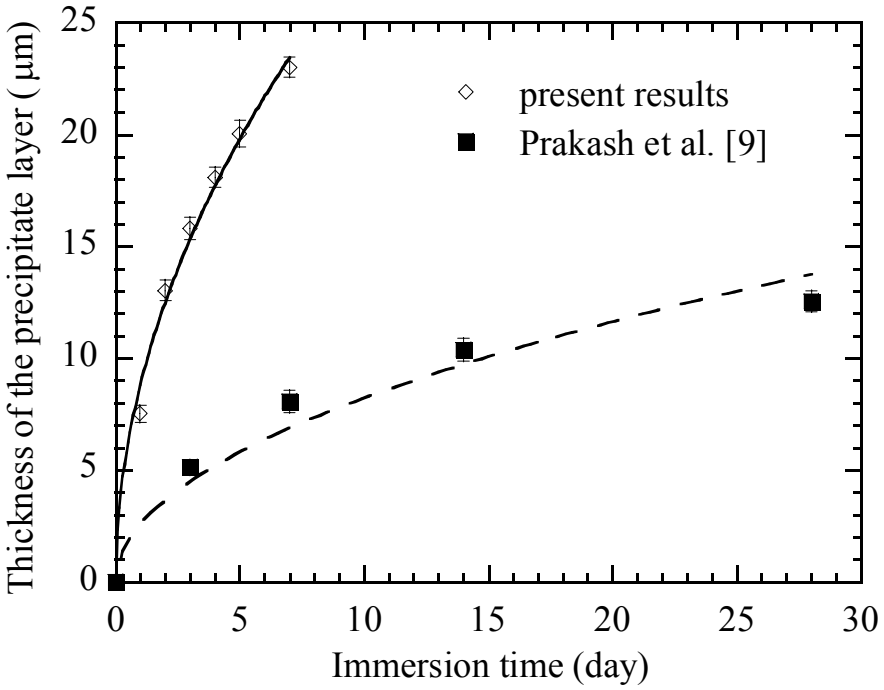

Figure 7.4. Variation of the thickness of the Ca-P precipitate layers with the immersion time in SBF. (The results from Prakash et al. [165] are the thickness of the apatite layerd formed on the composite disks with 40% hydroxyapatite (HA) in a PEEK matrix)

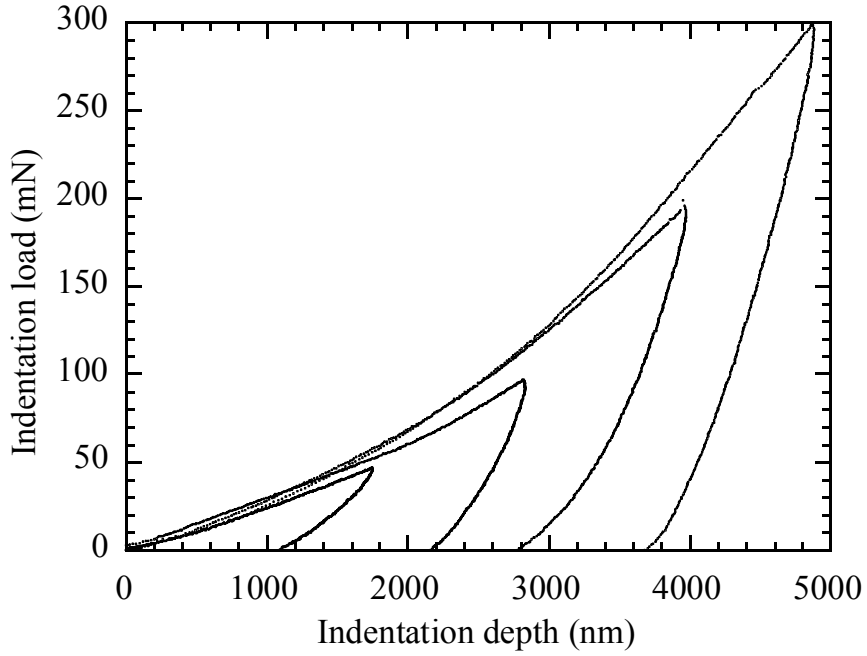

Figure 7.5. Typical loading-unloading curves for the indentation of a Ca-P precipitate layer formed by immersing a 45S5 bioglass in a SBF solution for 7 days

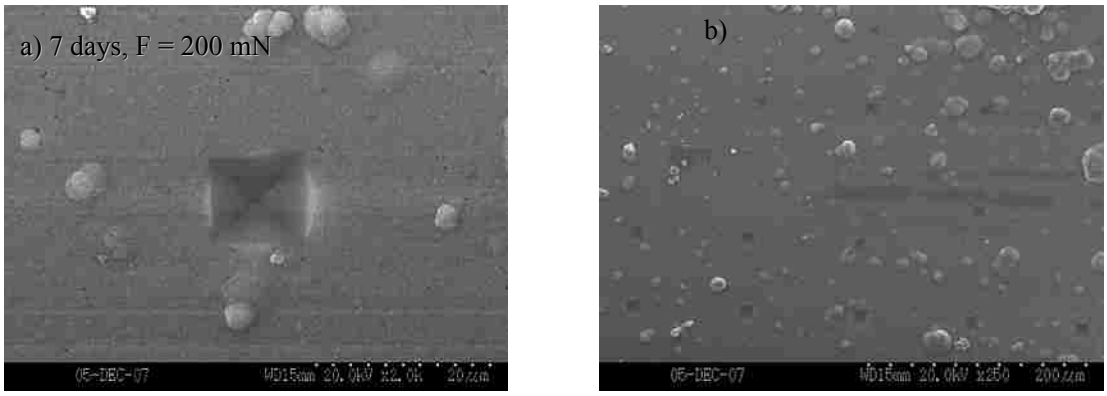

Figure 7.6. (a) SEM micrograph of the surface morphology surrounding an indent, and (b) SEM image of an array of indents. (The indented sample was immersed in SBF for 7 days. F is the peak indentation load.)

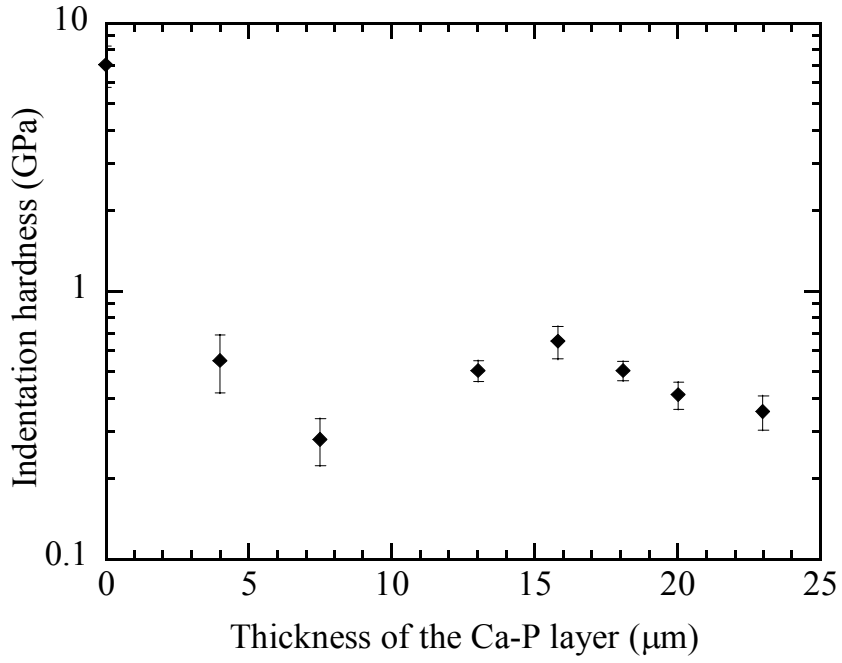

Figure 7.7. Dependence of the indentation hardness on the thickness of the Ca-P precipitate layers

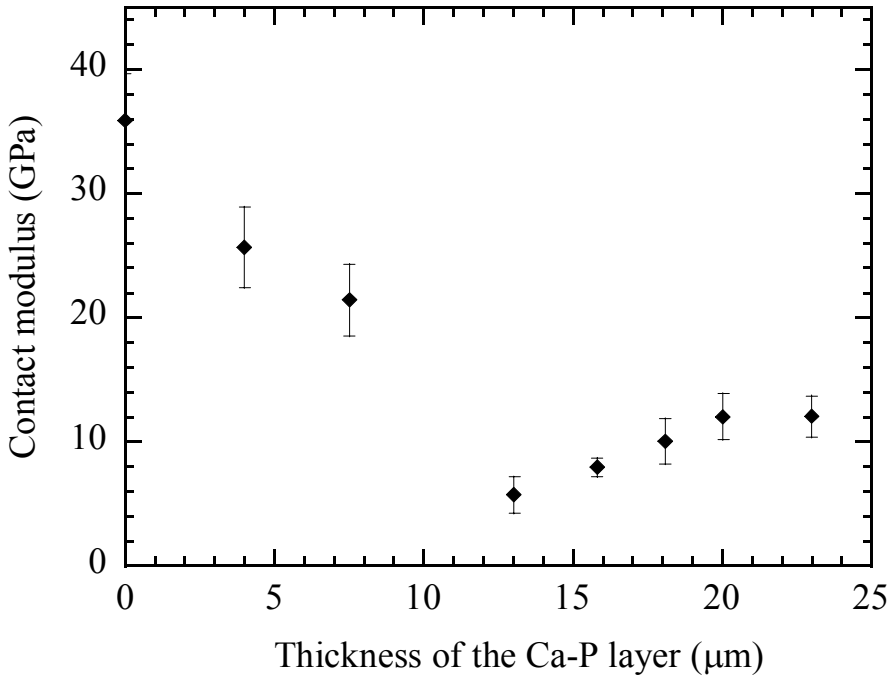

Figure 7.8. Dependence of the contact modulus on the thickness of the Ca-P precipitate layers

Chapter 8 Conclusion and Future work

8.1 Conclusion

The bioactivity of bioactive glass depends on the material microstructure and the mechanochemical interaction in the human physiological solution. Using the microindentation technique, the mechanical properties including the indentation hardness and fracture toughness of bioglass 45S5 were obtained both before and after being fully crystallized. The anelastic indentation recovery of the bioglass 45S5 was observed at room temperature from the depth recovery and the shrinking of the imprint marks.

To achieve the study goals, as an important gauge of the *in vitro* bioactivity of 45S5 bioglass, the surface dissolution of bioglass 45S5 in phosphate buffer solution (PBS) was characterized as a function of the indentation load by using a Vickers indenter. The surface morphology in the area surrounding micro-indents on the surface of the indented bioglass 45S5 is markedly different from that of the surface away from the indents after being immersed in PBS solution. The crack tips with tensile strain dissolved much faster than the stress-free surface. The crack tips blunt via dissolution with 1 day's immersion in PBS. The region under compression remained un-dissolved after 1 week's immersion in PBS due to strain relaxation of the undercutting of the indented region. If a bioactive glass were to have a residual compression in one area and zero compression or tension in another, a different rate of resorption could likely be realized in different areas resulting in different site-specific rates of cell proliferation and growth for integration. A paradox exists when attempting to increase the fracture toughness of bioactive glasses. Compressive surface strain certainly increases surface fracture toughness [177] but, as this work demonstrates, compressive strain alters the dissolution behavior of bioglass to make it less bioactive. Thus it is important to weigh the gains in mechanical properties with the loss in bioactivity by altering residual strain and stress states.

The local residual stress around an indent along the direction of 45 º to the

diagonal of the indents was quantified by the primary/secondary indents methods described in chapter 4. The surface around the indent was under a compressive stress state along the radial direction after the indentation. At fixed distance from the center of indents, the average local residual stress increased with the increase in the indentation load. At fixed maximum indentation load, the magnitude decreased with increasing distance away from the center of the indent. In the field far away from the indent center, the residual stress was approaching zero which indicated a stress-free state.

A spherical indenter was used to study the local deformation of 45S5 bioglass and also the behavior of the material dissolution around the indents. For the indents made with maximum indentation load larger than 1000 mN, radial cracks were created in addition to multi-ring cracks over the contact zone. For the indents made with maximum indentation load larger than 2000 mN, the indentation hardness gradually increased with the indentation load and reached a constant of 6.2 GPa. Fast dissolution occurred over the indentation-created damaged zone, including the edges of the cracks. Multiple small debris and ring-type grooves were observed; the depth and width of the grooves and cracks increased with the immersion time. A smooth surface surrounding the indents was formed over a long period of immersion, which was likely due to the confinement of material dissolution controlled by local compressive residual stress as observed from the Vickers indentation.

The mechanical properties of fully-crystallized bioglass 45S5 were also obtained by using Vickers indentation. An indentation hardness of 7.42±0.95 GPa was obtained, which is independent of the indentation load under the experimental conditions and the same as 7.47±0.51 GPa for the vitreous 45S5-bioglass. The average contact modulus was 12.14±1.15 GPa, about 3 times less than that for 45S5-bioglass in a vitreous state. The fracture toughness of the crystallized 45S5-bioglass was also about 3 times less than that of annealed 45S5-bioglass in vitreous state. Random surface dissolution was present with fast lateral dissolution rate over the undeformed surface. Surface precipitation occurred after four days' immersion, and a mineralized layer was formed over the entire surface of the

crystallized 45S5 bioglass after five days' immersion. There was a decrease in the calcium-phosphate ratio with immersion time. It is believed that a hydroxyapaptite layer (Ca/P ratio of 1.68 by EDS) was formed after seven-days' immersion and a dicalcium phosphate (Ca/P ratio of 1.25 by EDS) was formed after nine-days' immersion.

HA layers were observed on the surface of bioglass 45S5 after immersion in SBF. The thickness of the HA layers increased with the immersion time, following a parabolic relation. The contact elastic stiffness increases with the maximum indentation load in a linear relationship. There is a minimum modulus point when the immersion time was about 1 day and the thickness of HA was about 10 μm. When the time increased from 1 day to 7 days, the modulus increased and reached a maximum value of ~12.013GPa. When the immersion time increased from 0.5 day to 1 day, the modulus decreased with time. The Ca-P ratio reached about 1 when the immersion time was 1 day, which indicated the formation of C_2P and the Ca-P ratio reached 1.7 when the immersion time was 7 days, which indicated the formation of HA.

8.2 Future work

There is a substantial scope for carrying out further research that will extend the work presented in this dissertation.

The dissolution and precipitation behaviors of crystallized bioglass 45S5 in SBF have been studied. The grain boundary remained undissolved after 1 week's immersion which suggested that the region inside grains dissolved much faster. Also patterns which looked like orientated were observed on the "wall" of the undissolved grain boundary. TEM as a characterization technique is suggested to observe the orientation of the grain boundary surface in future studies. Chemical analysis, such as EDS or FTIR, needs be carried out to detect the mechanisms controlling the dissolution rates of grain boundaries and the grains. At the same time, the

mechanical properties of both grain boundaries and grains can be hardly characterized by micro-indentation due to the small size of the grains. Nano-indentation will be a good method to measure the mechanical performance instead.

The fracture toughness of the materials was greatly increased by being fully crystallized, however the dissolution performance of the materials were also hindered due to the presence of grain boundaries. In order to get a good balance between the fracture toughness and the biological performance of the glass-ceramic composites, the effects of crystallinity of bioglass on the mechanical properties and the *in vitro* behaviors can be detected by changing the crystallinity. The crystallinity can be controlled by the heat treatment parameters including temperature and time. The crystallinity can be characterized by the XRD technique. The further understanding of the importance of crystallinity of bioglass 45S5 is expected to contribute to the optimal design of the processing of implants made with bioactive glass.

Besides the dissolution of the bioactive glass, the formation of hydroxapatite layer is also an important factor to induce the ingrowth of natural bone in real applications. It was observed that the thickness of the hydroxapatite was varied with the stress distribution, immersion time and also the locations within the sample such as on the grain boundary or inside grains in fully crystallized glass-ceramic composites. Thus, the effect on the *in vitro* bioactivity response can be quantified by measuring the growth of the hydroxapatite layer thickness using Fourier transform infrared (FTIR) spectroscopy. The growth of the hydroxyapatite layer can be measured by the intensity of the P-O bonding peak which is near 602 or 575 cm^{-1} [28] related to that of the Si-O bonding peak (near 450 cm^{-1}). An Si-O to P-O peak ratio (Si:HA) less than 1 has been found to be associated with a well established HCA layer. Future studies should use this technique to correlate stress and crystallinity effects with HA layer formation, and in turn the effects of HA on later stages in the bioglass activity sequence.

Reference

1. Hench, L.L., *Bioceramics.* J. American Ceramic Society, 1998. **81**(8): p. 1705-28.
2. Hench, L.L., *Bonding Mechanisms at the Interface of Ceramic Prosthetic Materials.* J. Biomed. Mater. Res., 1971. **2**(1): p. 117-41.
3. Ogino, M., F. Ohuchi, and A.L.L. Hench, *Compositional Dependence of the Formation of Calcium Phosphate Films on Bioglass.* J. Biomed. Master. Res., 1980. **14**: p. 55-64.
4. Kim, H., *Ceramic Bioactivity and related biomimetic strategy.* Current Opinion in Solid State and Materials Science, 2003. **7**: p. 289-299.
5. Donald W. Turner , J.T.M., *Antigenicity of freeze-dried bone aIlograft in periodontal osseous defects.* Journal of Periodontal Research, 2006. **16**(1): p. 89 - 99.
6. Hamid Shegarfi, O.R., *Review article:Bone transplantation and immune response.* Journal of Orthopaedic Surgery, 2009. **17**(2): p. 206-11.
7. Hulbert, S.F., *Ceramics in Clinical Applications: Past, Present and Future.* High Tech Ceramics, 1987: p. 189-213.
8. Marta Cerruti, D.G., Kevin Powers, *Effect of pH and ionic strength on the reactivity of Bioglass® 45S5* Biomaterials, 2005. **26**(14): p. 1665-1674.
9. M. M. Pereira, A.E.C., and L. L. Hench, *Calcium phosphate formation on sol-gel-derived bioactive glass in vitro.* J. Biomed. Mater.Res., 1994. **28**: p. 693-698.
10. Qing Jie, K., Jiping Zhong, Yifengshi, Qin Li, Jiangchang, and Ruoding Wang, *Preparation of Maroporous Sol-Gel Bioglass Using PVA particles as pore former.* Journal of Sol-Gel Science and Technology, 2004. **30**: p. 49-61.
11. Cluppera, D.C., *Bioactivity of tape cast and sintered bioactive glass-ceramic in simulated body fluid.* Biomaterials, 2002. **23**: p. 2599-2606.
12. Xin, R., *A comparative study of calcium phosphate formation on bioceramics in vitro and in vivo.* Biomaterials, 2005. **26**: p. 6477-6486.
13. Arita, I.H., Wilkinson, D. S., Mondragen, M. A., Castano, V. M., *Chemistry and sintering behavior of thin hydroxyapatite ceramics with controlled porosity.* Biomaterials, 1995. **16**: p. 403-408.
14. TB, L., *Clinical evaluation of bioactive glass in the treatment of periodontal osseous defects in humans.* J. Periodontol, 1998. **69**: p. 1027-35.
15. Roncari, E., Galassi, C., *Tape casting of porous hydroxyapatite ceramics.* J. Master. Sci. Letters, 2000. **19**: p. 33-35.
16. Suominen EA., A.A., Juhanoja J., Yli-Urpo A., *Hydroxyapatite-glass composite as a bone substitute in large metaphyseal cavities in rabbits.* Int Orthop, 1995. **19**: p. 167-73.
17. Li P, Y.Q., Zhang F, and Kokubo T., *The effect of residual glassy phase in a bioactive glass-ceramic on the formation on its surface apatite layer in vitro.* J. Master Sci: Mater Med, 1992. **3**: p. 452-6.
18. Hench, L.L., D.L. Wheeler,D.C. Greenspan, *Molecular Control of Bioactivity*

in Sol-Gel Glasses. Journal of Sol-Gel Science and Technology, 1998. **13**: p. 245.
19. J.R. Jones, L.L.H., *Materials perspective Biomedical materials for new millennium: perspective on the future.* Materials Science and Technology, 2001. **17**: p. 891.
20. Hench, J.R.J.a.L.L., *Materials perspective Biomedical materials for new millennium: perspective on the future.* Materials Science and Technology, 2001. **17**: p. 891.
21. L. Palacio, P.P., J.I. Calvo, A. Hernandez, *Porosity measurements by a gas penetration method and other techniques applied to membrane characterization.* Thin Solid Films, 1999. **348**: p. 22-29.
22. Abell A.B., W.K.L., Lange D.A., *Mercury Intrusion Porosimetry and Image Analysis of Cement-Based Materials.* Journal of Colloid and Interface Science, 1999. **211**(6): p. 39-44.
23. R.C. Atwood, J.R.J., P.D. Lee, L.L. Hench, *Analysis of pore interconnectivity in bioactive glass foams using X-ray microtomography.* Scripta Materialia, 2004. **51**: p. 1029–1033.
24. Ibanez L, S.W., Ng L, Cates J., *The ITK software guide.* Clifton Park, NY, USA: Kitware Inc, 2003: p. 330-303.
25. Gonzalez R, W.R., *Digital Image Processing.* Reading MA, USA: Addison Wesley, 1992: p. 518–524.
26. Brunauer, S., *Physical Adsorption.* Princeton University Press, Princeton, N. J., 1945.
27. Somorjai, G.A., *Principles of Surface Chemistry.* Prentice-Hall, Englewood Cliffs, N. J., 1972.
28. A. Jena, K.G., *Characterization of Pore Structure of Filtration Media.* Fluid particle Separation Journal, 2002. **14**(3): p. 227-241.
29. Laleh Safinia, A.M., and Alexander Bismarck, *Nondestructive Technique for the Characterization of the Pore Size Distribution of Soft Porous Constructs for Tissue Engineering.* Langmuir, 2006. **22**: p. 3235-3242.
30. Boussu K, V.d.B.B., Volodin A, Snauwaert J, Van Haesendonck C, Vandecasteele C, *Roughness and hydrophobicity studies of nanofiltration membranes using different modes of AFM.* J Colloid Interface Sci., 2005. **286**(2): p. 632-8.
31. Binks, B.P., *Modern Characterization Methods of Surfactant Systems.* Surfactant science series, 1996. **86**.
32. Bollen CML, L.P., Quirynen M., *Comparison of surface roughness of oral hard materials to the threshold surface roughness for bacterial plaque retention: a review of the literature.* Dent Mater, 1997. **13**: p. 258-269.
33. X. Dai, Y.C.C., and A. C. K. So, *Digital Speckle Correlation Method Based on Wavelet-Packet Noise-Reduction Processing.* Appl. Opt, 1999. **38**: p. 3474-3482.
34. F Luk, V.H.a.W.N., *Measurement of surface roughness by a machine vision system.* J. Phys. E: Sci. Instrum, 1989. **22**: p. 977-980.

35. Park, R.G.C.a.J.G., *Measurement of electrical resistivity by a mutual inductance method.* Br. J. Appl. Phys., 1961. **12**: p. 507-510.
36. Adler RS, D.D., Laing TJ, Chiang EH, Meyer CR, Bland PH, Rubin JM., *Quantitative assessment of cartilage surface roughness in osteoarthritis using high frequency ultrasound.* Ultrasound Med Biol., 1992. **18**(1): p. 51-8.
37. Itaelae, A.A., Hannu; Hupa, Mikko; Nordstroem, Egon; Ylaenen, Heimo, *A method for etching the surface of a bioactive glass.* PCT Int. Appl., 2001. **21**: p. WO0166479.
38. Ana C. Queiroz, J.D.S., Rui Vilar, Sonia Eugenio, Fernando J. Monteiro, *Laser surface modification of hydroxyapatite and glass-reinforced hydroxyapatite.* Biomaterials, 2004. **25**: p. 4607–4614.
39. Varshneya, A.K., *Fundamentals of Inorganic Glasses.* Academic Press, 1994.
40. H.A. Tsai, Y.S.C., C.C. Hu, K.R. Lee, D.G. Yu, J.Y. Lai, *Heat-treatment effect on the morphology and pervaporation performances of asymmetric PAN hollow fiber membranes.* Journal of Membrane Science, 2005. **255**: p. 33–47.
41. Kongbo, R.K.K.T., *Method for heat treatment of aluminum alloy sheets to reduce the surface roughness.* 2003: p. KR2003090047.
42. Jalal Barzin, C.F., K. C. Khulbe, T. Matsuura, S. S. Madaeni and H. Mirzadeh, *Characterization of polyethersulfone hemodialysis membrane by ultrafiltration and atomic force microscopy.* Journal of Membrane Science, 2004. **237**(1-2): p. 77-85.
43. Rabi Rabady, D.F., and Ivan Avrutsky, *Heat treatment for reduction of surface roughness on holographic gratings.* Optics Letters, 2003. **28**(18): p. 1665-67.
44. S.J. Li, M.N., T. Akahori, T. Kasuga, R. Yang ,Y.L. Hao, *Fatigue characteristics of bioactive glass-ceramic-coated Ti–2**9Nb–13Ta–4.6Zr f**or biomedical **application**.* Biomaterials, 2003. **25**(17): p. 3369-3378
45. R.L.Reis, F.J.M., G.W.Hastings, *Stability of hydroxylapatite plasma Sprayed coated Ti-6Al-4V under cyclic bending in simulated physiological solution.* J. Mater. Sci.: Mater. Med., 1994. **5**: p. 457-462.
46. Sergo V., S.O., Clarke DR., *Mechanical and chemical consequences of the residual stresses in plasma sprayed hydroxyapatite coatings.* Biomaterials, 1997. **18**(6): p. 477-82.
47. Siiriäinen, J., *Measurement of Residual Stresses - Design and Implementation of Ring-Core Method*. TKK-MTR. Vol. TKK-MTR-4/99. 1999, Espoo: Helsinki University of Technology Laboratory of Materials Engineering.
48. Meyers, C., *Mechanical Behavior of Materials.* 1999: p. 162–168.
49. Tabor, D., *The Hardness of Metals.* 2000.
50. R.L. Smith , G.E.S., *An Accurate Method of Determining the Hardness of Metals, with Particular Reference to Those of a High Degree of Hardness.* Proceedings of the Institution of Mechanical Engineers, 1922. **I**: p. 623-641.
51. Ki Myung Lee, C.-D.Y., Andreas A. Polycarpou *Relationship between scratch hardness and yield strength of elastic perfectly plastic materials using finite element analysis.* Journal of Materials Research, 2008. **23**(8): p.

2229-2237
52. http://www.ukcalibrations.co.uk/vickers_htm.html.
53. Eduard Kimmari, L.K., *Application of the continuous indentation test method for the characterization of mechanical properties of B4C/Al composites.* Proc. Estonian Acad. Sci. Eng., 2006. **12**(4): p. 399–407.
54. J. L. He , V.S., *Finite element modeling of indentation into superhard coating.* Surf Coat Tech., 2003: p. 163-164, 374-379.
55. Franco A. R., P.G., Sinatora A., Pinedo C. E., Tschiptschin A. P., *The use of a Vickers indenter in depth sensing indentation for measuring elastic modulus and Vickers hardness.* J. Mater. Res., 2004. **7**: p. 483–491.
56. Chantikul, P., *A Critical Evaluation of Indentation Techniques for Measuring Fracture Toughness: II, Strength Method.* J. Am. Ceram. Soc., 1981. **64**(9): p. 539-543.
57. Evans, A.G.a.C., E.A., *Fracture Toughness Determinations by Indentation.* J. Amer. Ceram. Soc., 1976. **59**(7-8): p. 371-372.
58. Evans, A.G.a.C., E.A. *Fracture toughness: the role of indentation techniques*. in *American Society for Testing and Materials*. 1979. Philadelphia: Freiman,S.W.
59. Lawn, B.R., *Fracture of Brittle Solids*. 2nd ed. 1993, Cambridge: Press Syndicate of the University of Cambridge.
60. Lawn, B.R., Evans, A.G., Marshall, D.B., *Elastic/Plastic Indentation Damage in Ceramics: The Median/Radial Crack System.* J. Amer. Ceram. Soc., 1980. **63**(9-10): p. 574-581.
61. Anstis, G.R., *A Critical Evaluation of Indentation Techniques for Measuring Fracture Toughness: I, Direct Crack Measurements.* J. Am. Ceram. Soc., 1981. **64**(9): p. 533-538.
62. Gogotsi, G.A., *Deformational behaviour of ceramics.* Journal of the European Ceramic Society, 1991. **7**(2): p. 87-92.
63. M.R. Berrahmoune, S.B., K. Inal and E. Patoor, *Delayed cracking in 301LN austenitic steel after deep drawing: Martensitic transformation and residual stress analysis.* Materials Science and Engineering: A, 2006. **438-440**: p. 262-266.
64. Macherauch E., H.V., *Residual stresses in science and technology.* DGM, 1986.
65. Yaser M. Alkhiary, S.M.M.a.R.A.G., *Effects of acid hydrolysis and mechanical polishing on surface residual stresses of low-fusing dental ceramics.* The Journal of Prosthetic Dentistry, 2003. **90**(2): p. 133-142.
66. Burak Taskonak, J.J.M.J., Kenneth J. Anusavice, *Residual stresses in bilayer dental ceramics.* Biomaterials, 2005: p. 3235–3241.
67. Lawn, B., *Fracture of Brittle Solids-Second Edition.* 1975: p. 257.
68. Jr., M.J., *Fractography of glasses and ceramics", Proceedings of the conference on the fractography of glasses and ceramics* American Ceramic Society, 1991: p. 413–51.
69. JJ., M.J., *Quantitative fractographic analysis of fracture origins in glass.*

Plenum Press, 1994: p. 39-73.
70. Conway Jr. JC, M.J., JJ., *Use of crack branching data for measuring near-surface residual stresses in tempered glass.* J Am. Ceram Soc., 1989. **72**(9): p. 1584–7.
71. Tancred, D.C., Carr, A.J. and McCormack, B.A.O., *The sintering and mechanical behavior of hydroxyapatite with bioglass additions.* J. Mat. Sci.-Mat. Med., 2001. **12**(1): p. 81-93.
72. Reis, R.L., Monteiro, F.J. and Hastings, G.W., *Stability of Hydroxylapatite Plasma-Sprayed Coated Ti-6al-4v under Cyclic Bending in Simulated Physiological Solutions.* J. Mat. Sci.-Mat. Med., 1994. **5**(6-7): p. 457-462.
73. Maxian SH, Z.J., Dunn MG., *Mechanical and histological evaluation of amorphous calcium phosphate and poorly crystallized hydroxyapatite coatings on titanium implants.* J Biomed Mater Res, 1993. **27**(7): p. 17-28.
74. De Bruijn JD, B.Y., van Blitterswijk CA, *Structural arrangements at the interface between plasma sprayed calcium phosphates and bone.* Biomaterials, 1994. **15**(54): p. 3-50.
75. Oscar Peitl Filho, G.P.L.T., Larry L. Hench, *Effect of crystallization on apatite-layer formation of bioactive glass 45S5.* Journal of Biomedical Materials Research, 1998. **30**(4): p. 509 – 514.
76. Taylor LS, Z.G., *The quantitative analysis of crystallinity using FT-Raman spectroscopy.* Pharm Res., 1998. **15**: p. 755-761.
77. Jalsovszky G, E.O., Holly S, Hegedus B., *Investigation of the morphological composition of cimetidine by FT-Raman spectroscopy.* Appl Spectrosc, 1995. **49**: p. 1142-1145.
78. Forbes RA, M.B., Smith DR., *Measurement of residual isopropyl alcohol in loracarbef by near-infrared reflectance spectroscopy.* Anal Chem., 1999. **71**: p. 1232-1239.
79. Andersen KV, B.H., Jakobsen HJ., *Determination of enantiomeric purity from solid-state 31P MAS NMR of organophosphorus compounds.* Magn Reson Chem., 1990. **28**: p. S47-S51.
80. Kamat MS, O.T., DeAngelis RJ, Koyama Y, Deluca PP., *Estimation of the degree of crystallinity of cefazolin sodium by X-ray and infrared methods.* Pharm Res., 1988. **5**: p. 426-429.
81. Otsuka M, K.N., *A kinetic study of the crystallization process of non-crystalline indomethacin under isothermal conditions.* Chem Pharm Bull (Tokyo), 1988. **36**: p. 4026-4032.
82. Xiaohong Pan, T.J., and Larry Augsburger, *Quantitative Measurement of Indomethacin Crystallinity in Indomethacin-Silica Gel Binary System Using Differential Scanning Calorimetry and X-ray Powder Diffractometry.* AAPS PharmSciTech, 2006. **7**(1): p. 11.
83. Park A, C.L., *In vitro cell response to differences in poly-lactide crystallinity.* J Biomed Mater Res., 1996. **31**: p. 117-130.
84. Liggins RT, B.H., *Paclitaxel-loaded poly(L-lactic acid) microspheres. 3. Blending low and high molecular weight polymers to control morphology*

and drug release. Int J Pharm., 2004. **282**: p. 61-71.
85. S. Widjaja, T.H.Y., A.M. Limarga, *Measurement of creep-induced localized residual stress in soda-lime glass using nano-indentation technique.* Materials Science and Engineering: A, 2001. **318**: p. 211–215.
86. D. K. Sheity, A.R.R., W. H. Duckworth, *Indenter Flaw Geometry and Fracture Toughness Estimates for a Glass-Ceramic.* J. Am. Ceram. Soc., 1985. **68**(10): p. 282-284.
87. A. G. Evans , E.A.C., *Fracture Toughness Determinations by Indentation.* J. Am. Ceram. SOC., 1976. **56**(7): p. 371-72.
88. Mark V. Thomas, D.A.P., Mobanad Al-Sabbaagh, *Bioactive Glass Three Decades On.* Journal of Long-Term Effects of Medical Implants, 2005. **15**(6): p. 285-297.
89. Itala A , N.E., Ylanen H, Aro HT, Hupa M., *Creation of microrough surface on sintered bioactive glass microspheres.* J Biomed Mat Res, 2001. **56**(2): p. 282-288.
90. T. Saito, H.H., K. Uoe, T. Kizuki, K. Teraoka, K. Kato, Y. Yokogawa., *Calcium Phosphate Nano-Composite with Bone Morphogenetic Protein.* Key Engineering Materials, 2005. **330-332**: p. 284-286.
91. Mietek Jaroniec, M.K., James P. Olivier,, *Standard Nitrogen Adsorption Data for Characterization of Nanoporous Silicas.* Langmuir, 1999. **15**: p. 5410-5413.
92. P. Lodewyckx, C.I., S. Blacher, A. Léonard, *Use of x-ray microtomography to visualise dynamic adsorption of organic vapour and water vapour on activated carbon*

Adsorption, 2006. **12**(1): p. 0929-5607.
93. Holland, B., *Determination of Both Mesopores and Macropores in Three-Dimensional Ordered Porous Materials by Nitrogen Adsorption.* Journal of Porous Materials, 2004. **10**(1): p. 1380-2224.
94. D. Li, F.Q.Y., J. Nychka, *Indentation-induced residual stresses in 45S5 bioglass and the stress effect on the material dissolution.* Eng. Fract. Mech., 2008. **75**: p. 4898–4908.
95. D. Li, M.M.X.Y., P. Muralidhar, C. Wu, F.Q. Yang, *Local surface damage and material dissolution in 45S5 bioactive glass: Effect of the contact deformation.* J. Non-Crystalline Solids.
96. Washburn, J., *Experimental observations concerning the collapse of dislocation loops during annealing.* J. Metals, 1956. **8**: p. 189-191.
97. B.T.A. Chang, J.C.M.L., *Indentation recovery of amorphous materials.* Scripta Metall., 1979. **13**: p. 51-54.
98. G.A. Shaw, D.S.S., A.D. Johnson, A.B. Ellis, W.C. Crone, *Shape memory effect in nanoindentation of nickel-titanium thin films.* Appl. Phys. Lett., 2003. **83**: p. 257-259.
99. B.T.A. Chang, J.C.M.L., *Indentation recovery of amorphous materials.* Scripta Metall, 1979. **13**: p. 51-54.
100. Y.J. Zhang, Y.T.C., D.S. Grummon, *Shape memory surfaces.* Appl. Phys.

Lett., 2006. **89**: p. 041912.
101. F.Q. Yang, J.C.M.L., *Impression recovery of PMMA.* J. Mater. Res., 1997. **12**: p. 2809-2814.
102. B.T.A. Chang, J.C.M.L., *Indentation recovery of atactic polystyrene.* J. Mater. Sci.: Mater. Med., 1980. **15**: p. 1364-1370.
103. F.Q. Yang, S.L.Z., J.C.M. Li, *Impression recovery of amorphous polymers.* J. Electron. Mater., 1997. **26**: p. 859-862.
104. C.A. Tweedie, K.J.V.V., *On the indentation recovery and fleeting hardness of polymers.* J. Mater. Res., 2006. **21**: p. 3029-3036.
105. N.M. Everitt, S.R., D.S. McNally, *Bone recovery following micro-indentation.* J. Bone Joint Surg. Br., 2006. **88**(B): p. 398.
106. R. Chen, F.Q.Y., P.K. Liaw, G.J. Fan, H. Choo, *Microindentation of a Zr57Ti5Cu20Ni8Al10 bulk metallic glass.* Mater. Trans., 2007. **48**: p. 1743-1747.
107. F.Q. Yang, L.L.P., K. Okazaki, *Microindentation of aluminum.* Metall. Mater. Trans. A 2004. **35**: p. 3323-3328.
108. Ning, A.E.-G.a.C.Q., *Effect of bioactive ceramic dissolution on the mechanism of bone mineralization and guided tissue growth in vitro.* J. Biomed. Mat. Res., 2006. **76**: p. 386.
109. A. El-Ghannam, P.D.a.I.M.S., *Bioactive Glass Stimulates the Function of Biological Signaling Molecules and Cells.* J. Ortho. Res. Vol, 1999. **17**: p. 340.
110. H.H. Lu, S.R.P., P. Ducheyne, *45S5 Bioactive glass surface charge variations and the formation of a surface calcium phosphate layer in a solution containing fibronectin.* J. Biomed. Mat. Res., 2000. **51**: p. 80.
111. J.R. Jones, P.S., L.L. Hench, *Dose-dependent behavior of bioactive glass dissolution.* J. Biomed. Mat. Res., 2001. **58**: p. 720.
112. E.A.B. Effah Kaufmann, P.D., S. Radin, B. D.A. , R. Composto, J. Biomed. Mat.
Res., 2000. **52**: p. 825.
113. S. Radin, P.D., B. Rothman , A. Conti, J. Biomed. Mat. Res., 1997. **37**: p. 363.
114. O.P. Filho, G.P.L.T., L.L. Hench, J. Biomed. Mat. Res., 1996. **30**: p. 509.
115. A. El-Ghannam, E.H., A. Yehia, J. Biomed. Mat. Res., 2001. **55**: p. 387.
116. D.F. Averette , M.M., J. Dent. Res., 1983. **62**: p. 842.
117. N.E. Esipova, A.I.E., A.I. Rusanov, Glass Phys. Chem., 2006. **32**: p. 267.
118. S.V. Hainsworth , T.F.P., J. Mater. Sci.: Mater. Med., 1994. **29**: p. 5529.
119. S.W. Youn, C.G.K., Mater. Sci. Eng. A, 2004. **384**: p. 275.
120. V. Sergo, O.S., D.R. Clarke, Biomaterials, 1997. **18**: p. 477.
121. Lawn, B.R., *Fracture of Brittle Solids*. Second Ed. ed. Cambridge Solid State Science Series, ed. E.A. Davis and I.M. Ward. 1993, Cambridge: Press Syndicate of the University of Cambridge. 378.
122. Evans, A.G., *Fracture toughness: the role of indentation techniques*, in *Fracture mechanics applied to brittle materials*, S.W. Freiman, Editor. 1979,

American Society for Testing and Materials: Philadelphia. p. 112-135.
123. Evans, A.G. and E.A. Charles, *Fracture Toughness Determinations by Indentation.* Journal of the American Ceramic Society, 1976. **59**(7-8): p. 371-372.
124. Lawn, B.R., A.G. Evans, and D.B. Marshall, *Elastic/Plastic Indentation Damage in Ceramics: The Median/Radial Crack System.* Journal of the American Ceramic Society, 1980. **63**(9-10): p. 574-581.
125. Anstis, G.R., et al., *A Critical Evaluation of Indentation Techniques for Measuring Fracture Toughness: 1, Direct Crack Measurements.* Journal of the American Ceramic Society, 1981. **64**(9): p. 533-538.
126. Shetty, D.K., A.R. Rosenfield, and W.H. Duckworth, *Indenter Flaw Geometry and Fracture-Toughness Estimates for a Glass-Ceramic.* Journal of the American Ceramic Society, 1985. **68**(10): p. C282-C284.
127. Day, T., *Mechanical Properties of MO-SCI Bioactive Glass 45S5*, J.A. Nychka, Editor. 2007: Lexington.
128. Bowden, M. and D. Gardiner, *Stress and Structural Images of Microindented Silicon by Raman Microscopy.* Applied Spectroscopy, 1997. **51**(9): p. 1405-1409.
129. Kim, J.J., et al., *Nanocrystallization during nanoindentation of a bulk amorphous metal alloy at room temperature.* Science, 2002. **295**(5555): p. 654-657.
130. Chen, R., et al., *Hardness variation across a Zr57Ti5Cu20Ni8Al10 bulk metallic glass.* Journal of Materials Science, 2007. **42**(6): p. 2208-2211.
131. Yang, F.Q., J.A. Nychka, and P. Liaw, *Compression testing of bulk metallic glass: deformation behavior and shear band formation*. 2006, University of Kentucky, University of Tennessee.
132. Clupper, D.C. and L.L. Hench, *Crystallization kinetics of tape cast bioactive glass 45S5.* Journal of Non-Crystalline Solids, 2003. **318**(1-2): p. 43-48.
133. Sergo, V., O. Sbaizero, and D.R. Clarke, *Mechanical and chemical consequences of the residual stresses in plasma sprayed hydroxyapatite coatings.* Biomaterials, 1997. **18**(6): p. 477-482.
134. Reis, R.L., F.J. Monteiro, and G.W. Hastings, *Stability of Hydroxylapatite Plasma-Sprayed Coated Ti-6al-4v under Cyclic Bending in Simulated Physiological Solutions.* Journal of Materials Science-Materials in Medicine, 1994. **5**(6-7): p. 457-462.
135. Filho, O.P., G.P. La Torre, and L.L. Hench, *Effect of crystallization on apatite-layer formation of bioactive glass 45S5.* Journal of Biomedical Materials Research, 1996. **30**(4): p. 509-514.
136. Evans AG., C.E., *Fracture toughness determinations by indentation.* J Am Ceram Soc., 1976. **59**(7-8): p. 371-372.
137. Anstis GR., C.P., Lawn BR,Marshall DB, *A critical evaluation of indentation techniques for measuring fracture toughness: 1, direct crack measurements.* J Am Ceram Soc., 1981. **64**(9): p. 533-538.
138. Chantikul P., L.B., Marshall DB., *Micromechanics of flaw growth in static*

fatigue - influence of residual contact stresses. J Am Ceram Soc., 1981. **64**(6): p. 322-325.
139. Zhang TY., C.L., Fu R., *Measurements of residual stresses in thin films deposited on silicon wafers by indentation fracture.* Acta Mater., 1999. **47**(14): p. 3869-3878.
140. Zeng KY. , R.D., *Experimental measurement of residual stress field around a sharp indentation in glass.* J Am Ceram Soc., 1994. **77**(2): p. 524-530.
141. Chiang SS. , M.D., Evans AG., *The response of solids to elastic plastic indentation .1. stresses and residual-stresses.* J Appl Phys., 1982. **53**(1): p. 298-311.
142. Reis RL., M.F., Hastings GW., *Stability of hydroxylapatite plasma-sprayed coated Ti-6al-4v under cyclic bending in simulated physiological solutions.* J Mater Sci Mater Med., 1994. **5**(6-7): p. 457-462.
143. H., E., *Viscosity, plasticity, and diffusion as examples of absolute reaction rates.* J Chem Phys., 1936. **4**(10): p. 283-291.
144. FQ, Y., *Interaction between diffusion and chemical stresses.* Mater Sci Eng A., 2005. **409**(1-2): p. 153-159.
145. B.R. Lawn, A.G.E., D.B. Marshall, *Elastic/plastic indentation damage in ceramics: The median/radial crack system.* J. Am. Ceram. Soc., 1980. **63**: p. 574-581.
146. S. Dériano, A.J., T. Rouxel, J.-C. Sangleboeuf, S. Hampshire, *The indentation fracture toughness (Kc) and its parameters: the case of silica-rich glasses.* J. Non-Crystal. Solids, 2004. **344**: p. 44-55.
147. F.Q. Yang, W.W.D., K. Okazaki, *Effect of cold rolling on the indentation deformation of AA 6061 aluminum alloy.* J. Mater. Res., 2005. **20**: p. 1172-1179.
148. Green, D.J., *An introduction to the mechanical properties of ceramics*. 1998: Cambridge University Press. 264.
149. Charles, R.J., *Dynamic fatigue of glass.* J. Appl. Phys., 1958. **29**: p. 1651-1657.
150. Eyring, H., *Viscosity, plasticity, and diffusion as examples of absolute reaction rates.* J. Chem. Phys., 1936. **4**: p. 283-291.
151. V. Sergo, O.S., D.R. Clarke, *Mechanical and chemical consequences of the residual stresses in plasma sprayed hydroxyapatite coatings.* Biomaterials, 1997. **18**: p. 477-482.
152. J.-C. Pollet, S.J.B., *Thermally activated crack propagation – theory.* Int. J. Fract., 1977. **13**: p. 667-679.
153. D. Li, M.X.Y., P. Muralidhar, C. Wu, F. Q. Yang, *Local surface damage and material dissolution in 45S5 bioactive glass: Effect of the contact deformation.* J. Non-Cryst. Solids 2009. **355**(14-15): p. 874-879
154. A. G. Evans, E.A.C., *Fracture toughness determinations by indentation.* J. Am. Ceram. Soc., 1976. **59**: p. 371-372.
155. G. R. Anstis, P.C., B. R. Lawn, D. B. Marshall, *A critical evaluation of indentation techniques for measuring fracture toughness: 1, direct crack*

measurements. J Am Ceram Soc., 1981. **64**: p. 533-538.
156. J. A. Nychka, D.L., B. Alexander, *In vitro bioactivity of 45S5 bioactive glass as function of indentation load.* J. Mech. Behav. Biomed. Mater., 2008. **1**: p. 243-251.
157. T. Kokubo, H.K., S Kitsugi, T. Yammamuro, *Solutions able to reproduce in vivo surface-structure changes in bioactive glass-ceramic A-W.* J. Biomed. Mater. Res., 1990. **24**: p. 721-734.
158. S.-W. Ha, K.-L.E., E. Wintermantel, H. Gruner, M. Guecheva, H. Vonmont, *NaOH treatment of vacuum-plasma-sprayed titanium on carbon fibre-reinforced poly(etheretherketone).* J. Mater. Sci.: Mater. Med., 1997. **8**: p. 881-886.
159. C. Q. Ning, Y.Z., *In vitro bioactivity of a biocomposite fabricated from HA and Ti powders by powder metallurgy method.* Biomaterials, 2002. **23**: p. 2909-2915.
160. Y. W. Gu, K.A.K., P. Cheang, *In vitro studies of plasma-sprayed hydroxyapatite/Ti-6Al-4V composite coatings in simulated body fluid (SBF)* Biomaterials, 2003. **24**: p. 1603-1611.
161. M. Vallet-Regi, A.J.S., J. Roman, M. Gill, *Effect of magnesium content on the in vitro bioactivity of CaO–MgO–SiO2–P2O5 sol–gel glasses.* J. Mater. Chem., 1999. **9**: p. 515-518.
162. I. B. Leonor, A.I., K. Onuma, N. Kanzaki, R. L. Reis, *In vitro bioactivity of starch thermoplastic/hydroxyapatite composite biomaterials: an in situ study using atomic force microscopy.* Biomaterials, 2003. **24**: p. 579-585.
163. M. Wang, J.W., *Developing tricalcium composite as a new biodegradable material for clinical applications.* J. Biomechanics, 2000. **192**: p. 741-744.
164. Hench, L.L., *Biomaterials: a forecast for the future.* Biomaterials, 1998. **19**: p. 1419-1423.
165. K. H. Prakash, R.K., S. C. Yu, K. A. Khor, P. Cheang, *On the Kinetics of Apatite Growth on Substrates under Physiological Conditions.* Langmuir 2006. **22**: p. 269-276.
166. J. L. Katz, K.U., *On the anisotropic elastic properties of hydroxyapatite.* J. Biomechanics, 1971. **4**: p. 221-227.
167. V.V. Silva, F.S.L., R. Z. Domingues, *Microstructural and mechanical properties of ceramics for bio-medical applications.* Composites Sci. Tech., 2001. **61**: p. 301-310.
168. W. E. Brown, N.E., B. Tomazic, *Octacalcium Phosphate as a Precursor in Biomineral Formation.* Adv. Dent. Res., 1987. **1**: p. 306-313.
169. R. Z. LeGeros, P.C., *Apatites in biological systems.* Growth Charact. Mater., 1981. **4**: p. 1-45.
170. H.-M. Kim, K.K., F. Miyaji, T. Kokubo, T. Yao, Y. Suetsugu, J. Tanaka, T. Nakamura, *Composition and structure of the apatite formed on PET substrates in SBF modified with various ionic activity products.* J. Biomed. Mater. Res., 1999. **46**: p. 228-235.
171. X. Lu, Y.L., *Theoretical analysis of calcium phosphate precipitation in*

simulated body fluid. Biomaterials, 2005. **26**: p. 1097-108.
172. Sargent, P.M. *Microindentation Techniques in Mater- ials Science and Engineering*. in *American Society for Testing and Materials*. 1986. Philadelphia, PA.
173. A. R. Franco, G.P., A. Sinatora, C. E. Pinedo, A. P. Tschiptschin, *The Use of a Vickers Indenter in Depth. Sensing Indentation for Measuring Elastic Modulus and Vickers. Hardness.* J. Mater. Res., 2004. **7**: p. 483–491.
174. Fischer-Cripps, A.C., *Nanoindentation.* Springer-Verlag, 2002: p. 136.
175. K. Geng, F.Q.Y., E. A. Grulke, *Nanoindentation of submicron polymeric coating systems* Mater. Sci. Eng. A., 2008. **479**: p. 157-163.
176. F. A. Müller, L.M., D. Caillard, E. Conforto, *Preferred growth orientation of biomimetic apatite crystals.* J. Cryst. Growth, 2007. **304**: p. 464-471.
177. Green, D.J., *Compressive Surface Strengthening of Brittle Materials.* Journal of Materials Science, 1984. **19**(7): p. 2165-2171.

Vita

Ding Li was born on June 16th, 1981 in Ganzhou, Jiangxi, China.

EDUCATION:

M.S. in Materials Science and Engineering, Beijing Institute of Technology (2002-2005);
B.S. in Materials Science and Engineering, Hefei University of Technology (1998-2002)

RECENT AWARD:

Research Challenge Trust Fund Fellowship from UK (2006-2007)
NSF Travel Award for NSF CMMI 2008 Research and Innovation Conference
NSF Travel Award for 2008 TMS
NSF/ARO Travel Award for 2009 TMS

PUBLICATIONS:

1. Ding Li and Fuqian Yang, John A. Nychka, "Growth and Mechanical Behavior of Hydroxyl-Carbonate Apatite Layer on 45S5 Bioactive Glass", J. Mechanical Behavior of Biomedical Materials, submitted.

2. Ding Li, Fuqian Yang and Peter K. Liaw, "Stress-Assisted Electrochemical Corrosion of Cu-Based Bulk Metallic Glass", Journal of Materials Research, 25(3), 592-597, 2010.

3. Ding Li and Fuqian Yang, "Anelastic Indentation Recovery of Bioglass 45S5 at Room Temperature", Journal of non-crystalline solids, 356(3), 169-171, 2010.

4. Fuqian Yang and Ding Li, "Indentation-induced formation of low-dimensional Si structures in KOH solution", J. Phys. D: Appl. Phys. 43(9), 5403, 2010.

5. Ding Li, Yang Mimi X. Muralidhar Pavitra ; Wu Connie ; Fuqian Yang "Local surface damage and material dissolution in 45S5 bioactive glass: Effect of the contact deformation", Journal of non-crystalline solids, 355, 874-879, 2009.

6. Fuqian Yang, Ding Li, Mimi X Yang, Ran Li, Wenhui Jiang, Gongyao Wang, Tao Zhang and Peter K Liaw, "Localized deformation of a Cu46.25Zr45.25Al7.5Er1 bulk metallic glass", J. Phys. D: Appl. Phys. **42** 065401 (8pp), 2009.

7. John A. Nychka, Sherri L. R. Mazur, Satadru Kashyap, Ding Li and Fuqian Yang, “Dissolution of bioactive glasses: The effects of crystallinity coupled with stress”, JOM 61(9), 2009.

8. Ding Li, Fuqian Yang and John Nychka, “Indentation-induced residual stresses in 45S5 bioglass and the stress effect on the material dissolution” Engineering Fracture Mechanics 75, 4898 – 4908, 2008.

9. J.A. Nychka and D. Li, Surface Morphological Changes Accompanying Dissolution of Bioactive Glass: Effect of Residual Stress, Advanced Materials Research, 47–50, 1302-1306, 2008.

10. J.A. Nychka, D. Li, and B. Alexander, In vitro bioactivity of 45S5 bioactive glass as a function of indentation load, J. Mechanical Behavior of Biomedical Materials, 1, 243-251, 2008.

Ding Li

04/01/2010